DISSERTATION

NONLINEAR ELECTRIC POLARIZATION IN WURTZITE GROUP III-NITRIDES

Submitted by

Georgiy O. Vaschenko

Department of Electrical and Computer Engineering

In partial fulfillment of the requirements

for the Degree of Doctor of Philosophy

Colorado State University

Fort Collins, Colorado

Fall 2002

ProQuest Information and Learning Company
300 North Zeeb Road
P.O. Box 1346
Ann Arbor, MI 48106-1346

COLORADO STATE UNIVERSITY

NOVEMBER 1, 2002

WE HEREBY RECOMMEND THAT THE DISSERTATION PREPARED UNDER OUR SUPERVISION BY GEORGIY O. VASCHENKO ENTITLED NONLINEAR ELECTRIC POLARIZATION IN WURTZITE GROUP III-NITRIDES BE ACCEPTED AS FULFILLING IN PART REQUIREMENTS FOR THE DEGREE OF DOCTOR OF PHILOSOPHY.

Committee on Graduate Work

Adviser

Department Head

Abstract of Dissertation

Nonlinear Electric Polarization in Wurtzite Group III-nitrides

In this dissertation we provide the first experimental investigation of the nonlinear piezoelectric effect in technologically important group III-nitride heterostructures with wurtzite crystal lattice configuration. This effect is revealed by modifying the strain state in the InGaN/GaN and GaN/AlGaN quantum well structures by applied hydrostatic pressure. The ensuing changes in the electric polarization are probed with time-integrated and time-resolved photoluminescence spectroscopy. From the photo-luminescence peak energy of the quantum well emission at different applied pressures we obtain the values of the polarization-induced built-in electric field in the wells and the corresponding well-barrier polarization difference. We found that in the InGaN/GaN and GaN/AlGaN quantum well structures the built-in field increases with applied pressure much faster than expected from the conventional (linear) model of macroscopic polarization in group III-nitrides. In the InGaN/GaN structures the built-in field increases from ~ 1.4 MV/cm at atmospheric pressure to ~ 2.6 MV/cm at 9 GPa, while the theory predicts a reduction of the field to ~ 1.3 MV/cm. This discrepancy is interpreted as the signature of the strong nonlinearity of the piezoelectric response in the group III-nitrides. Model calculations incorporating the strain dependence of the piezoelectric coefficients of the investigated materials reproduce reasonably well the experimentally observed pressure behavior of the built-in electric field. Other secondary effects, such as nonlinear elasticity and photoelastic effect, have also been included in this model and are shown to have a significantly smaller effect on the observed changes in the photoluminescence with pressure. We conclude that the nonlinear piezoelectric effect plays the dominant role in defining the pressure behavior of photoluminescence in the InGaN/GaN and GaN/AlGaN quantum well structures.

The findings of this work reveal the large scale of the nonlinear piezoelectric effect in group III-nitrides and challenge the accuracy of the conventional theory of macroscopic polarization in these materials. We show that for the accurate modeling of the nitride-based devices the nonlinear piezoelectricity should be accounted for. Also, this work for the first time unequivocally identifies the polarization-induced electric field as the mechanism responsible for the anomalous pressure behavior in the InGaN/GaN and GaN/AlGaN quantum well structures.

Georgiy O. Vaschenko
Department of Electrical and Computer Engineering
Colorado State University
Fort Collins, CO 80523
Fall 2002

Acknowledgments

This dissertation is the result of collective effort of a large group of people. Among these people my adviser, Dr. Carmen Menoni, made the most important contribution. I would like to thank her for the continuous support, trust, and involvement over the years of my dissertation work. I have learned a great deal from her.

I would like to acknowledge my co-adviser, Dr. Jorge Rocca, for his interest in this work and encouragement of publishing its results. I would also like to thank my graduate committee members, Dr. Gary Robinson and Dr. Nancy Levinger, for sharing their insight on the early stages of this work and for reading the manuscript of this dissertation.

Among the people in our lab I should recognize the contribution made by Dr. Dinesh Patel who taught me how to do pressure dependent studies, prepared the samples for the measurements, and suggested many important ideas that were implemented in this dissertation work. The help and useful discussions on the subject of this work with Ovidio Anton and Dr. Jon Pikal are also greatly appreciated.

This dissertation would not be possible without the help of our collaborators. Dr. Milan Minsky and Dr. Stacia Keller from the University of California at Santa Barbara made very significant contributions to this work on its early stages by providing samples for our study and by engaging into very helpful discussions on the properties of nitride heterostructures. Dr. Milan Minsky also deserves a credit for providing results of

her investigation of the InGaN/GaN quantum wells. I am indebted to Dr. Nathan Gardner from Lumileds Lighting and to Dr. Hock Min Ng from Bell Labs for providing nitride quantum well samples and for sharing their insight into the processes in these structures. Dr. Carlos Tomé from Los Alamos National Lab deserves recognition for his help on the calculation of strain in quantum well structures under pressure and for the numerous discussions of the elasticity considerations in our experiments.

Finally, I would like to thank the very special people in my life, my wife Tanya and son Alexander, who were always a source of inspiration and moral support for me.

Table of Contents

Chapter **Page**

List of Tables x

List of Figures xi

1. Introduction 1

2. Background 6

2.1. Physical properties of GaN, AlN, InN and their alloys and heterostructures 6

2.1.1. Structural properties 6

2.1.2. Energy bands and effective masses 9

2.1.3. Mechanical properties 12

2.1.4. Substrates for epitaxial growth of group III-nitrides 14

2.1.5. Group III-nitride alloys and heterostructures 17

2.2. Spontaneous and piezoelectric polarization in group III-nitrides 19

2.3. Polarization-induced electric fields in III-nitrides 21

2.4. Nonlinear electromechanical properties in group III-nitrides 27

2.4.1. Nonlinear elasticity 29

2.4.2. Electroelastic effect 31

2.4.3. Nonlinear piezoelectricity 32

2.4.4. Electrostriction 34

2.4.5. Photoelastic effect 35

2.4.6. Electrooptical effect 35

2.5. Important experimental studies in nitride quantum wells 36

2.5.1. Carrier localization effect 36

2.5.2. Polarization induced electric field 42

2.5.3. Pressure studies 46

3. Experiment 50

3.1. Samples description 50

3.2. Details of experimental techniques 53

4. Experimental results 57

4.1. Pressure measurements in InGaN/GaN quantum wells and InGaN epilayer ... 57

4.2. Pressure measurements in GaN/AlGaN quantum wells 61

5. Interpretation and analysis of experimental results 66

5.1. Pressure dependent PL in InGaN/GaN quantum wells and InGaN epilayer 67

5.1.1. Calculation of strain varied by pressure 69

5.1.2. Bandgap energy variation with pressure 71

5.1.3. Determination of the built-in field and polarization 72

5.1.4. Pressure dependence of PL decay time 76

5.2. Pressure dependent PL in GaN/AlGaN quantum wells 79

5.2.1. Calculation of the exciton binding energy 81

5.2.2. Built-in electric field and well-barrier polarization difference 82

5.2.3. The role of the other secondary effects 89

6. Impact of this work on recent studies in group III-nitrides 90

7. Conclusion 96

Appendix 1. Definition of electric polarization 99

Appendix 2. Calculation of the electron and hole confinement energies in the presence of transverse electric field 102

Appendix 3. Calculation of quantum well exciton binding energy 104

Bibliography 105

List of Tables

Table **Page**

2.1. Physical parameters of wurtzite GaN, AlN, and InN 7

2.2. Properties of some materials suitable as substrates for the growth of group III-nitrides 16

2.3. Spontaneous polarization and piezoelectric coefficients of group III-nitrides ... 19

2.4. Calculated elastic stiffness coefficients of AlN and their pressure derivatives ... 31

3.1. Summary of the parameters of investigated samples 53

5.1. Calculated pressure coefficients of the bandgap energy in GaN and AlGaN with different AlN mole fraction 81

List of Figures

Figure **Page**

1.1. Number of publications in the mainstream scientific literature containing 'GaN' in the topic area 2

2.1. Atomic arrangement in wurtzite GaN lattice 6

2.2. Ga-face (a), and N-face (b) lattice orientation in GaN film 9

2.3. Bandgap energies of nitrides as a function of the in-plane lattice constant 10

2.4. Binding energies of excitons confined in GaN/AlGaN quantum wells as a function of well width calculated for different electric fields 12

2.5. In-plane atomic arrangement of the (0001) AlN film grown on (0001) sapphire 15

2.6. Cross-section TEM micrograph of an ELOG GaN film on sapphire substrate ... 17

2.7. Spontaneous polarization in AlInGaN alloys as a function of lattice constant ... 23

2.8. Built-in electric field in the wells of a hypothetical InGaN/GaN structure with 3 nm wells and 5 nm barriers as a function of InN mole fraction 25

2.9. Effect of the built-in electric field in the wells of an InGaN/GaN structure 26

2.10. Conduction band edge profile in a 10 nm wide $In_{0.20}Ga_{0.80}N$/GaN quantum well calculated for several values of free carrier concentrations 27

2.11. Pressure dependence of the unit cell volume in the GaN 30

2.12. Calculated piezoelectric constants of GaN as a function of applied volume conserving strain 33

2.13. Cross section TEM image of a commercial InGaN/GaN LED structure with high emission efficiency 37

2.14. Electroluminescence (EL), photovoltage (PV), and modulated electroabsorption (EA) spectra of three InGaN/GaN LEDs with varying InN mole fraction in the wells x 38

2.15. Carrier localization on In-rich clusters in nonuniform InGaN alloy 39

2.16. TEM image of the $In_{0.20}Ga_{0.80}N/In_{0.05}Ga_{0.95}N$ quantum well region of a purple laser structure 40

2.17. Calculated squared wave function of the valence (a) and conduction (b) band states of $In_{0.20}Ga_{0.80}N$ alloy 41

2.18. Low temperature (T = 8 K) time-integrated PL spectrum of the GaN quantum well (QW) and $Al_{0.93}Ga_{0.07}N$ (B) emission 42

2.19. Calculated and experimental forward current in GaN/AlN/GaN structure with 3 nm AlN layer 43

2.20. Calculated and experimental PL peak energies of the $In_{0.13}Ga_{0.87}N/In_{0.03}Ga_{0.97}N$ quantum wells 44

2.21. PL peak energies and decay times in the $GaN/Al_{0.24}Ga_{0.76}N$ quantum wells 45

3.1. Structure of the InGaN/GaN quantum well samples A1 - A3 50

3.2. Schematic diagram of the InGaN epilayer B1 51

3.3. Schematic diagram of the GaN/AlGaN quantum well structures C1 - C3 52

3.4. Cross-sectional TEM image of the sample C3 52

3.5. Schematic diagram of the time-resolved photoluminescence set-up 54

3.6. Schematic cross-section of a diamond anvil cell and the actual size picture of the cell used in this work 56

4.1. Photoluminescence obtained from an $In_{0.15}Ga_{0.85}N/GaN$ quantum well structure with 3.1 nm wells at different applied pressures 57

4.2. Pressure dependence of the PL peaks in $In_{0.15}Ga_{0.85}N/GaN$ quantum wells and GaN layers obtained with optical excitation intensity of 2 W/cm^2 and 200 W/cm^2 58

4.3. Pressure dependence of the quantum well PL decay times in $In_{0.15}Ga_{0.85}N$/GaN structures obtained with optical excitation intensity of 2 W/cm^2 60

4.4. Low temperature PL obtained from 80 nm $In_{0.11}Ga_{0.89}N$ epilayer at atmospheric pressure and at 11 GPa 60

4.5. Pressure dependence of PL peak energy in the 80 nm $In_{0.11}Ga_{0.89}N$ epilayer 61

4.6. Low temperature (T = 35 K) PL spectrum obtained from GaN/$Al_{0.50}Ga_{0.50}N$ quantum well structure at atmospheric pressure 62

4.7. Pressure dependence of the PL peaks in GaN/$Al_xGa_{1-x}N$ quantum well structures with $x = 0.2$ (a), $x = 0.5$ (b), and $x = 0.8$ (c) 63

4.8. Pressure dependence of the quantum well PL decay times in GaN/$Al_{0.5}Ga_{0.5}N$ structure obtained with optical excitation intensity of 2 W/cm^2 64

5.1. Pressure dependence of the strain components in $In_{0.15}Ga_{0.85}N$/GaN quantum wells 71

5.2. PL peak energy in InGaN/GaN quantum wells as a function of well width at different applied pressure 73

5.3. Experimental and theoretical pressure dependence of the built-in electric field in $In_{0.15}Ga_{0.85}N$/GaN quantum wells 74

5.4. Pressure dependence of the PL decay time constant in 2.5 and 3.1 nm quantum wells 77

5.5. Ground state electron and hole wavefunctions squared calculated for atmospheric pressure and for 9 GPa in a 3.1 nm InGaN/GaN quantum well 78

5.6. Calculated pressure dependence of the strain components in GaN quantum wells of GaN/AlGaN structures 80

5.7. Exciton binding energy as a function of the well width calculated using the theoretical values of the built-in electric field at atmospheric pressure 82

5.8. Schematic diagram of the conduction band edge in the GaN/AlGaN quantum well region 83

5.9. Well width dependence of the PL peak energy in GaN/AlGaN quantum wells at 5 GPa 86

5.10. Pressure dependence of P_w–P_b and corresponding built-in electric field in 2.9 nm GaN/AlGaN quantum wells 87

5.11. Experimental and 'linear' model pressure dependence of P_w–P_b in the GaN/AlGaN quantum wells with $x = 0.5$ obtained considering pressure dependence of the elasticity coefficients C_{ij} of sapphire, AlN, and GaN, and that of the dielectric constants of AlN and GaN 89

6.1. Experimental and calculated pressure coefficients in GaN/$Al_{0.17}Ga_{0.83}N$ quantum wells 92

6.2. Experimental and calculated pressure coefficients in GaN/$Al_{0.17}Ga_{0.83}N$ quantum wells 92

6.3. Experimental pressure coefficients of PL peak energies in wurtzite and zincblende InGaN/GaN quantum wells 93

6.4. Nonlinear spontaneous a) and piezoelectric b) polarization in the group III-nitride alloys as a function of the alloy composition x 94

6.5. Calculated spontaneous polarization versus lattice constant of ideal wurtzite structure 95

6.6. Experimental and calculated pressure dependence of P_w–P_b and corresponding built-in electric field in 2.9 nm GaN/AlGaN quantum wells 96

6.7. Calculated and experimental values of the built-in electric field in the GaN/AlGaN quantum wells as a function of alloy composition in the barriers 97

1. Introduction

Gallium nitride (GaN), aluminium nitride (AlN), and indium nitride (InN) offer a unique blend of physical properties that are attractive for fundamental investigations as well as for numerous applications in industry. Large bandgap and large band offsets make these materials good candidates for the design of ultraviolet, visible and infrared lasers, short wavelength light emitting diodes (LED), and solar blind photodetectors. Good thermal conductivity, large breakdown fields, excellent chemical stability, unusually high saturated electron drift velocity, and large polarization induced electrical fields uniquely define group III-nitrides as materials of choice for high power, high frequency active electronic devices. From the fundamental research prospective III-nitrides are interesting since unlike many other, better explored semiconductors crystallizing with zinc blende lattice (i.e. GaAs, InP, etc.), these materials normally have wurtzite lattice configuration. Among the most remarkable consequences of this type of the crystal symmetry is a significant electrical polarization which manifest itself in a variety of ways and which is the main focus of this dissertation.

Group III-nitrides were first synthesized as early as in 1928-38 [1-3]. However, the experimental study of these materials was hampered for years by the low structural quality of the samples. Only in the early 1990s the progress in the epitaxial techniques of crystal growth resulted in elevating the quality of nitride films to the level sufficient for application in practical devices. The turning point in exploration of nitrides was the demonstration in 1991 by Akasaki *et al.* [4] and by Nakamura *et al.* [5] of efficient GaN-based blue light emitting diodes (LEDs). Driven by the success in realization of these devices the nitride's field exploded in the following years (Fig. 1.1). Availability of reasonably good single crystal films and heterostructures prompted an extensive experimental and theoretical investigation of the GaN and its alloys with AlN and InN. It was then realized that the properties of these materials are significantly different than the properties of much better explored GaAs and other III-V semiconductors.

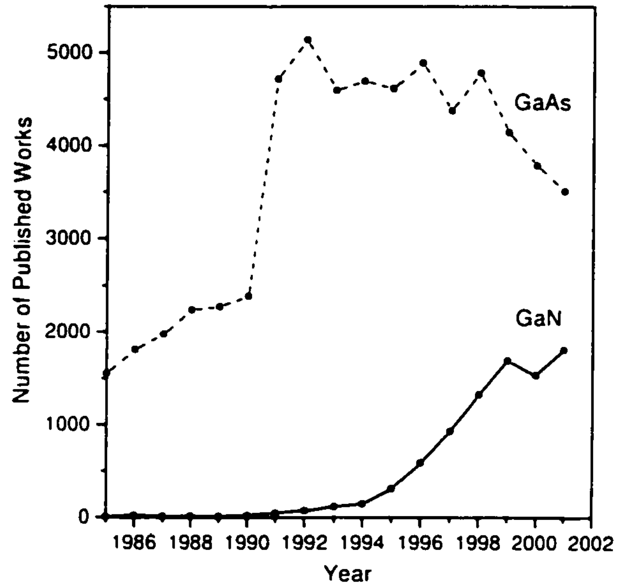

Fig. 1.1. Number of publications in the mainstream scientific literature containing 'GaN' in the topic area. The number of works on GaAs is shown for comparison by the dashed line. Source: ISI Web of Science database.

Examples of such differences are the unusually low sensitivity of the performance of the GaN based LEDs on the density of dislocations in the material, extremely long emission decay times in the quantum well structures, lower than expected photon energy of emission from the quantum wells, low pressure coefficients of photoluminescence, etc.

Some of the peculiar effects observed in nitrides have already found their explanation. However, due to the novelty of these materials and due to the structural imperfections of the epitaxial crystals typical for the currently employed growth techniques, the detailed and accurate understanding of the physics of the group III-nitrides is yet to come.

Probably the least understood and explored area in the emerging physics of group III-nitrides is the electrostatics of these materials and in particular the effects of electric polarization. In part this can be explained by the latency of the quantum mechanical theory of electric polarization in crystals, which was developed less than ten years ago [6 - 9]. In part it can be also attributed to the fact that most of the developments in this theory and ensuing practical studies were made within the dielectrics and ferroelectrics communities, while the first effort to adopt these developments to the semiconductors is dated by 1997 [10].

Understanding the role that macroscopic polarization plays in the group III-nitrides has not only theoretical, but also very important practical implications. Intense polarization fields in GaN-based heterostructures are held responsible for the high threshold current and emission red shift in the short wavelength lasers [11]. In emerging long wavelength intersubband transition structures the polarization-induced electric fields increase the intersubband relaxation time and reduce the effective barrier height [12]. Polarization-induced two-dimensional electron gases in GaN-based high electron mobility transistors allow one to achieve sheet carrier concentrations of up to $2 \cdot 10^{13}$ cm^{-2} resulting in outstanding performance of these devices [13]. To design these and other group III-nitride devices and to optimize their characteristics a clear picture of polarization effects is required.

Conventional theory of polarization in solids traditionally assumes that the polarization response of material to the strain (that can be for instance generated by the lattice mismatch in the epitaxially grown heterostructure) is essentially a linear effect that can be described by the piezoelectric tensor e_{ijk} simply as:

$$\Delta P_i = e_{ijk}\varepsilon_{jk}, \tag{1.1}$$

where ΔP_i is a change of spontaneous polarization in the i direction due to strain (also known as piezoelectric polarization), ε_{jk} is the strain tensor, and elements of e_{ijk} are constants independent of strain [14-17]. This model was shown to accurately describe properties of many semiconductor structures [17-21]. However, in early 1990's R. André *et al.* [22, 23] demonstrated experimentally a nonlinear behavior of the piezoelectric response in CdTe-based quantum wells. A strong polarization nonlinearity in this II-VI material was explained by the sensitivity of the piezoelectric constant to the change in the crystal volume [24]. In 1998 K. Shimada *et al.* [25] predicted in a theoretical work that similar effects can be expected in group III-nitrides. It was suggested that the piezoelectric constants of the GaN and AlN have strong dependences on the volume conserving strain. However, there was no experimental evidence to confirm or to dispute these predictions.

In this dissertation we provide a systematic investigation of the polarization-induced electric field in the InGaN/GaN and in GaN/AlGaN quantum well structures. To obtain signatures of this field in structures with different geometry we use photoluminescence (PL) at different temperatures and excitation intensities, time resolved PL, and pressure dependent PL measurements. Our experimental findings strongly support an important role that the polarization-induced field plays in the optical properties of the nitride heterostructures. By applying hydrostatic pressure to the quantum well samples we modify the strain state in the wells and in the barriers, and therefore we tune the polarization-induced electric field. This method allows us to increase the field by 25 – 100 %, depending on the sample and applied pressure. Such significant increase of the polarization-induced electric field proves the conventional model of polarization to be insufficient to describe the observed effects and suggests strong nonlinearity in the polarization response to the applied strain. This is the first evidence of the strong polarization nonlinearity in the group III-nitride heterostructures.

This dissertation is divided into seven chapters. Chapter 1 is the introduction. The second chapter describes the most important physical properties of the nitrides, including some of the known nonlinear properties of these materials. Chapter 3 describes the InGaN/GaN and GaN/AlGaN samples investigated in this work and the experimental techniques implemented in our study. Chapter 4 summarizes the major results of the time-integrated and time-resolved pressure dependent photoluminescence study implemented in our work. Chapter 5 provides the analysis and interpretation of the experimental data, where the main focus is on revealing the strong nonlinearities in the strain response of the polarization-induced electric field. Chapter 6 considers the impact of our work on the recent studies in group III-nitrides. And finally, Chapter 7 summarizes the whole dissertation and suggests some of the possible areas of future investigations of nonlinear properties of the group III-nitrides.

2. Background

2.1. Physical properties of GaN, AlN, InN and their alloys and heterostructures

2.1.1. Structural properties

Group III-nitrides are semiconducting materials with wurtzite (hexagonal or α) crystal lattice configuration at equilibrium. The atomic arrangement in wurtzite GaN lattice is shown in Fig. 2.1. This kind of crystal lattice is described by three independent parameters: length of the basal hexagon *a*, the height of the hexagonal prism *c*, and the anion-cation bond length (in units of *c*) along the (0001) axis *u*, known as internal

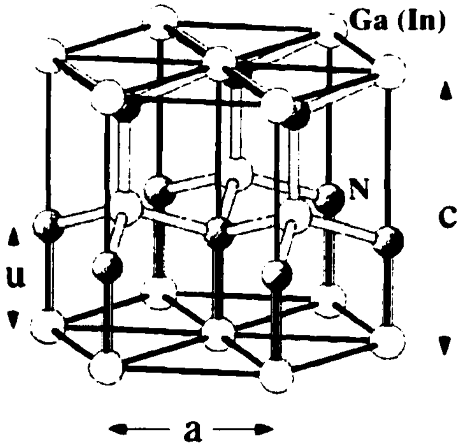

Fig. 2.1. Atomic arrangement in wurtzite GaN lattice. After Stampfl and Van de Walle [26].

parameter. The conventional values of these parameters for group III-nitrides are given in Table 2.1. This table also provides the summary of the other fundamental parameters of nitrides in wurtzite phase.

Table 2.1. Physical parameters of wurtzite GaN, AlN, and InN.

Parameters	GaN	AlN	InN	References
a, (Å)	3.1890	3.110	3.538	[27]
c, (Å)	5.1864	4.980	5.703	[27]
u	0.377	0.3821	0.3749	[28, 29]
E_g, (eV)	3.507	6.23	1.994	[30]
$m_e^{\parallel} / m_o$	0.20	0.33	0.11	[31, 32]
$m_e^{\perp} / m_o$	0.18	0.25	0.10	[31, 32]
$m_{hh}^{\parallel} / m_o$	1.76	3.53	1.56	[31, 32]
$m_{hh}^{\perp} / m_o$	1.61	10.42	1.68	[31, 32]
$m_{lh}^{\parallel} / m_o$	1.76	3.53	1.56	[31, 32]
$m_{lh}^{\perp} / m_o$	0.14	0.24	0.11	[31, 32]
E_{ex}, (meV)	23	44	-	[30, 33]
$a_c^{\perp} - D_1$, (eV)	-6.11	-4.21	-4.05	[34]
$a_c^{\parallel} - D_2$, (eV)	-9.62	-12.04	-6.67	[34]
D_3, (eV)	5.76	9.06	4.92	[34]
D_4, (eV)	-3.04	-4.05	-1.79	[34]
C_{11}, (GPa)	390	345	223	[35, 36, 37]
C_{12}, (GPa)	145	125	115	[35, 36, 37]
C_{13}, (GPa)	106	120	92	[35, 36, 37]
C_{33}, (GPa)	398	395	224	[35, 36, 37]
C_{44}, (GPa)	105	118	48	[35, 36, 37]
C_{66}, (GPa)	123	110	54	[35, 36, 37]
B, (GPa)	210	201	141	[35, 36, 37]
ε_o	10.28	10.31	14.61	[10]

Under certain conditions, by using epitaxial growth techniques on zinc blende (cubic or β) substrates, III-nitrides with zinc blende configuration can also be realized. This phase is thermodynamically less stable than the wurtzite. Because of the lower stability zinc blende nitrides at present show structural quality inferior to their wurtzite counterparts. Since all of the structures investigated in this work had wurtzite configuration the description of the physical properties of nitrides here is mostly limited to those of the wurtzite symmetry.

One of the consequences of the wurtzite lattice configuration is the reduced symmetry. As appears from Fig. 2.1 the two directions along the c axis of the crystal are not equal: in one direction the bonds are faced by anions (N) and in the opposite direction by the cations (Ga). GaN crystals grown in the [0001] direction where the cation-anion bond points from Ga to N are distinguished as crystals with Ga-face polarity (Fig. 2.2(a)). On the other hand, if the crystal has the opposite orientation it has N-face polarity (Fig. 2.2(b)). The polarity is defined by the conditions of the initial stage of the crystal growth, such as the substrate type and orientation, type of the nucleation layer, growth temperature, *etc*. Generally, the metal organic chemically vapor deposited (MOCVD) GaN films on sapphire substrates have Ga-face polarity when they are grown on low temperature (~600 °C) buffer layers [38]. The molecular beam epitaxy (MBE) grown films have Ga-face polarity when deposited on a high temperature (900 °C) AlN buffers [38]. The polarity can be determined by wet chemical etching of the film surface (Ga-polar films have much smaller etch rates), and then examining the surface with atomic force microscopy (AFM) [39].

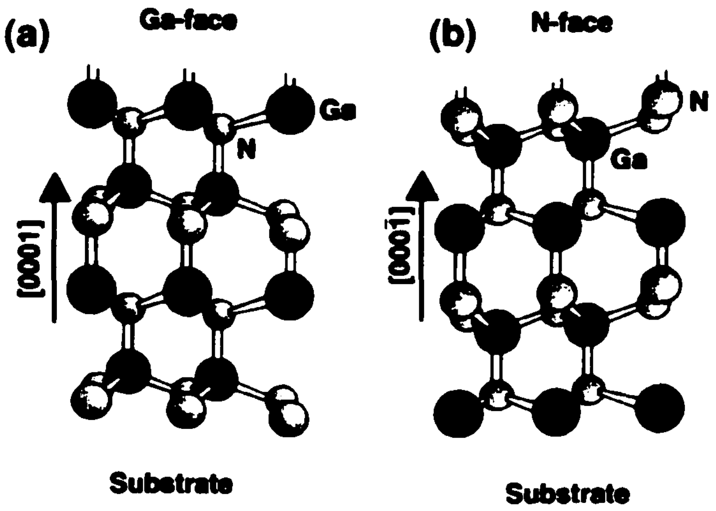

Fig. 2.2. Ga-face (Ga-polar) (a), and N-face (N-polar) (b) lattice orientation in GaN film. After Ambacher [40].

Polarity defines many important properties of the group III-nitrides [41]. The crystal growth mode itself depends on the polarity. Such characteristics as temperature stability of the crystal surface, stoichiometry, and dopant incorporation may be significantly affected by polarity. Closely related to polarity is also the orientation of the spontaneous and piezoelectric polarization and the resulting electric field along the growth axis in the III-nitride epilayers and heterostructures.

2.1.2. Energy bands and effective masses

One of the key parameters making III nitrides especially attractive for various applications is the bandgap energy E_g. These materials have direct bandgaps with energy ranging from 0.77-1.99 eV in InN, to 3.507 eV in GaN, and to 6.23 eV in AlN [30, 42] (Fig. 2.3). The large values of the bandgap energy and its large variation between different materials makes the group III-nitrides and their alloys potentially useful for application in optical devices operating from the red (~ 650 nm) to the deep ultraviolet (~200 nm) part of the spectrum.

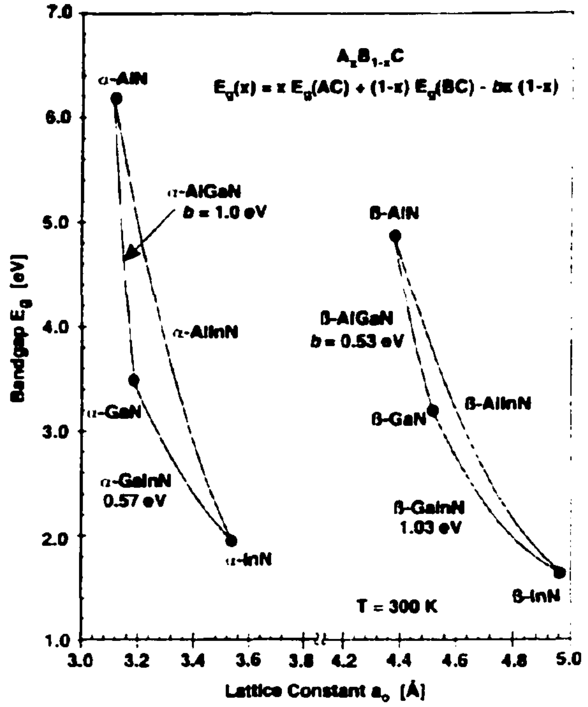

Fig. 2.3. Bandgap energies of nitrides as a function of the in-plane lattice constant. After Ambacher [40].

Although it is clear that the electron and hole effective masses in group III-nitrides are significantly larger than those in the conventional III-V materials, the exact values of the masses are still being established [30]. The bottom of the GaN and InN conduction bands can be well approximated by the parabolic dispersion relation with only a slight anisotropy. The values of the electron effective masses for the nitrides accepted in this work are shown in Table 2.1. In AlN the conduction band is more anisotropic and two different values should be used for the in-plane ($m_e^{\perp}$) and for the c-direction ($m_e^{\parallel}$) effective masses [31]. The top of the valence band in the nitrides is highly anisotropic and nonparabolic and therefore the values of the hole effective mass are even more uncertain than those of the electron. The heavy hole effective masses for GaN and AlN adopted in this work are taken from the theoretical paper of Suzuki *et al.* [31], while those for the InN are taken from the paper by Yeo *et al.* [32].

One of the consequences of the large effective masses in the group III-nitrides is the large exciton binding energy E_{ex}. In GaN the binding energy is ~ 23 meV [30], compared to only 4.2 meV in GaAs [43]. Thus, with E_{ex} comparable to the room temperature thermal energy kT, the excitons can be relatively stable even at room temperature. This is supported by the common observation of narrow excitonic peaks in the photoluminescence spectrum from good quality GaN epilayers [44, 45]. Excitonic recombination is also held accountable for the fast decay of the photoluminescence in these structures. The role of excitons in the recombination process can be even more important in the quantum well structures, where the binding energy significantly increases due to the quantum confinement. This effect is balanced by the reduction of the binding energy due to the quantum confined Stark effect produced by the polarization-induced electric field [46, 47]. The Stark effect prevails in the wider wells, while the quantum confinement controls exciton binding energy in the narrower ones (Fig. 2.4). In the wells wider than ~ 2 - 3 nm the reduction of the binding energy can be so important that it may result in ionization of the excitons.

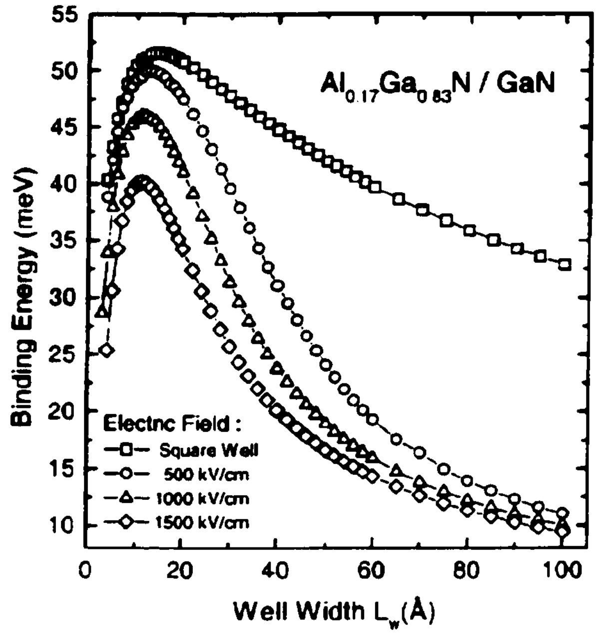

Fig. 2.4. Binding energies of excitons confined in GaN/AlGaN quantum wells as a function of well width calculated for different electric fields. After Grandjean *et al.* [47].

2.1.3. Mechanical properties

Mechanical properties of material describe its response to applied stress. The stress in nitride structures commonly results from the lattice mismatch between layers of different materials, lattice mismatch between the epitaxial layers and substrate, or it can be introduced externally by applying to the structure hydrostatic pressure. If moderate mechanical stress σ_i is applied to a nitride crystal it responds elastically by adjusting positions of the atoms in the lattice. This shift of the atoms from their equilibrium positions constitutes strain ε_j that, according to a Hook's law, can be related to applied stress via the elastic stiffness coefficients of material C_{ij}:

$$\sigma_i = C_{ij}\,\varepsilon_j. \tag{2.1}$$

For the wurtzite symmetry of the group III-nitrides this relation in the matrix form can be rewritten as [15]:

$$\begin{pmatrix}\sigma_1\\ \sigma_2\\ \sigma_3\\ \sigma_4\\ \sigma_5\\ \sigma_6\end{pmatrix}=\begin{pmatrix}C_{11} & C_{12} & C_{13} & 0 & 0 & 0\\ C_{12} & C_{11} & C_{13} & 0 & 0 & 0\\ C_{13} & C_{13} & C_{33} & 0 & 0 & 0\\ 0 & 0 & 0 & C_{44} & 0 & 0\\ 0 & 0 & 0 & 0 & C_{44} & 0\\ 0 & 0 & 0 & 0 & 0 & C_{66}\end{pmatrix}\times\begin{pmatrix}\varepsilon_1\\ \varepsilon_2\\ \varepsilon_3\\ \varepsilon_4\\ \varepsilon_5\\ \varepsilon_6\end{pmatrix}, \qquad (2.2)$$

where $C_{66}=\frac{1}{2}(C_{11}-C_{12})$. The elastic stiffness coefficients for three nitride materials are shown in Table 2.1. Experimental values are accepted for GaN and AlN, while due to the lack of good stoichiometry InN samples the theoretical values are cited for this material.

A characteristic that defines how material changes its volume V with applied hydrostatic pressure p is called compressibility. It is defined as [48]:

$$K=-\frac{1}{V}\left(\frac{dV}{dp}\right)_T=\frac{1}{B}, \qquad (2.3)$$

where B is called the bulk modulus of material. This later parameter is usually specified along with other mechanical characteristics of materials, even though it is not an independent parameter (it can be expressed via the elastic stiffness coefficients). GaN, AlN and InN have bulk moduli of 210 [35], 201 [36], and 141 [37] GPa respectively.

As was mentioned above the mechanical stress applied to the semiconductor crystal shifts the atoms from their equilibrium positions. This modifies the energy band structure. Deformation potentials describe the response of the conduction and the valence bands of a semiconductor to the strain generated by the applied stress (strain). For the wurtzite structure the change in the band edge positions can be expressed in terms of the strain as [34]:

$$\Delta E_c = a_c^{\parallel}(\varepsilon_1 + \varepsilon_2) + a_c^{\perp}\varepsilon_3, \tag{2.4}$$

and

$$\Delta E_v^{hh} = (D_2 + D_4)(\varepsilon_1 + \varepsilon_2) + (D_1 + D_3)\varepsilon_3, \tag{2.5}$$

where $a_c^{\parallel}$ and $a_c^{\perp}$ are the conduction band deformation potentials, $D_1 - D_4$ are the valence band deformation potentials, ε_1, ε_2 are the in-plane strain components, and ε_3 is the strain in the [0001] direction. In most experiments the change of the bandgap energy $\Delta E_g = \Delta E_c - \Delta E_v^{hh}$ is detected instead of the shift of the individual bands. Therefore instead of the individual deformation potentials the values of the $(a_c^{\perp} - D_1)$, $(a_c^{\parallel} - D_2)$, D_3, and D_4 are quoted, which can be used to relate ΔE_g to the strain according to:

$$\Delta E_g = (a_c^{\parallel} - D_2 - D_4)(\varepsilon_1 + \varepsilon_2) + (a_c^{\perp} - D_1 - D_3)\varepsilon_3. \tag{2.6}$$

In this work the values of the deformation potentials calculated by Chow and Koch [34] are accepted (Table 2.1).

2.1.4. Substrates for epitaxial growth of group III-nitrides

One of the major problems in fabricating good quality nitride films is the lack of suitable substrates with small lattice mismatch and good thermal compatibility with nitrides. The most common substrate for the nitrides is the α-sapphire (Al_2O_3 with trigonal lattice symmetry) [49]. This material is widely available, relatively inexpensive, has good thermal conductivity, and is optically transparent for the range of wavelengths emitted by the nitrides. GaN and AlN are usually grown on the (0001) plane of sapphire, with nitride atoms aligned by the oxygen atoms of sapphire forming a hexagonal lattice

(Fig. 2.5). The problems encountered with the growth on sapphire are the large lattice mismatch (Table 2.2), large difference in temperature expansion coefficients, and the insulating nature of the sapphire. The large lattice mismatch leads to generation of large

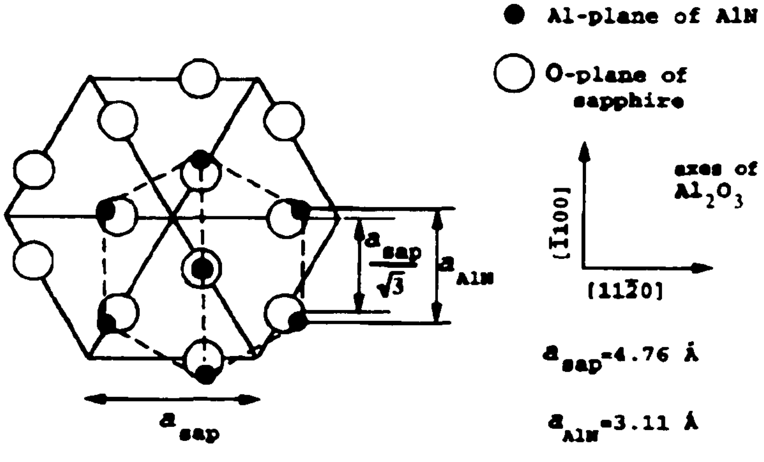

Fig. 2.5. In-plane atomic arrangement of the (0001) AlN film grown on (0001) sapphire. After Dovidenko *et al.* [50].

concentration of structural defects (i.e. dislocations) in the epitaxial films grown on sapphire. To mitigate this effect a low temperature grown GaN or AlN nucleation layer is usually deposited on the substrate prior to the deposition of the main structure [51]. This layer accommodates most of the lattice mismatch by a large density of structural defects and allows the growth of better quality following high temperature nitride layers. Another method used to improve the structural quality of the nitride films on sapphire substrates is to deposit thin SiO_2 stripes on the surface of the GaN buffer layer and then grow the film over these stripes. This technique is called epitaxial lateral overgrowth (ELOG) [52, 53]. Most of the residual in-plane strain is relieved in this configuration by the reduction of

Table 2.2. Properties of some materials suitable as substrates for the growth of group III-nitrides. After Ambacher [40].

Substrate	Lattice symmetry	Lattice constants, (Å)	Thermal expansion coefficient, (10^{-6} K^{-1})
α-GaN	Wurtzite	$a = 3.1890$ $c = 5.1864$	5.59 3.17
Al_2O_3	Rhombohedral	$a = 4.7589$ $c = 12.991$	7.3 8.5
6H-SiC	Wurtzite	$a = 3.0806$ $c = 15.1173$	4.46 4.16
Si	Diamond	$a = 5.43088$	3.59
GaAs	Zincblende	$a = 5.652$	6.0
MgO	Rock salt	$a = 4.216$	10.5
$MgAl_2O_4$	Diamond	$a = 8.083$	7.45
$LiGaO_2$	Orthorombic	$a = 5.4063$ $b = 6.3786$ $c = 5.0129$	6 9 7
ZnO	Wurtzite	$a = 3.252$ $c = 5.213$	2.9 4.75

lateral size of the GaN film. Also, the dislocations below the stripes are stopped from propagating towards the surface. The film coalesces over the SiO_2 stripes with a concentration of dislocations reduced from 10^8-10^{10} to 10^4-10^5 cm^{-2} (Fig. 2.6).

Another material that is used as a substrate for the growth of wurtzite nitrides is silicon carbide (SiC). This material has much smaller lattice mismatch than sapphire (~3.1 % for the GaN) and even better thermal conductivity than sapphire. However, SiC until now is not so commonly used due to the scarcity and high cost of this material.

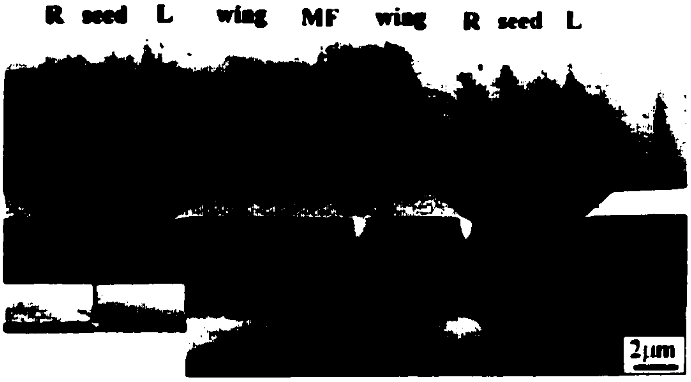

Fig. 2.6. Cross-section TEM micrograph of an ELOG GaN film on sapphire substrate. After Liliental-Weber and Cherns [53].

Another problem with SiC is that it usually forms various polytypes of stacking arrangements [51]. Therefore the layers grown on this material have nonuniform strain distribution along the surface of the wafer.

There are also reports of the growth of wurtzite and zinc blende nitrides on Si, GaAs, NaCl, GaP, InP, W, ZnO $MgAl_2O_4$, TiO_2, $NdGaO_3$, $LiGaO_2$, $LiAlO_2$, and MgO [40, 51]. A brief description of some of these materials is summarized in the Table 2.2. Ultimately, the best substrate for the growth of the nitrides would be bulk GaN, but up until now single crystal GaN substrates of sufficiently large size are not available.

2.1.5. Group III-nitride alloys and heterostructures

Nitrides are seldom used in devices as binaries. Most of applications require production of epitaxial layers of ternary and quaternary alloys, such as InGaN, AlGaN, or InAlGaN. Some of the properties of the nitride alloys can be described by simply taking a linear interpolation between the properties of the binary constituents. This applies with rather good precision to the *a* and *c* lattice constants, elastic stiffness coefficients, and, to some extent, the effective masses [30]. Thus the lattice constant of InGaN, for instance, can be found as:

$$a_{InGaN} = a_{GaN} + x(a_{InN} - a_{GaN}), \tag{2.7}$$

where x is the InN molar fraction in the InGaN. For other characteristics of nitrides linear interpolation does not always provide an accurate description. The most notable example of such deviation from the linear trend is the bandgap energy dependence on composition. For the ternary systems the bandgap values are always smaller than those predicted by linear interpolation (Fig. 2.2), and are usually described by the quadratic expression [30]:

$$E_g^{InGaN} = xE_g^{InN} + (1-x)E_g^{GaN} - bx(1-x), \tag{2.8}$$

where b is called bandgap bowing parameter. In this work values of $b = 2.6$ and 1 eV are accepted for InGaN and AlGaN respectively [54, 55].

Another parameter relevant in the analysis of nitride alloy based heterostructures is the conduction/valence band offset ratio. This parameter for nitrides is still being investigated both experimentally and theoretically. The experimental determination of the band offsets in the quantum well structures is hampered by the polarization-induced electric fields in the heterostructure layers that strongly affect positions of the confined energy states. Combining the results of the theoretical and experimental investigations the GaN/InN and AlN/GaN valence band offsets range from 0.48 to 1.05 eV and from 0.5 to 1.36 eV respectively [30]. In this dissertation band offsets calculated by Wei and Zunger [56] are adopted, suggesting the conduction/valence band offset ratio of 70/30 for InGaN/GaN and GaN/AlGaN systems.

2.2. Spontaneous and piezoelectric polarization in group III-nitrides

Spontaneous polarization P_{sp} (definition of this parameter is given in Appendix 2) in III-nitrides was first calculated in 1997 by Bernardini, Fiorentini and Vanderbilt [57], and later the calculations were refined by the same group of authors [58]. The results of the refined calculations are shown in the Table 2.3. The values of the spontaneous polarization obtained from the calculations strongly depend on the structural parameters of the nitrides, which are considered to have rather large uncertainty. Since the P_{sp} of any material cannot be measured experimentally the theoretical values cannot be directly verified. However, the experiments on nitride heterostructures confirm that the polarization differences between the materials are in the range expected from the theory.

Table 2.3. Spontaneous polarization and piezoelectric coefficients of group III-nitrides.

Material	P_{sp}, (C/m^2)	e_{33}, (C/m^2)	e_{31}, (C/m^2)	Reference
GaN	- 0.034	0.63 0.67 1.12	- 0.32 - 0.34	[25] [58] [59]
AlN	- 0.090	1.29 1.50 1.55	- 0.38 - 0.53 - 0.58	[25] [58] [59]
InN	- 0.042	0.81	- 0.41	[58]

As was discussed in the Introduction the strain in a crystal can modify spontaneous polarization. For the case of a crystal with wurtzite symmetry the strain-induced change of polarization in matrix form can be expressed as [15]:

$$\begin{pmatrix} \Delta P_1 \\ \Delta P_2 \\ \Delta P_3 \end{pmatrix} = \begin{pmatrix} 0 & 0 & 0 & 0 & e_{15} & 0 \\ 0 & 0 & 0 & e_{15} & 0 & 0 \\ e_{31} & e_{31} & e_{33} & 0 & 0 & 0 \end{pmatrix} \times \begin{pmatrix} \varepsilon_1 \\ \varepsilon_2 \\ \varepsilon_3 \\ \varepsilon_4 \\ \varepsilon_5 \\ \varepsilon_6 \end{pmatrix}. \qquad (2.9)$$

In most nitride systems the shear strains are nonexistent ($\varepsilon_4 = \varepsilon_5 = \varepsilon_6 = 0$), and therefore the only nonzero component of the piezoelectric polarization is the component along z-axis, which usually coincides with the crystal growth direction [0001]. In this dissertation we will consider only such case and the Eq. (2.9) will be reduced to:

$$\Delta P_3 = P_{pz} = e_{31}(\varepsilon_1 + \varepsilon_2) + e_{33}\varepsilon_3. \qquad (2.10)$$

The piezoelectric coefficients (also sometimes called piezoelectric constants) of wurtzite material can be expressed as [57]:

$$e_{31} = \frac{a_0}{2}\frac{\partial P_3}{\partial a} + \frac{2e}{\sqrt{3}a_0} Z^* \frac{du}{da}, \qquad (2.11)$$

and

$$e_{33} = c_0 \frac{\partial P_3}{\partial c} + \frac{4ec_0}{\sqrt{3}a_0^2} Z^* \frac{du}{dc}, \qquad (2.12)$$

where a_0 and c_0 are the equilibrium values of the lattice parameters, and

$$Z^* = \frac{\sqrt{3}a_0^2}{4e}\frac{\partial P_3}{\partial u} \qquad (2.13)$$

is the z-axis component of the Born (transverse) dynamical charge. The Born effective charge is a fundamental characteristic of the material that measures macroscopic polarization induced by a relative displacement of the cation and anion sublattices.

The first term in the Eqs. (2.11) and (2.12) is called the clamped-ion term and the second is the internal strain term. The clamped ion term describes the effect of the homogenous strain on the polarization in the absence of the internal strain u, while the internal strain term describes the contribution of the relative displacement of differently charged sublattices at fixed strain [57]. To calculate the piezoelectric coefficients the strain derivatives of the polarization can be found using Eq. (A1.2), where the transformation $\lambda_1 \rightarrow \lambda_2$ is associated with the applied strain. The results of recent calculations of the piezoelectric coefficients for AlN, GaN, and InN are summarized in Table 2.3.

Experimentally it is not easy, if not impossible, to access just one of the terms in the piezoelectric coefficients of wurtzite materials due to the coupling between the homogeneous macroscopic strain and microscopic internal strain, and due to the presence of the three independent piezoelectric coefficients. Usually only the e_{33} and e_{15} are directly measured using the converse piezoelectric effect, i.e. by assessing the displacement of a crystal in an applied electric field [59]. The experimental values of e_{33} for GaN and AlN are shown in Table 2.3.

2.3. Polarization induced electric fields in III-nitrides

The presence of polarization in a finite system implies also existence of the electric field. In the general case of a quantum well system with no externally applied electric field the built-in field in the generic j-th well (or barrier) with thickness L_j can be found as [60]:

$$F_j = \frac{\sum_k L_k P_k / \epsilon_k - P_j \sum_k L_k / \epsilon_k}{\epsilon_j \sum_k L_k / \epsilon_k} \qquad (2.14)$$

where L_k is the thickness of the k-th layer, P_k is the total (spontaneous and piezoelectric) polarization in the k-th layer, and ϵ_k is the dielectric constant in k-th layer. Equation (2.14) is obtained from elementary electrostatics with the following assumptions:

1) the quantum wells are far enough from any interface or surface of the sample;
2) the well-barrier interfaces are free of interface states;
3) the quantum well region is sufficiently thick, so that the maximum error for defining the field with Eq. (2.14) $E_g / \sum_k L_k$ is a small number compared to the field value.

For the set of quantum wells and barriers made of just two materials Eq. (2.14) can be reduced to:

$$F_w = \frac{P_b - P_w}{\epsilon_w + \epsilon_b L_w / L_b}, \qquad (2.15)$$

where F_w is the field in the well layer, and L_w and L_b are the cumulative thicknesses of the well and the barrier layers respectively. A similar expression can be obtained for the field in the barrier F_b.

As appears from Eq. (2.15) the major role in defining the magnitude of the built-in electric field is played by the polarization difference between the barrier and the well materials. The polarization difference has two distinct components: the difference in spontaneous polarization between two materials and the difference of piezoelectric polarization, which can be significant when at least one of the materials is strained.

Figure 2.7 shows the spontaneous polarization in the AlN, GaN, InN and their compounds as a function of lattice constant *a* [60]. The lattice constant of AlN is close to that of GaN, and therefore the lattice mismatch strain produces only a small difference in the piezoelectric polarization components of these two materials or their ternary compounds. In contrast, a spontaneous polarization difference of ~ 0.056 C/m results in large built-in fields in GaN/AlN heterostructures. In the GaN and InN combination the opposite effect is expected: the piezoelectric polarization plays major role in defining built-in electric fields, while the spontaneous polarization contribution is negligible.

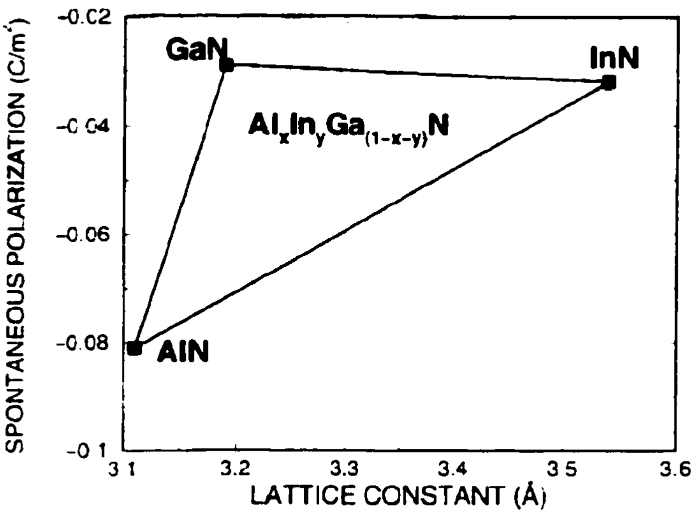

Fig. 2.7. Spontaneous polarization in AlInGaN alloys as a function of lattice constant. After F. Bernardini and V. Fiorentini [60].

To estimate the built-in field in a practical quantum well structure one has to find the lattice mismatch strain in the wells and in the barriers. In the InGaN/GaN quantum wells grown on GaN buffer, for example, the strain is defined by the InN mole fraction in the wells and it is given by:

$$\varepsilon_1^{InGaN} = \frac{a_{GaN} - a_{InGaN}}{a_{InGaN}}; \ \varepsilon_1^{GaN} = 0 \tag{2.16}$$

$$\varepsilon_3^{InGaN} = -2\frac{C_{13}^{InGaN}}{C_{33}^{InGaN}}\varepsilon_1^{InGaN}; \ \varepsilon_3^{GaN} = 0 \tag{2.17}$$

Since the quantum wells are much thinner than the GaN buffer layer the in-plane lattice constant of the InGaN matches that of the surrounding GaN layers, thus giving rise to the in-plane strain described by Eq. (2.16), and the GaN barriers remain strain-free. Equation (2.17) is obtained from Eq. (2.2) assuming vanishing stress along z-axis ($\sigma_3 = 0$). Once the strain is determined, the piezoelectric components of polarization can be calculated using Eq. (2.10). To find the piezoelectric coefficients and spontaneous polarization in InGaN Vegard's law is used, i.e.[11]:

$$e_{31}^{InGaN} = e_{31}^{GaN} + x(e_{31}^{InN} - e_{31}^{GaN}), \tag{2.18}$$

$$e_{33}^{InGaN} = e_{33}^{GaN} + x(e_{33}^{InN} - e_{33}^{GaN}), \tag{2.19}$$

and

$$P_{sp}^{InGaN} = P_{sp}^{GaN} + x(P_{sp}^{InN} - P_{sp}^{GaN}). \tag{2.20}$$

Then, using Eq. (2.15) the built-in field in the quantum wells can be obtained in a straightforward fashion.

Figure 2.8 shows the electric field in the wells of a hypothetical structure with 3 nm wells and 5 nm barriers as a function of InN mole fraction calculated using the approach just described. As follows from this plot even at small x = 0.1 – 0.2 typical for the InGaN-based light emitting devices the polarization induces a very large (~ 1 – 2 MV/cm) electric field across the wells. A field of such magnitude has a profound effect

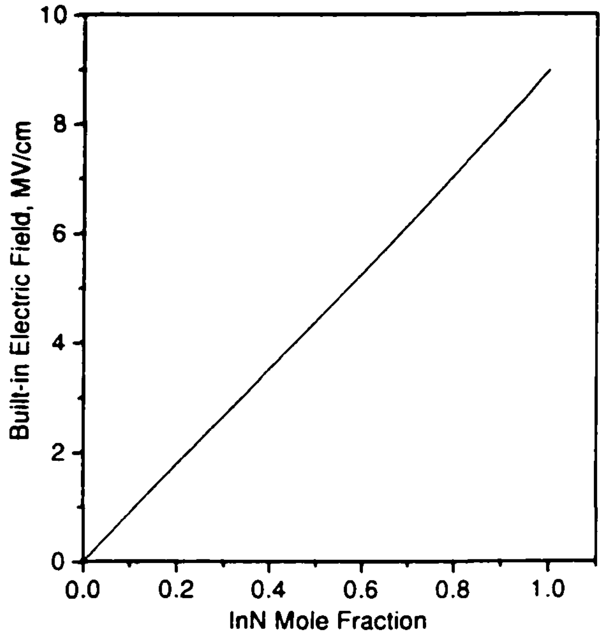

Fig. 2.8. Built-in electric field in the wells of a hypothetical InGaN/GaN structure with 3 nm wells and 5 nm barriers as a function of InN mole fraction.

on the electrical and optical properties of the quantum wells. Figure 2.9 schematically illustrates the change in the band structure and in electron and hole wavefunctions due to the field (quantum confined Stark and Franz-Keldysh effects). The tilt of the band edges significantly reduces the effective bandgap of the electron-hole transition, leading to a red shift of the photo- and electroluminescence from the wells. The electric field also pushes electrons and holes towards the opposite sides of the wells resulting in a reduction of the electron-hole wavefunction overlap and therefore in the increase of the radiative recombination lifetime [61]:

$$\tau \sim \left(\int_{-\infty}^{\infty} dz \psi_e(z) \psi_h(z) \right)^{-2} . \qquad (2.21)$$

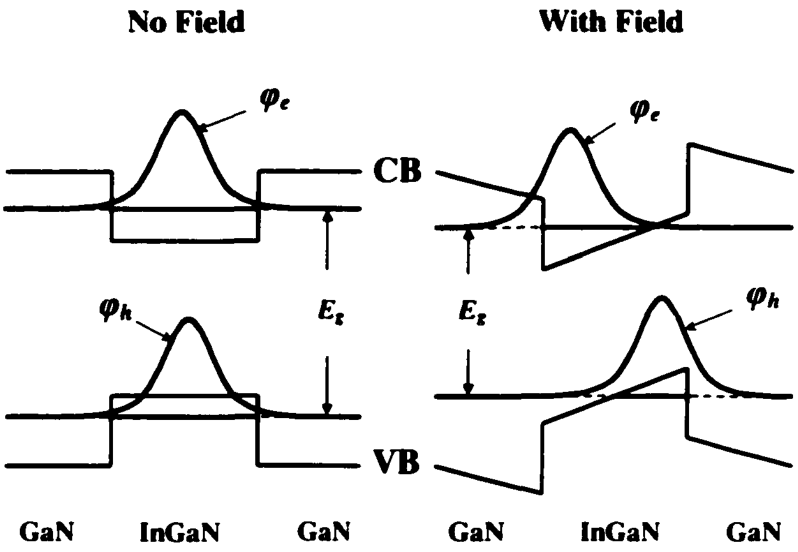

Fig. 2.9. Effect of the built-in electric field in the wells of an InGaN/GaN structure.

In the presence of nonradiative recombination mechanisms the increase of radiative lifetime may lead to a significant reduction of the emission efficiency.

The effects of the built-in electric field on the properties of nitride quantum wells can be mitigated by the injection of the large number of free carriers that would partially screen out the field. This can be achieved by doping the wells and the barriers, by electrical injection of excess carriers, or by the optical excitation. Figure 2.10 shows the conduction band edge profile in a 10 nm wide $In_{0.20}Ga_{0.80}N$/GaN quantum well calculated for several values of free carrier concentrations. At a rather high carrier concentration of $5 \cdot 10^{13}$ cm^{-2}, which is achievable in laser devices with large injection current, the quasi-field-free shape of the band edge can be recovered [62]. Such high carrier concentration required to obtain nearly flat-band condition explains the high threshold injection currents experimentally observed in nitride-based laser diodes.

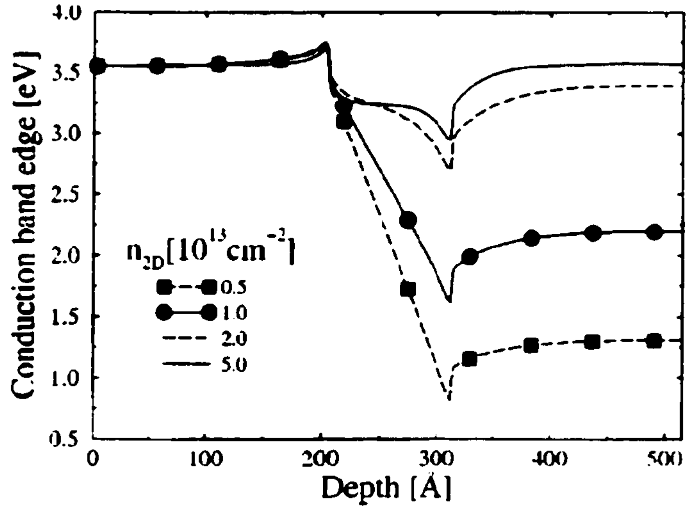

Fig. 2.10. Conduction bandedge profile in a 10 nm wide $In_{0.2}Ga_{0.8}N$/GaN quantum well calculated for several values of free carrier concentrations. After Della Sala *et al.* [62].

2.4. Nonlinear electromechanical properties in group III-nitrides

The description of the macroscopic polarization in nitride alloys and heterostructures presented in previous section assumes that the nature of electromechanical properties of these materials is linear. This notion was accepted in an overwhelming number of scientific publications dealing with polarization in nitrides [11, 40, 63-65]. The linear model of polarization was challenged, however, by the work of Shimada *et al.* [25], who predicted, based on the Berry phase calculations, a significant strain dependence of the piezoelectric coefficients of GaN, AlN and BN. The highly nonlinear nature of the electromechanical interactions in nitrides was also supported by the observation of strong electrostriction effect in GaN reported by Guy *et al.* [66].

The strain dependence of the piezoelectric coefficients and electrostriction are two effects belonging to a broader group that is identified as secondary or nonlinear electromechanical effects. For the crystal experiencing the effects of mechanical stress and electrical field at constant temperature from thermodynamical considerations one can obtain the following expressions for the polarization and stress [67, 68]:

$$P_i = P_i^{sp} + e_{ij}\varepsilon_j + \epsilon_o \chi_{ik} F_k + \tfrac{1}{2} e_{ijl} \varepsilon_j \varepsilon_l + \tfrac{1}{2} \epsilon_o \chi_{ikm} F_k F_m + f_{ikj} F_k \varepsilon_j + \dots, \qquad (2.22)$$

and $$\sigma_j = C_{jl}\varepsilon_l - e_{ij} F_i + \tfrac{1}{2} C_{jln} \varepsilon_l \varepsilon_n - e_{ijl} F_i \varepsilon_l - \tfrac{1}{2} f_{jik} F_i F_k + \dots, \qquad (2.23)$$

where P_i, P_i^{sp}, and F_i are the components of the total polarization, spontaneous polarization, and electric field intensity vectors; ε_i and σ_i are the strain and stress components; e_{ij}, χ_{ik}, and C_{jl} are the piezoelectric coefficients, dielectric susceptibilities, and elastic stiffness coefficients; ϵ_o is the permittivity of free space; e_{ijl}, χ_{ikm}, f_{ikj}, and C_{jln} are the nonlinear electromechanical coefficients defined as [68]:

$$e_{ijl} = -\left(\frac{\partial^2 \sigma_j}{\partial \varepsilon_l \partial F_i} \right)_S = \left(\frac{\partial^2 P_i}{\partial \varepsilon_j \partial \varepsilon_l} \right)_S, \qquad (2.24)$$

$$\chi_{ikm} = \left(\frac{\partial^2 P_i}{\partial F_k \partial F_m} \right)_{S,\varepsilon}, \qquad (2.25)$$

$$f_{ikj} = -\left(\frac{\partial^2 \sigma_j}{\partial F_i \partial F_k} \right)_S = \left(\frac{\partial^2 P_i}{\partial \varepsilon_k \partial F_j} \right)_S, \qquad (2.26)$$

$$C_{jln} = \left(\frac{\partial^2 \sigma_j}{\partial \varepsilon_l \partial \varepsilon_n} \right)_{S,F}, \qquad (2.27)$$

where S is the entropy. The last three terms in the Eqs. 2.22 and 2.23 give rise to the six distinct secondary effects. Following is the description of these effects along with the information available on their role in nitrides.

2.4.1. Nonlinear elasticity

Nonlinear elasticity can be defined as the strain dependence of the elastic stiffness coefficients of a material [69]. It can be understood as the stiffening of the crystal bonds with the reduction of the interatomic distances. For the crystal with no applied electric field from Eq. 2.23 we can write:

$$\sigma_j = C_{jl}\varepsilon_l + \tfrac{1}{2}C_{jln}\,\varepsilon_l\,\varepsilon_n = (C_{jl} + \tfrac{1}{2}\,C_{jln}\,\varepsilon_n)\,\varepsilon_l = C'_{jl}\varepsilon_l\,. \tag{2.28}$$

The term $\frac{1}{2}\,C_{jln}\,\varepsilon_n$ can be viewed as a stress dependent correction to the linear elastic coefficients. Considering this correction we can express the strain-stress relation in the form of the Hooke's law in its traditional form. The elastic coefficients C'_{jl} however are now strain dependent.

The nonlinear elastic properties of materials are most commonly described quantitatively by the third (and higher) order elastic stiffness coefficients C_{jln} [70, 71]. The values of the C_{jln} are usually defined experimentally by measuring ultrasonic velocity in the material as a function of applied uniaxial or hydrostatic pressure. The third order elastic stiffness coefficients were measured in α-quartz [72], GaAs [73], Ge [74], and few other materials, but not in any of the group III-nitrides. To the best of our knowledge there are also no computational works predicting the third order coefficients in nitrides.

Nonlinear elasticity manifests itself in a rather dramatic fashion in the experiments involving application of hydrostatic pressure. Figure 2.11 shows the experimentally determined pressure dependence of the unit cell volume in the GaN. Strain dependence of the elastic coefficients results in a nonlinear volume reduction with pressure, that can be described by the Murnaghan's equation of state [75]:

$$V(p) = V_0\left(1 + p\frac{B'}{B}\right)^{-1/B'} , \qquad (2.29)$$

where V_0 is the volume at zero pressure p, B is the bulk modulus, and B' is its pressure derivative. The latter is in the range of 2.9 - 12.7 in nitrides [76]. For GaN at a pressure of 10 GPa Eq. (2.29) predicts that the volume would deviate from the linear value by ~ 0.6 %, which is a significant effect.

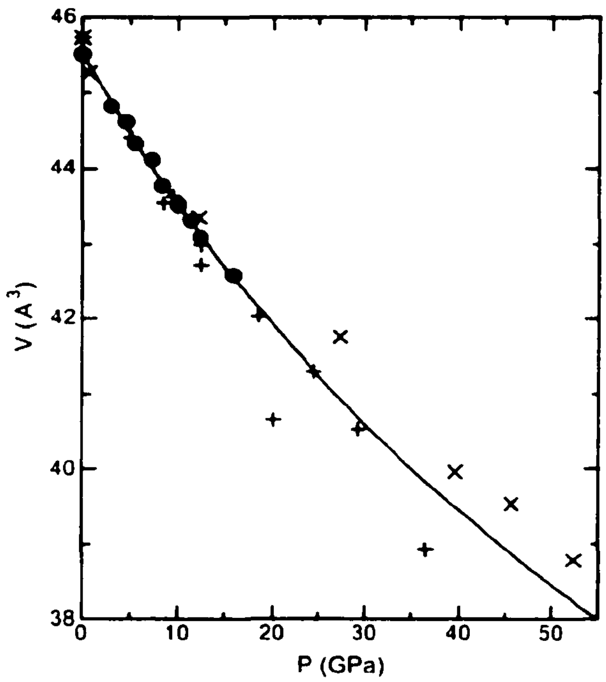

Fig. 2.11. Pressure dependence of the unit cell volume in the GaN. After T. Tsuchiya *et al.* [77].

Kato and Hama [78] calculated the pressure dependence of the individual elastic coefficients of AlN from first principles. The results of these calculations are summarized in Table 2.4. According to this work C_{12} is the most sensitive to applied pressure with $\frac{dC_{12}}{dp} \approx 5$, while C_{33} is the least sensitive with $\frac{dC_{33}}{dp} \approx 0.73$.

Table 2.4. Calculated elastic stiffness coefficients of AlN and their pressure derivatives. After R. Kato and J. Hama [78].

Coefficient	Value, GPa	dC/dp
C_{11}	380	3.3
C_{12}	114	5.0
C_{13}	127	1.9
C_{33}	382	0.73
C_{44}	109	- 0.40
C_{66}	133	- 0.81
B	207	2.3

2.4.2. Electroelastic effect

The electroelastic (also known as elastoelectric or polarizing) effect originates from the dependence of the elastic stiffness coefficients on the applied electric field $C_{ij}(F_i)$. This effect has been extensively studied in quartz in relation to the piezoelectric resonators [79-81]. These works revealed significant dependence of the resonant frequency of mechanical oscillations and the propagation velocity of elastic waves in the presence of the dc electric field applied to the quartz crystals. Electric field of 1 MV/cm applied to this material increases C_{11} by ~ 0.3 % with respect to its field free value [81].

which is a rather small correction. The magnitude of the electroelastic effect in nitrides is presently unknown.

2.4.3. Nonlinear piezoelectricity

The term `nonlinear piezoelectricity` in this dissertation is assigned to the strain dependence of the piezoelectric coefficients e_{ij} (ε_j) [82], although the same definition sometimes is used to describe the whole group of the secondary effects in electromechanical processes [80]. Originally nonlinear piezoelectricity was discovered and investigated in dielectrics [83]. Recently this effect was also detected in cubic CdTe based quantum well structures. The piezoelectric coefficient e_{14} of CdTe was found to increase from 0.07 to 0.15 C/m^2 when the lattice mismatch strain was tuned from – 0.3 to – 1.7 % by changing the alloy composition in the CdZnTe barriers [22, 84]. The e_{14} was also found to significantly increase with the strain produced by hydrostatic pressure [82]. The strong nonlinear piezoelectric effect was explained by the very close in magnitude and opposite in sign internal strain and clamped-ion terms of the piezoelectric coefficient, which nearly cancel each other in the unstrained CdTe. By applying strain one modifies the internal strain term, resulting in a significant change of the e_{14}.

The only work dealing with nonlinear piezoelectricity in nitrides published prior to our investigation is that of Shimada *et al.* [25]. Figure 2.12 shows the piezoelectric constants of GaN e_{33} and e_{31} as a function of applied volume conserving strain determined in this work. The volume conserving (also known in elasticity theory as deviatoric) strain components of the total strain are defined as:

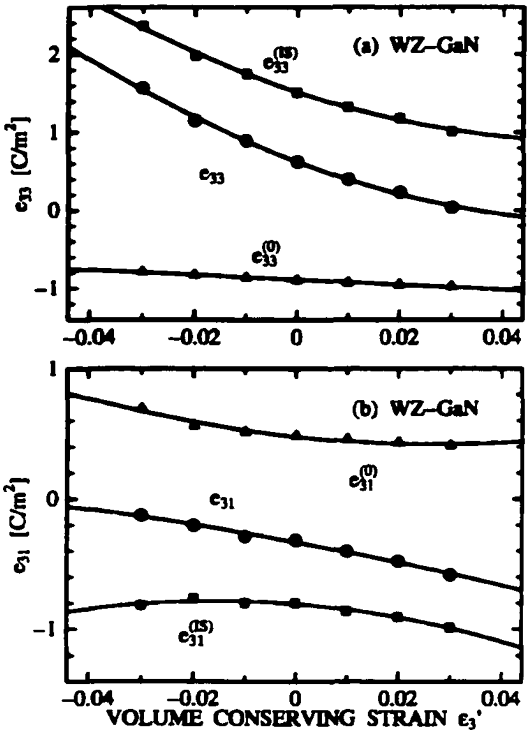

Fig. 2.12. Calculated piezoelectric constants of GaN as a function of applied volume conserving strain. After K. Shimada *et al.* [25].

$$\varepsilon_i^{dev} = \varepsilon_i - \varepsilon^{dil}, \qquad (2.30)$$

where

$$\varepsilon^{dil} = \tfrac{1}{3}(\varepsilon_1 + \varepsilon_2 + \varepsilon_3) \qquad (2.31)$$

defines dilatational (volumetric) strain. The volume conserving strain, although convenient for computational purposes, does not describe any practical strained system, such as strained quantum wells or material subjected to hydrostatic pressure. According to the Fig. 2.12 both the clamped-ion and the internal strain components of the piezoelectric coefficients in GaN change significantly with volume conserving strain. This is the consequence of the modified symmetry of the crystal lattice and in particular the change of the internal parameter *u*. The changes in both components result in a substantial variation of the piezoelectric coefficients with strain. For example e_{33} reduces from 0.63 C/m^2 at equilibrium to 0.23 C/m^2 at $\varepsilon_3^{dev} = 0.02$, while e_{31} changes from – 0.32 to – 0.48 C/m^2 in the same strain range. This significant strain dependence of the piezoelectric constants indicates unusually large nonlinearity of the piezoelectric response of GaN and related materials.

2.4.4. Electrostriction

Electrostriction is traditionally defined as the appearance of mechanical strain proportional to the square of the electric field applied to the material [15, 85]. It can be also described as the electric field dependence of the piezoelectric coefficients e_{ij} (F_j). Unlike piezoelectricity, the electrostriction is possible in materials with all types of symmetry and even in glasses and liquids. In most of materials this effect is very small in magnitude. The most notable exception is the case of ferroelectrics, where the electrostrictive strains can be very large due to the reorientation of domains in electric fields.

The only study of electrostriction in nitrides published so far is that by Guy *et al.* [66], who showed experimentally strong electrostriction effect in wurtzite GaN films. The measured value of the electrostriction coefficient M_{333} in this work is $1.2 \cdot 10^{-18}$ m^2/V^2, which makes the electrostriction contribution to the ε_3 component of strain equal to that of the piezoelectricity at an applied field of ~ 0.83 MV/m. Based on the observation of such strong electrostriction effect in GaN Guy *et al.* [66] predicted that the effective dielectric constants of GaN are strongly affected by the strain (converse electrostriction).

and that the piezoelectric coefficients are significantly altered by the applied electric fields.

2.4.5. *Photoelastic effect*

The change of the index of refraction n caused by stress (strain) is called photoelastic effect [15]. In the notations of the Eqs. (2.22) and (2.23) this effect is equivalent to the strain dependence of the dielectric constants and dielectric susceptibilities of material $\chi_{ij}(\varepsilon_j)$. As in the case of nonlinear piezoelectricity, photoelastic effect arises due to the changes in the crystal symmetry produced by strain. Although there is no complete description of the photoelastic effect in nitrides the magnitude of this effect is evident from the existing studies of the pressure dependence of the index of refraction [86, 87]. According to the calculations in Ref. 87, InN has the strongest dependence of the index of refraction on pressure, reducing from $n \approx 2.87$ at atmospheric pressure to $n \approx 1.89$ at 10 GPa. This result, however, is in disagreement with the prediction of the Ref. 86, suggesting more conservative $n \approx 2.75$ at 10 GPa. Experimentally measured dn/dp for GaN [88] slightly favors values predicted in the Ref. 86.

2.4.6. *Electrooptical effect*

Electrooptical effect reflects the dependence of the dielectric susceptibility on the electric field $\chi_{ij}(F_j)$. Most of studies of this effect in nitrides so far were aimed at defining high frequency nonlinear susceptibilities in relation to the optical harmonics generation

[89 - 91]. In this dissertation we are, however, concerned about the static response of the material. Although the static nonlinear susceptibilites of nitrides were not directly measured (to the best of our knowledge), they can be extrapolated from the experimental data applying Miller's rule [92]. Thus, in GaN, for instance, $\chi_{333}(0) = -10.7$ pm/V [91]. At an applied electric field of 1 MV/cm the electrooptic effect will reduce χ_{33} by 0.001, which is fairly insignificant contribution.

2.5. Important experimental studies in nitride quantum wells

2.5.1. Carrier localization effects

One of the most astounding findings in the early studies of InGaN/GaN quantum wells was the high efficiency of light emission despite the extremely large density of dislocations in such structures [92]. Figure 2.13 shows the cross section transmission electron microscope (TEM) image of a commercial LED with high emission efficiency. The dislocation density in this device was estimated to be $2\text{-}10\times10^{10}$ cm^{-2}. In comparison, the efficiencies of the GaAs based LEDs are limited by dislocations at typical densities of 10^4 cm^{-2}. To explain this striking contrast between these materials it was initially proposed that the dislocations in GaN do not act as nonradiative centers [92]. This explanation was later challenged by the extensive experimental data showing that the dislocations in GaN are indeed electrically active [93, 94]. To resolve this dilemma it was proposed that although the dislocations act as nonradiative centers, the carriers in the

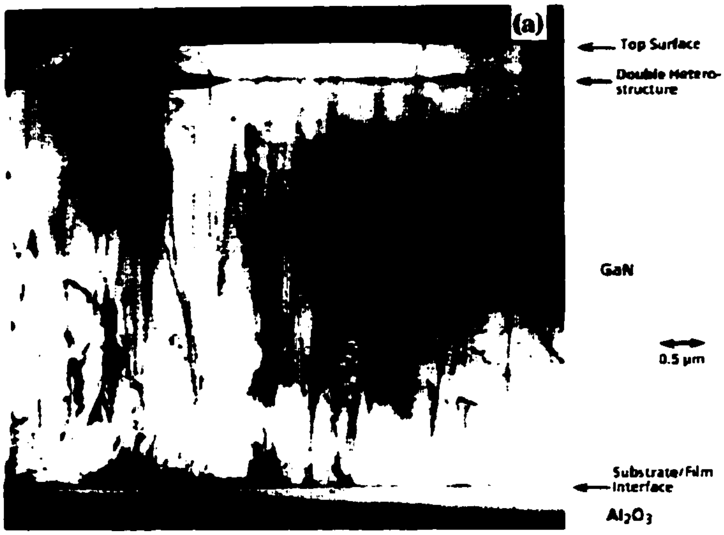

Fig. 2.13. Cross section TEM image of a commercial InGaN/GaN LED structure with high emission efficiency. After S. D. Lester *et al.* [92].

active InGaN layers are localized, and therefore they avoid being trapped at dislocations [95 - 97]. This model was supported by the experimental observation of extremely broad (FWHM ~ 200 meV) electroluminescence peaks, large red shift (Stoke's shift) of emission peaks with respect to absorption features (Fig. 2.14), and by very long (compared to that in GaN), on the order of 2 – 4 ns, emission decay times.

Several mechanisms of carrier localization in InGaN quantum wells were proposed. The most popular model suggests that the InGaN alloy inhomogeneity is the origin of the potential fluctuations in the quantum wells giving rise to localization of carriers in the excitonic form (Coulomb attracted electron-hole pairs) [97]. The mechanism of carrier localization at In-rich clusters (quantum dot-like formations) is shown schematically in Fig. 2.15. Broad emission peaks according to this model are the result of statistical distribution of the cluster sizes and InN mole fraction. The large

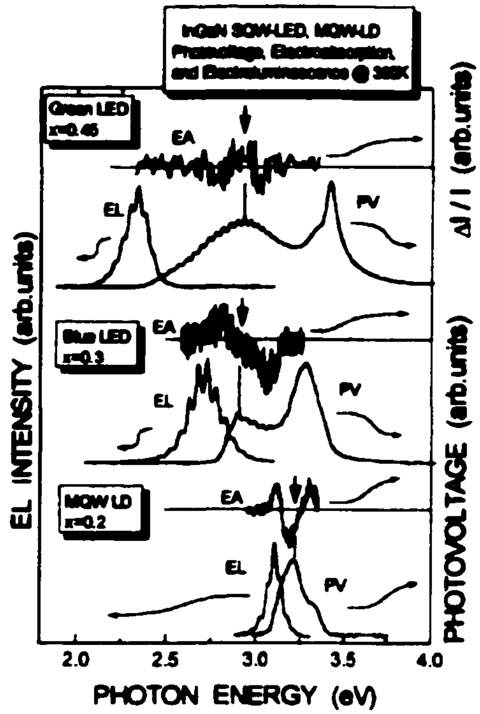

Fig. 2.14. Electroluminescence (EL), photovoltage (PV), and modulated electro-absorption (EA) spectra of three InGaN/GaN LEDs with varying InN mole fraction in the wells x. Vertical arrows indicate position of the absorption edge. After Chichibu *et al.* [95].

Stoke's shift is due to the fact that the absorption takes place over the whole range of available bandgap states, while the emission originates from the occupied energy states only, i.e. from the localized states with lowest energy. And finally, the long emission decay time can be explained by the 0D exciton confinement effect that increases wave vector uncertainty of the confined excitons at the expense of the reduced oscillator strength [98].

The physical reason for large inhomogeneity of InGaN lies in large difference in interatomic spacing between GaN and InN. Ho and Stringfellow predicted that because of

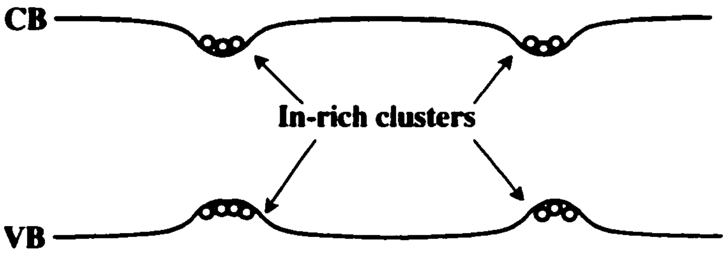

Fig. 2.15. Carrier localization on In-rich clusters in nonuniform InGaN alloy. Areas with larger than average In concentration have smaller bandgap energy than the surrounding areas.

this difference the maximum bulk solubility of In in GaN under typical epitaxial growth conditions should be less than 6 % [99]. In incorporation beyond this concentration would result in a formation of the In-rich clusters. The situation with the quantum wells as opposed to the bulk material could be somewhat different, as the surface effects and nonequilibrium conditions of the epitaxial growth techniques may significantly alter the energetics of the In incorporation and the homogenious alloy with In composition larger than 6 % can be obtained [100 - 102]. Figure 2.16 shows the high resolution TEM image of the $In_{0.20}Ga_{0.80}N/In_{0.05}Ga_{0.95}N$ quantum well region of a laser structure confirming the model of In clustering [103]. The dark areas in this image indicate In-rich material. The quantum well region appears as a set of layers of quantum dot-like features.

Another mechanism of localization proposed for InGaN is that of the hole wavefunction localization [102, 104]. Using large scale atomistic pseudopotential calculations Bellaiche *et al.* [102] showed that even in the absence of In segregation in perfectly random InGaN alloy the holes tend to be localized at the In atoms, while the electron wavefunctions are uniformly extended. This localization appears due to the

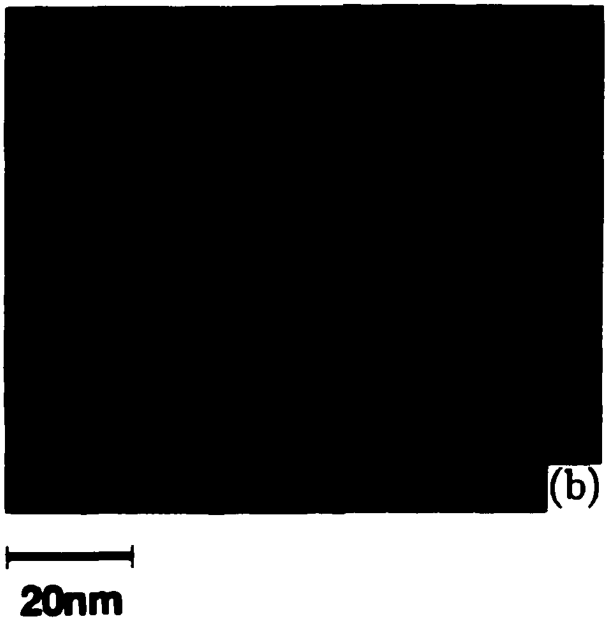

Fig. 2.16. TEM image of the $In_{0.20}Ga_{0.80}N/In_{0.05}Ga_{0.95}N$ quantum well region of a purple laser structure. The dark areas in this image indicate In-rich material forming quantum dot-like features instead of uniform quantum wells. After Narukawa *et al.* [103].

microscopic difference in potentials of the alloyed atoms, around the In-rich atomic chains (In-N-In) spontaneously formed along the (110) direction [104]. Figure 2.17 shows the calculated wavefunctions of the conduction and valence states in the random InGaN alloy with InN mole fraction 0.20. The hole localization, as the exciton localization on alloy nonuniformities, can be responsible for the observed efficient emission from the quantum well devices, large Stoke's shift of emission, and long PL decay times.

The third type of localization is that due to the well width fluctuations. Unlike the first two mechanizms this one may appear not only in the InGaN/GaN structures, but also in the GaN/AlGaN, where the wells are formed by the binary GaN [105, 106]. Even a

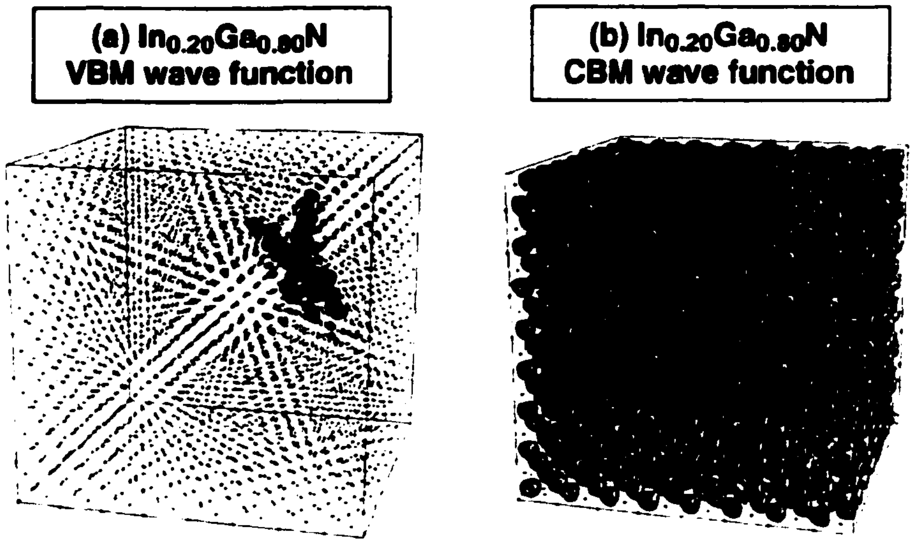

Fig. 2.17. Calculated squared wave function of the valence (a) and conduction (b) band states of $In_{0.20}Ga_{0.80}N$ alloy. The isosurfaces correspond to 75% of the integrated charge. After P. R. C. Kent and A. Zunger [104].

variation of the well width by one atomic monolayer (~ 0.26 nm) in the 2.5 nm $GaN/Al_{0.93}Ga_{0.07}N$ quantum wells produces local potential minima 15 meV deep, which is sufficient to localize excitons at low temperature [107]. This localization can be experimentally confirmed by the observation of the dispersion of the quantum well decay time. The localized excitons having lower energy show longer decay times than the free excitons responsible for the higher energy tail of the emission line (Fig. 2.18). In the quantum well structures with larger Al (In) composition the effect of this localization can be more pronounced and may persist even above the room temperature. In $GaN/Al_{0.80}Ga_{0.20}N$ system, for instance, a single monolayer well width fluctuation produces potential fluctuations of ~ 100 meV, which are mainly due to the large polarization induced electric field across the wells. The fluctuations on this scale can explain not only the dispersion of the carrier lifetimes, but also the significant PL line broadening experimentally observed in such structures [108].

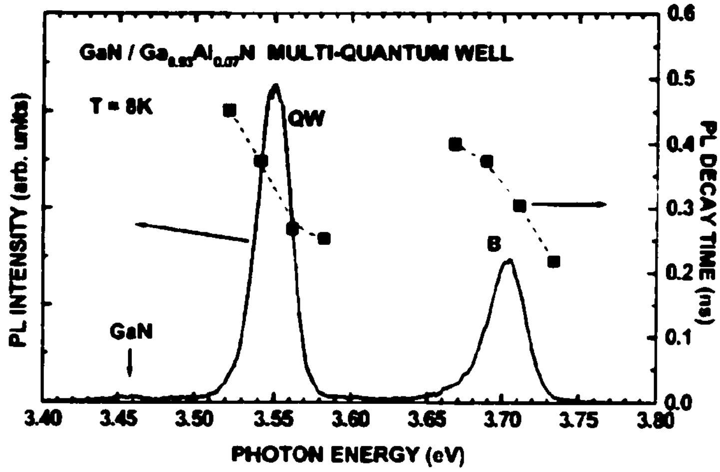

Fig. 2.18. Low temperature (T = 8 K) time-integrated PL spectrum of the GaN quantum well (QW) and $Al_{0.93}Ga_{0.07}N$ (B) emission. Squares show the spectral variation of the exponential decay time. After P. Lefebvre *et al.* [105].

2.5.2. Polarization-induced electric fields

First experimental demonstration of the effect of polarization-induced electric field in nitride heterostructures was accomplished by Bykhovski *et al.* in 1995 [109]. In this work the current-voltage characteristics of the symmetrically *n*-doped GaN-AlN-GaN structures with the AlN layer thickness varying from 3 to 10 nm were experimentally investigated and compared with calculations that included the effect of the polarization-induced electric field. Figure 2.19 shows the results obtained for the 3 nm AlN layer. Good agreement between the model and the experiment suggests the presence of the polarization induced field in the studied structures.

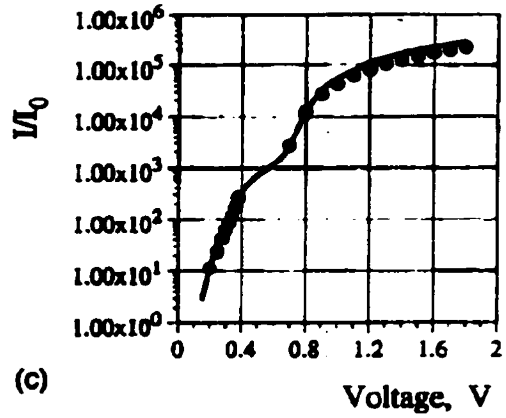

Fig. 2.19. Calculated (solid line) and experimental (circles) forward current in GaN/AlN/GaN structure with 3 nm AlN layer. The model used in calculations includes the effect of piezoelectric field. After A. Bykhovski *et al.*[109].

The effect of the built-in electric field on the optical properties of nitride heterostructures was experimentally investigated for the first time by T. Takeuchi *et al.* [110]. The PL from the $In_{0.13}Ga_{0.87}N/In_{0.03}Ga_{0.97}N$ multiple quantum wells with varied width (2-11.5 nm) and in a 40 nm single layer was measured at different optical excitation densities. The quantum well PL peaks were found to shift significantly with excitation density, while the thick layer did not show any considerable shift. The shift in the quantum wells was explained by the screening of the piezoelectric field, while the lack of the shift in the 40 nm layer was explained by the "inadequate confinement" of the carriers [111]. The blue shift of emission is also expected in the system with carrier localization due to the filling the lower energy states with abundant carriers. However, Takeuchi *et al.* showed that this blue shift significantly increases with increasing well width (Fig. 2.20), the finding that is consistent only with the effect of the electric field.

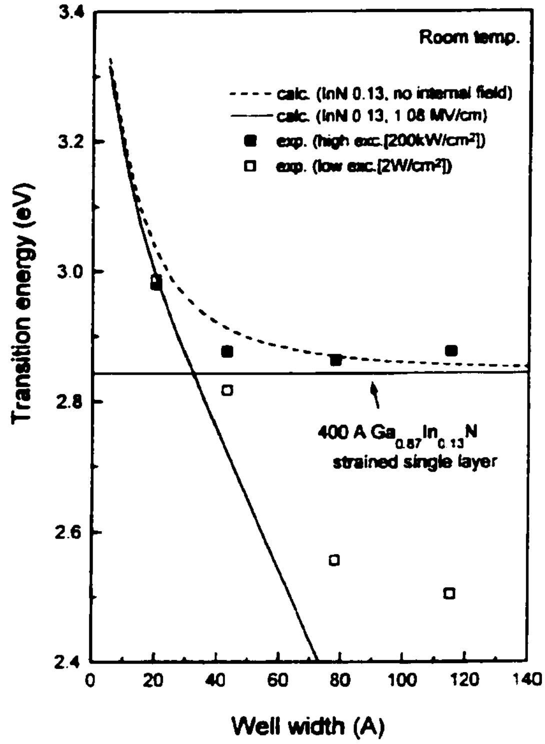

Fig. 2.20. Calculated (solid and dashed lines) and experimental (squares) PL peak energies of the $In_{0.13}Ga_{0.87}N/In_{0.03}Ga_{0.97}N$ quantum wells. The increase of the red shift with well width at low excitation (open squares) suggests the presence of large polarization induced built-in electric field. After T. Takeuchi *et al.*[110].

The role of spontaneous polarization in the built-in electric fields in GaN/AlGaN quantum well structures was investigated by Langer *et al.* [112]. PL peak energies of the samples with Al composition in the barriers of 24 % were studied as a function of well width (Fig. 2.21(a)). The best fit to the experimental data was obtained with the value of the built-in field of 1.5 MV/cm. This value of the field was also confirmed by the comparison of the measured and calculated (for the field of 1.5 MV/cm) PL decay time dependence on the well width (Fig. 2.21(b)). Since the piezoelectric contribution to the total polarization difference in this combination of materials is rather small (§ 2.3), this built-in electric field is mostly the result of the difference in the spontaneous polarization between the GaN and AlGaN.

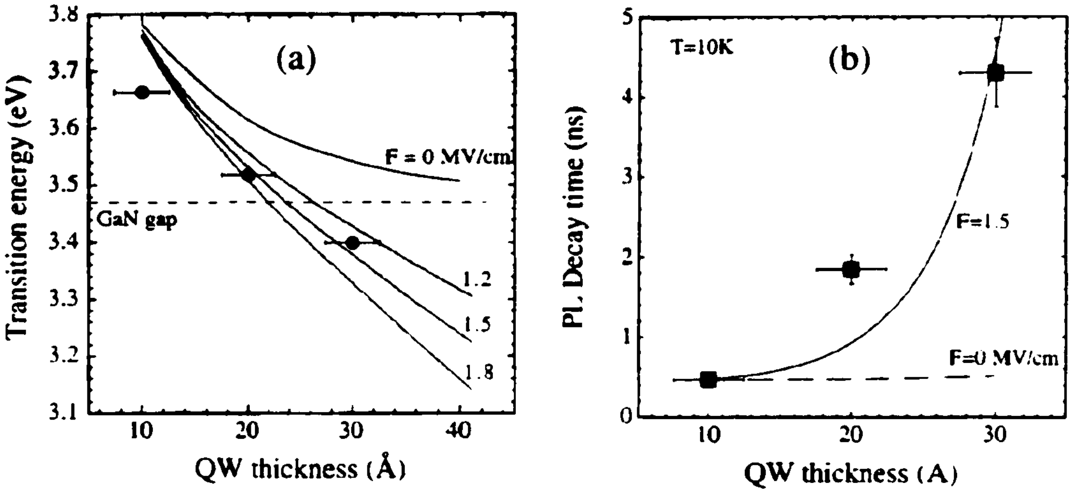

Fig. 2.21. PL peak energies (a) and decay times (b) in the GaN/Al$_{0.24}$Ga$_{0.76}$N quantum wells. After R. Langer *et al.*[112].

Among the other important experimental studies of the polarization induced electric fields in nitride heterostructures one can also select the works by Wetzel *et al.* on defining the magnitude of the field from the Franz-Keldysh oscillations [113, 114], the observation of the microsecond range PL decays in the GaN/AlGaN quantum wells by Im *et al.* [115], and characterization of the built-in fields in nitride heterostructures by electron holography carried out by Cherns *et al.* [116].

2.5.3. Pressure studies

Very often to single out certain physical process in semiconductors one needs to change a condition that affects this process without affecting the other. Such conditions that can be changed are few in number: temperature, electric or magnetic field, injected carrier concentration, and mechanical stress. The latter, when applied as hydrostatic pressure, provides a unique opportunity to continuously tune the strain in the different layers of a semiconductor structure, thus changing the energy bands and affecting polarization. Since the experimental evidence on the optical properties of nitride heterostructures often can not be uniquely assigned to the localization or built-in effects, the pressure is the tool that can potentially help to solve this problem. That is why a large number of studies were dedicated to the investigation of the optical properties in nitride heterostructures under applied pressure [117 - 121].

The most common observation in the pressure studies of the InGaN/GaN PL is the anomalously small pressure coefficient (*dE/dp*) of emission peaks. Perlin *et al.* [117] measured pressure dependence of PL in commercial LED structures with InN mole fraction in the wells of 0.15 and 0.45. They found pressure coefficients of 16 and 12 meV/GPa for the two types of structures respectively, much smaller than experimentally determined *dE/dp* in GaN epilayers (~ 47 meV/GPa) [88] and that expected for InN from theoretical computations (~ 33 meV/GPa)[86]. To explain the small pressure coefficients of the quantum well PL Perlin *et al.* [117] proposed that the emission in these structures originates from the highly localized bandtail states associated with the alloy fluctuations or structural defects. The deep energy states are normally expected to have the pressure dependence different than that of the host material since the defect potential does not depend on the bond length [122].

Another explanation of the anomalous pressure behaviour of the InGaN/GaN quantum wells was suggested by Shan *et al.* [118]. In this work the pressure behaviour of PL and photomodulated transmission (PT) spectra of the $In_{0.15}Ga_{0.85}N$/GaN multiple quantum wells was compared to that of the $In_{0.11}Ga_{0.89}N$ thick epilayer. Shan *et al.* have found that the pressure coefficient of the quantum well PL (28 meV/GPa) is almost equal to that of the PT peak, which is related to the absorption edge in the wells. Based on this finding Shan *et al.* suggested that the PL originates from the effective mass band edge states, thus ruling out the involvement of the deep localized states in the emission. Furthermore, it was shown that the pressure dependence of the $In_{0.11}Ga_{0.89}N$ epilayer is very similar to that of the GaN (the measured dE/dp = 40 meV/GPa). The peculiar behaviour of the quantum wells was attributed therefore not to the InGaN material, but to the mechanical arrangement of the structures, where the quantum wells are surrounded by the GaN barriers with different than InGaN mechanical properties. The small dE/dp in the wells was explained by the larger bulk modulus of the GaN among the two materials, leading to the uniaxial (tensile) strain in the wells that partially compensates the effect of the hydrostatic pressure.

The basis of the Shan's analysis is the assumption that under the applied pressure the quantum wells are pseudomorphically strained to the GaN barriers, and therefore the changes in the c lattice constant of InGaN with pressure are governed by the Poison's relation to the pressure-induced changes in the a lattice constant:

$$\frac{\Delta c}{c} = -2\frac{C_{13}}{C_{33}}\frac{\Delta a}{a}. \tag{2.32}$$

This expression, that can be easily obtained from Eq. (2.2), accurately describes the change of c under the action of the in-plane strain only in case of vanishing stress along the [0001] direction of the crystal $\sigma_3 = 0$. When hydrostatic pressure is applied this stress component is $\sigma_3 = -p$, and therefore Eq. (2.32) does not hold. We therefore can conclude that the model suggested by Shan *et al.* [118] is not accurate. This, however, should not reduce the importance of the experimental observations of this work proving that the bandgap states and not the deep levels are responsible for emission in InGaN/GaN quantum wells.

The third explanation of the anomalous pressure response of the InGaN quantum wells was suggested by Weinstein *et al.* [119]. In this work the pressure coefficient of the bulk InN in zincblende phase was calculated from the first principles and found to be 19 meV/GPa, much smaller than that of the wurtzite InN. It was therefore proposed that the emission in InGaN/GaN quantum wells actually originates from the InN quantum dot-like inclusions with cubic phase. Considering the effect of pressure on the electron effective mass Weinstein *et al.* estimated the pressure coefficient of PL from such inclusions to be in the range of 14 – 19 meV/GPa, in reasonable agreement with the findings of the work by Perlin *et al.* [117].

Summarizing this chapter, we presented here the brief review of the major physical properties of group III-nitrides and their alloys and heterostructures. As follows from this review, some of the properties of these materials are not yet clearly defined. Among the less investigated properties of nitrides are the nonlinear electromechanical interactions and the optical properties. Namely, the mechanism of the radiative recombination and the effects of hydrostatic pressure need further exploration. In the following chapters of this dissertation we provide the description of the experimental conditions, results, and analysis of our study of nitride heterostructures, where the above mentioned problems are in the focus of investigation.

3. Experiment

3.1. Samples description

Two sets of quantum well structures and one epilayer were investigated in this work. Characteristics of these structures are summarized in Table 3.1. The first set of samples (A1 – A3) was prepared at LumiLeds Lighting company using metal organic chemical vapor deposition (MOCVD) on (0001) sapphire. This set consists of three InGaN/GaN structures with well widths of 2.5, 3.1, and 3.8 respectively (Fig. 3.1). Each sample has four identical quantum wells separated by 12.5 nm Si doped (~ 10^{18} cm^{-3}) GaN barriers. The InN mole fraction in the wells is 0.15. The well and barrier width, as well as InN mole fraction estimated from the growth parameters were confirmed with X-ray diffraction (XRD) measurements. The QW regions are grown on 3.5 μm GaN:Si buffer layers.

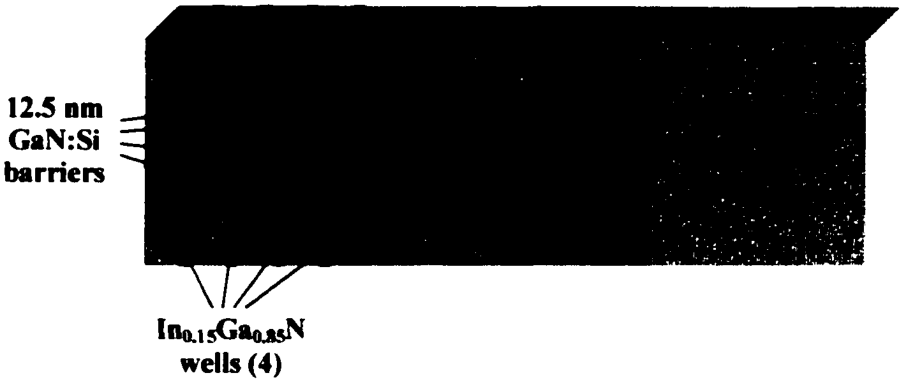

Fig. 3.1. Structure of the InGaN/GaN quantum well samples A1 - A3.

The InGaN epilayer (B1) was grown at the University of California at Santa Barbara (UCSB) by MOCVD on (0001) sapphire. The InN mole fraction in this sample is 0.11. The epilayer is 80 nm thick and is deposited on a 2 μm GaN buffer layer (Fig. 3.2).

Fig. 3.2. Schematic diagram of the InGaN epilayer B1.

The second set of the quantum well samples (C1 – C3) was grown at Bell Laboratories, Lucent Technologies by plasma-assisted molecular-beam epitaxy (MBE) also on (0001) sapphire substrates. Three GaN/AlGaN structures have similar geometry and differ by the AlN mole fraction in the barriers, which is 0.20, 0.50, and 0.80 respectively. The AlN mole fraction was estimated from the results of the XRD measurements. Each sample has four GaN quantum wells 1.8, 2.9, 3.9, and 4.9 nm thick, separated by the 5.2 nm AlGaN barriers (Fig. 3.3). The well widths and interface quality were investigated with transmission electron microscopy (Fig. 3.4). The quantum well regions of these samples were not intentionally doped. The background doping concentration is found to be $\sim 10^{17}$ cm^{-3}.

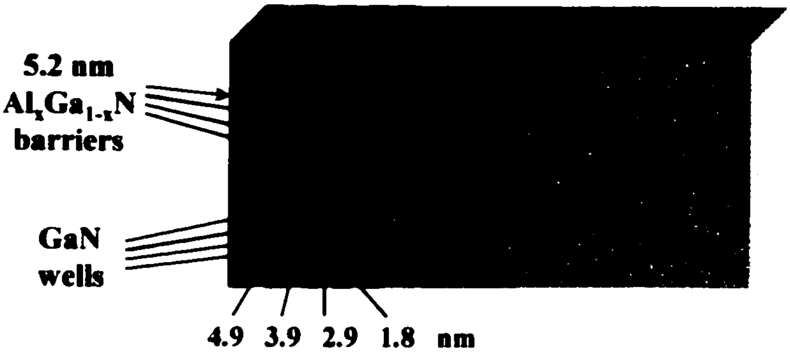

Fig. 3.3. Schematic diagram of the GaN/AlGaN quantum well structures C1 - C3.

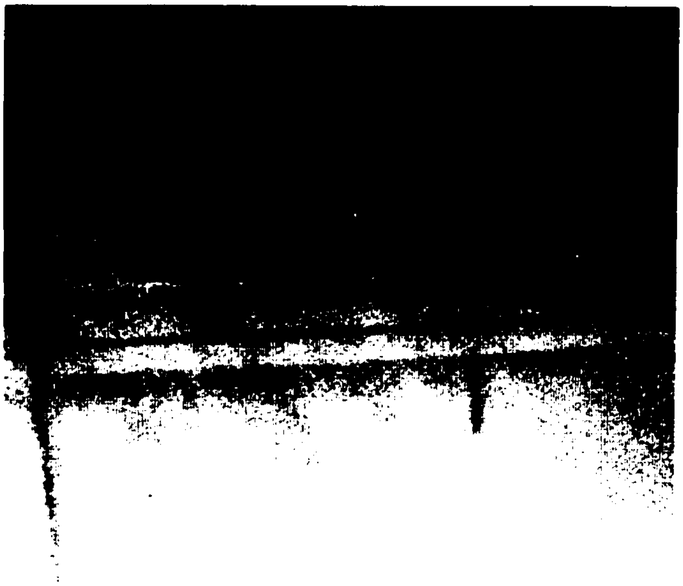

Fig. 3.4. Cross-sectional TEM image of the sample C3. Dark horizontal lines represent the GaN layers, while the light grey lines are AlGaN wells.

Table 3.1. Summary of the parameters of investigated samples.

Sample	# of wells	Well material	Well width, nm	Barrier material	Barrier width, nm	Doping concentration, cm^{-3}
A1	4	$In_{0.15}Ga_{0.85}N$	2.5	GaN:Si	12.5	10^{18}
A2	4	$In_{0.15}Ga_{0.85}N$	3.1	GaN:Si	12.5	10^{18}
A3	4	$In_{0.15}Ga_{0.85}N$	3.8	GaN:Si	12.5	10^{18}
B1	Epilayer	$In_{0.11}Ga_{0.89}N$	80.0	NA	NA	NA
C1	4	GaN	1.8, 2.9, 3.9, 4.9	$Al_{0.20}Ga_{0.80}N$	5.2	10^{17}
C2	4	GaN	1.8, 2.9, 3.9, 4.9	$Al_{0.50}Ga_{0.50}N$	5.2	10^{17}
C3	4	GaN	1.8, 2.9, 3.9, 4.9	$Al_{0.80}Ga_{0.20}N$	5.2	10^{17}

3.2. Details of experimental techniques

Experimental techniques implemented in this work include time integrated and time resolved photoluminescence (PL) spectroscopy, and pressure dependent photoluminescence spectroscopy. A schematic diagram of the time resolved photoluminescence experimental set-up is shown in Fig. 3.5. To excite the PL in wide bandgap nitride samples we have developed a frequency tripler for the existing self-mode-locked titanium sapphire (Ti:S) laser, that increases the photon energy of the pulsed emission from ~ 1.55 eV (800 nm) to ~ 4.65 eV (267 nm). The output emission of the tripler consists of ~ 100 fs pulses at a repetition rate of 82 MHz with average power

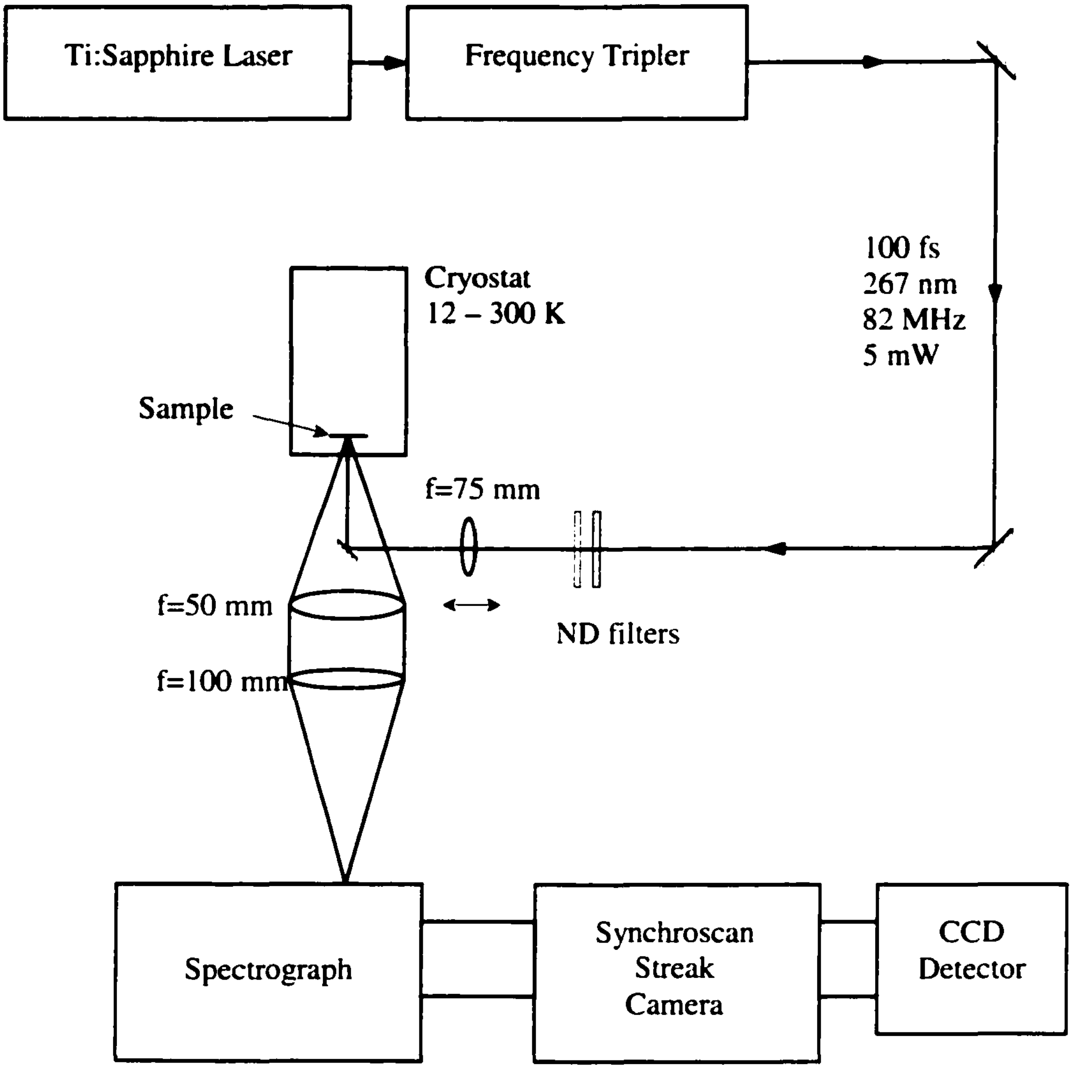

Fig. 3.5. Schematic diagram of the time-resolved photoluminescence set-up.

of 5 mW. This emission is delivered through a variable attenuator to the nitride sample mounted in a closed cycle cryostat (CTI-Cryogenics, Model 22). The temperature of the sample can be tuned between 12 and 300 K. The excitation beam is focused on the sample surface with a 75 mm focal length lens. The corresponding spot diameter on the sample surface is estimated to be ~ 6.3 μm. The excitation power density can be varied in experiment from ~ 50 mW to ~ 2 kW/cm^2

The PL emission from the investigated sample is collected in a backscattering configuration from the sample surface with a 50 mm focal length lens. The collimated PL beam is focused with a 100 mm lens onto the input slit of a 0.3 meter triple grating spectrograph. Two different gratings, 150 and 600 grooves/mm, are used in PL detection. The corresponding spectral resolution is 0.5 and 0.12 nm respectively. The output slit of the monochromator was removed and replaced with the input slit of a synchroscan streak camera oriented along the spectral axis (for the time-resolved measurements), or with a CCD camera (for the time-integrated measurements). The CCD is a liquid nitrogen cooled, back-illuminated Princeton Instruments, Model LN/CCD-1100PB. The streak camera is home built. It has a temporal resolution of 4 ps. In some time resolved measurements with the decay time longer than 10 – 20 ns we used a fast photomultiplier tube (Hamamatsu Model H6779) in conjunction with a 500 MHz digital oscilloscope (Hewlett Packard Infinium) in accumulation mode. The time resolution of this combination is ~ 0.8 ns.

The pressure dependent PL set up is similar to the one just described, except for the samples being placed in a gasketed diamond anvil cell. The diamond cell used in this work has a standard Merril-Bassett [123] configuration that is shown in Fig. 3.6. To apply hydrostatic pressure the samples are cut to a 70×70×30 μm size to fit in a 100 μm gasket. The volume between the diamonds surrounding the sample is filled with liquid argon that serves as a pressure transmitting media. The pressure is determined from the wavelength of the R_2 emission line of a small piece of ruby crystal placed next to the sample in the cell [123]. To reduce nonhydrostaticity effect (nonuniformity of applied pressure) the pressure was increased at room temperature where argon is softer, while all measurements were done at 35 K [124]. This is the lowest temperature achievable in our cryostat with the additional load to the cryostat's cold finger provided by the diamond cell.

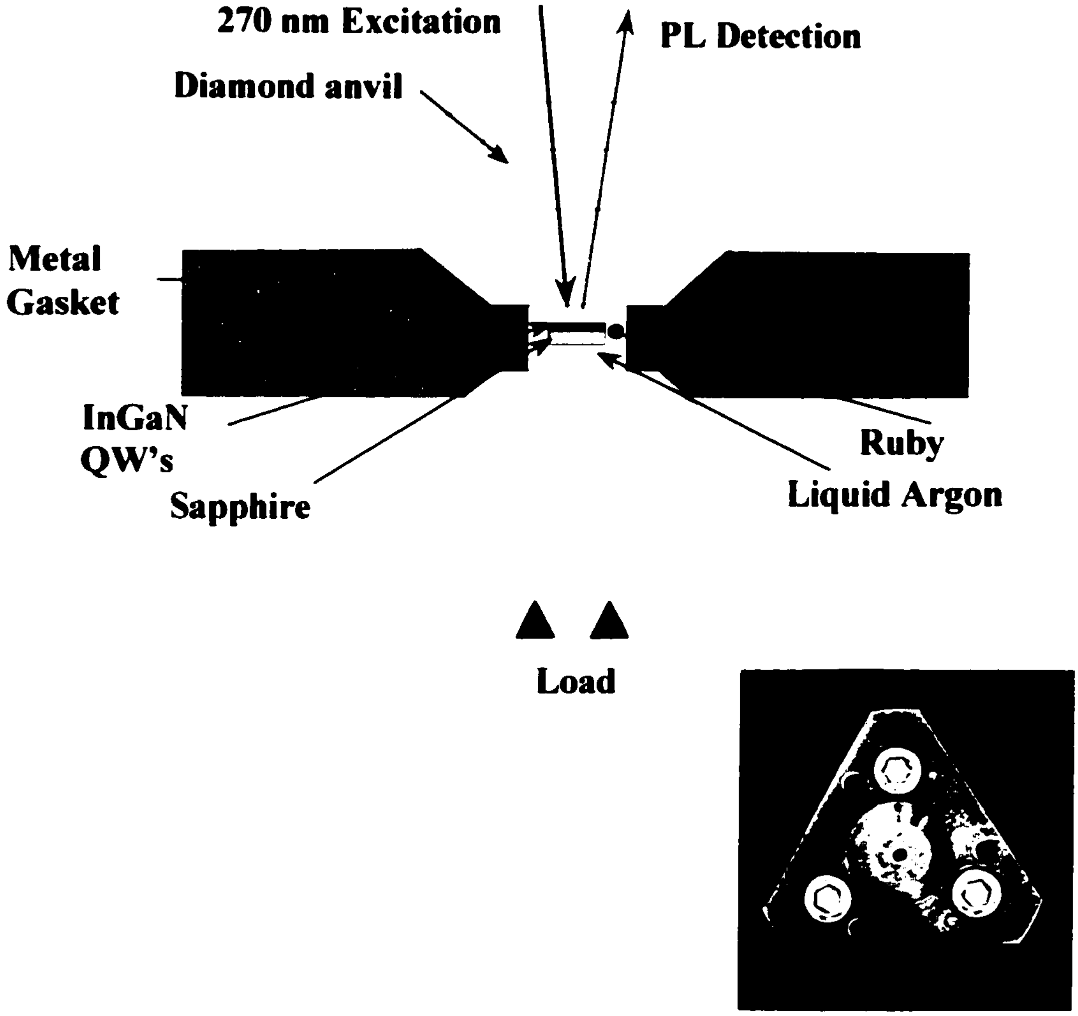

Fig. 3.6. Schematic cross-section of a diamond anvil cell (top), and the actual size picture of the cell used in this work (lower right).

4. Experimental results

4.1. Pressure measurements in InGaN/GaN quantum wells and InGaN epilayer

Figure 4.1 shows typical PL spectra of InGaN/GaN quantum well structure with 3.1 nm wells obtained at varied applied pressure and temperature of 35 K. The main effect of pressure is a significant shift of the PL peak towards higher photon energy. The PL line is characterized by large width that increases from ~ 80 meV full width at half

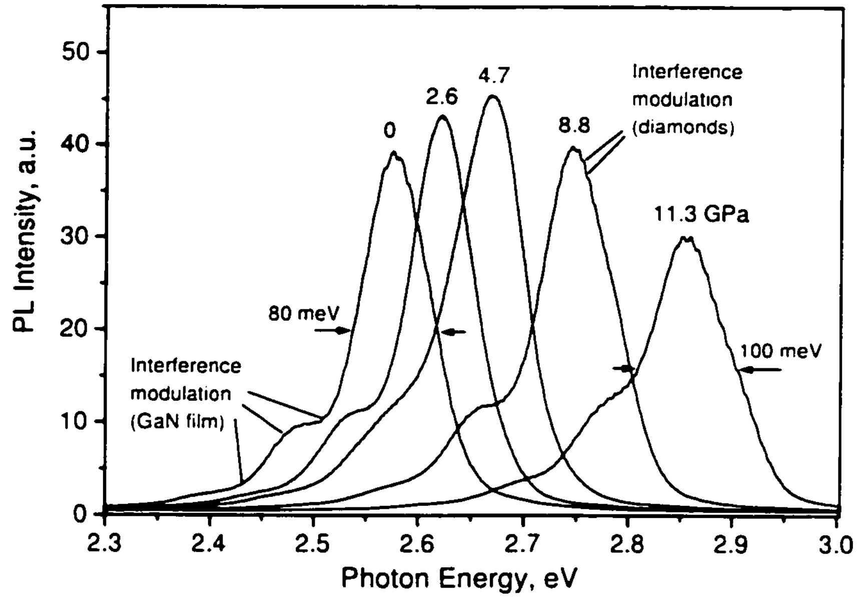

Fig. 4.1. Photoluminescence obtained from a $In_{0.15}Ga_{0.85}N$/GaN quantum well structure with 3.1 nm wells at different applied pressures. The pressures are labeled above the PL peaks in GPa. The PL was obtained at 35 K with optical excitation intensity of ~ 200 W/cm^2 at 270 nm.

maximum (FWHM) at atmospheric pressure to ~ 100 meV at 11.3 GPa. The low energy side of the PL line is modulated by the optical interference pattern produced due to the reflection of PL emission at the air/GaN and GaN/Sapphire interfaces. The high frequency ripple with small modulation amplitude that is present in some of the PL spectra is the result of the interference of the PL reflected from the diamond faces. The integrated PL intensity does not change significantly with applied pressure. The samples with 2.5 and 3.8 nm wells show qualitatively similar behavior to that of the 3.1 nm structure, except for the magnitude of the PL peak shift with pressure.

Figure 4.2 summarizes the pressure dependence of the PL peak energy in InGaN/GaN quantum well structures and GaN layers obtained at excitation intensity of

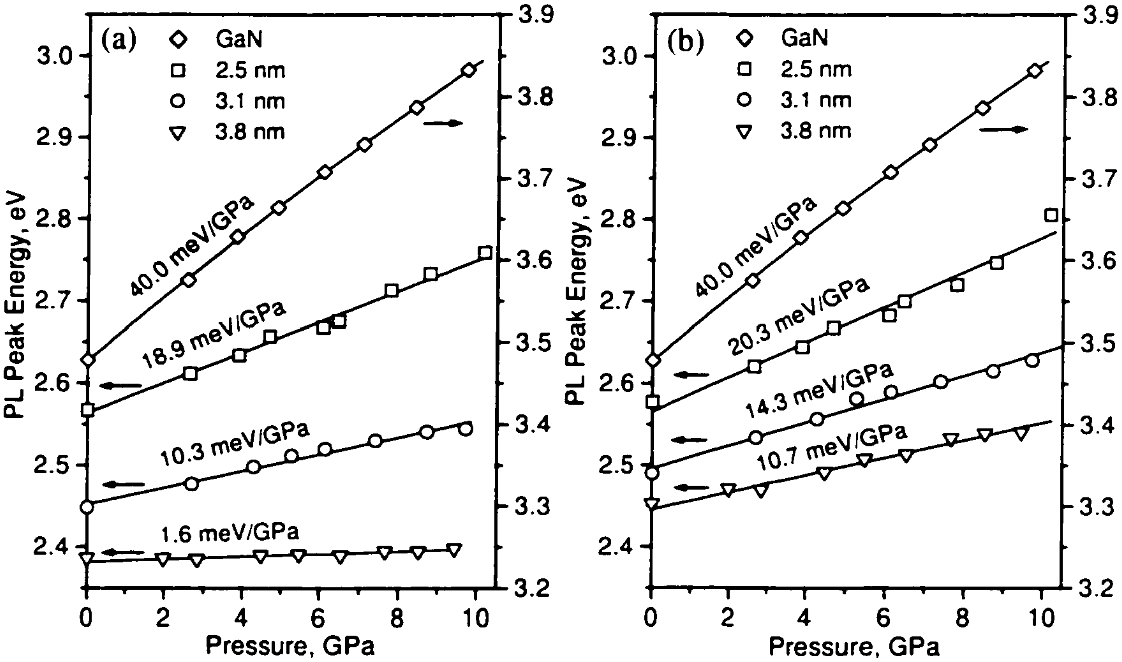

Fig. 4.2. Pressure dependence of the PL peaks in $In_{0.15}Ga_{0.85}N$/GaN quantum wells and GaN layers obtained with optical excitation intensity of 2 W/cm^2 (a), and 200 W/cm^2 (b). Data points are fitted with strait lines for the quantum well PL peaks and with second-order polynomial for GaN to determine the pressure coefficients. The pressure coefficients are shown above the lines. Measurements were done at 35 K.

2 W/cm^2 (Fig. 4.2(a)) and 200 W/cm^2 (Fig. 4.2(b)). At both excitation intensities the pressure coefficients of quantum well PL peaks are significantly smaller than that of the GaN layers. Also, the pressure coefficient shows a clear trend with respect to the well width: it increases from 1.6 meV/GPa in the widest wells (3.8 nm) to 10.3 meV/GPa in the 3.1 nm wells, and to 18.9 meV/GPa in the narrowest wells (2.5 nm) in the experiment with low excitation intensity. Increase of the excitation intensity results in an increase of the pressure coefficients. The most noticeable change appears in the widest wells, where the pressure coefficient increases from 1.6 meV/GPa to 10.7 meV/GPa.

The quantum well PL decay time also significantly changes with applied pressure. The decay time constants of PL in 2.5 and 3.1 nm well samples measured at different pressures are shown by the open symbols in Fig. 4.3. The decay time constant increases from 11 to 37 ns in the 2.5 nm well and from 42 to 155 ns in the 3.1 nm wells when the pressure is increased from 1 atm to ~ 10 GPa. Decay times in the 3.8 nm wells sample were too long to be accurately measured with our experimental apparatus. The decay times in the InGaN/GaN quantum wells samples shown in Fig. 4.3 are a measure of the radiative carrier lifetime, which dominates over the nonradiative lifetime, as can be assessed from the very small variation of the integrated PL intensity with pressure (Fig. 4.1).

The PL spectra obtained from the $In_{0.11}Ga_{0.89}N$ epilayer at 1 atm and at an applied pressure of 11 GPa are shown in Fig. 4.4. The lines are narrower than those of the $In_{0.15}Ga_{0.85}N$/GaN quantum well PL (Fig. 4.1). The line width gradually increases with pressure from ~ 51 meV to ~ 65 meV. Also, the integrated PL intensity shows a reduction trend of approximately 40 % with applied pressure.

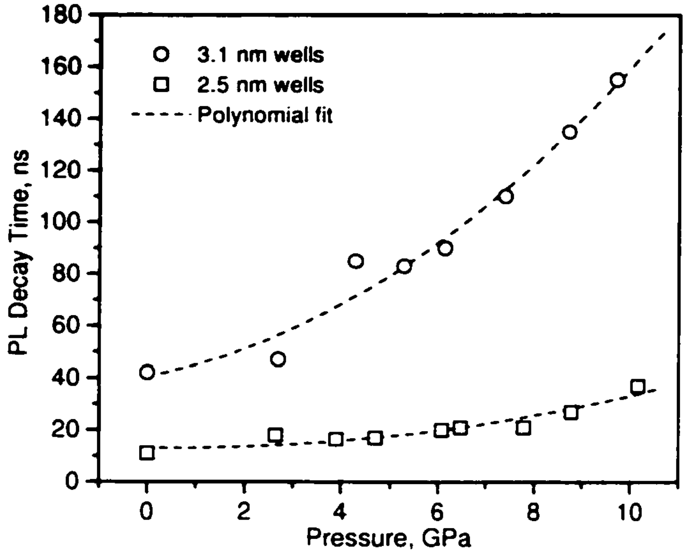

Fig. 4.3. Pressure dependence of the quantum well PL decay times in $In_{0.15}Ga_{0.85}N/GaN$ structures obtained with optical excitation intensity of 2 W/cm^2. Decay time constants are obtained with a least-square single exponential fit to the measured decay traces. Measurements were done at 35 K in the spectral interval within 20 meV from the PL peak. The dashed line is a guide to the eye.

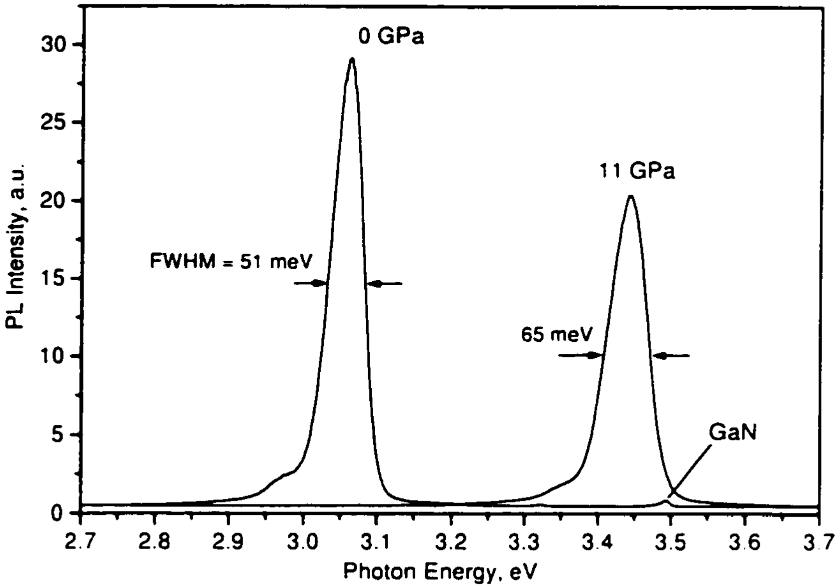

Fig. 4.4. Low temperature PL obtained from 80 nm $In_{0.11}Ga_{0.89}N$ epilayer at atmospheric pressure and at 11 GPa. The excitonic peak from the GaN buffer layer (~ 3.5 eV) is also shown.

The pressure shift of the PL peak energy and the change of the decay time constant in the epilayer are shown in Fig. 4.5. In contrast with the quantum well emission the PL from the epilayer has a rather large pressure coefficient of 37.4 meV/GPa, close to that of the GaN. Also, the PL decays are significantly faster in the epilayer than in the quantum wells and instead of increasing show a slight reduction with applied pressure.

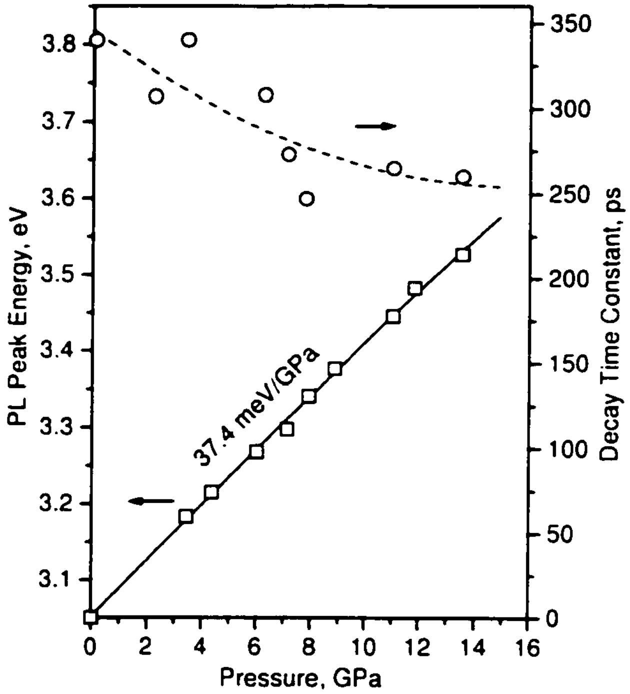

Fig. 4.5. Pressure dependence of PL peak energy and decay time constant in the 80 nm $In_{0.11}Ga_{0.89}N$ epilayer. The solid line is the second order polynomial fit to the data points; the dashed line is a guide to the eye.

4.2. Pressure measurements in GaN/AlGaN quantum wells

Figure 4.6 shows the typical PL spectrum in a $GaN/Al_{0.50}Ga_{0.50}N$ quantum well structure. Four emission peaks that correspond to the PL from the 1.8, 2.9, 3.9, and 4.9

nm wells respectively can be distinguished. The PL peak energies of the latter three wells are significantly lower that that of GaN (~ 3.5 eV), which is the material of the quantum wells.

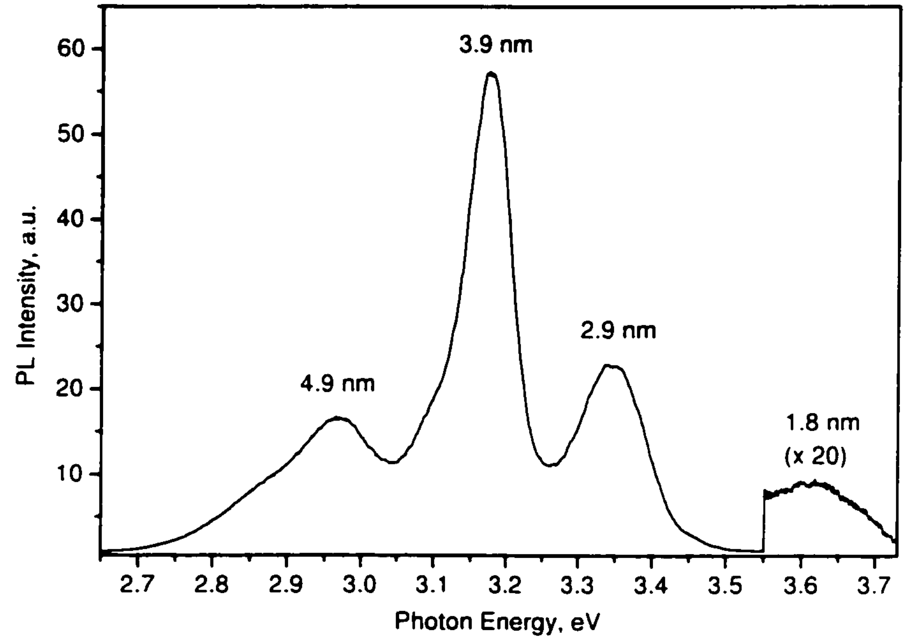

Fig. 4.6. Low temperature (T = 35 K) PL spectrum obtained from GaN/$Al_{0.50}Ga_{0.50}N$ quantum well structure at atmospheric pressure. PL peaks are labeled with the corresponding well widths. PL was obtained with optical excitation intensity of ~ 20 W/cm^2.

The pressure dependence of the quantum well PL in GaN/AlGaN structures with different AlN mole fractions in the barriers are shown in Fig. 4.7. As in the case of the InGaN/GaN samples the pressure coefficients of the quantum well PL emission are smaller than that of GaN and they reduce with the increase of the well width. In the sample with AlN mole fraction of 0.80 the pressure coefficient reduces from 16.1 meV/GPa in the 1.8 nm well to a record low – 7.2 meV/GPa in the 4.9 nm well. In

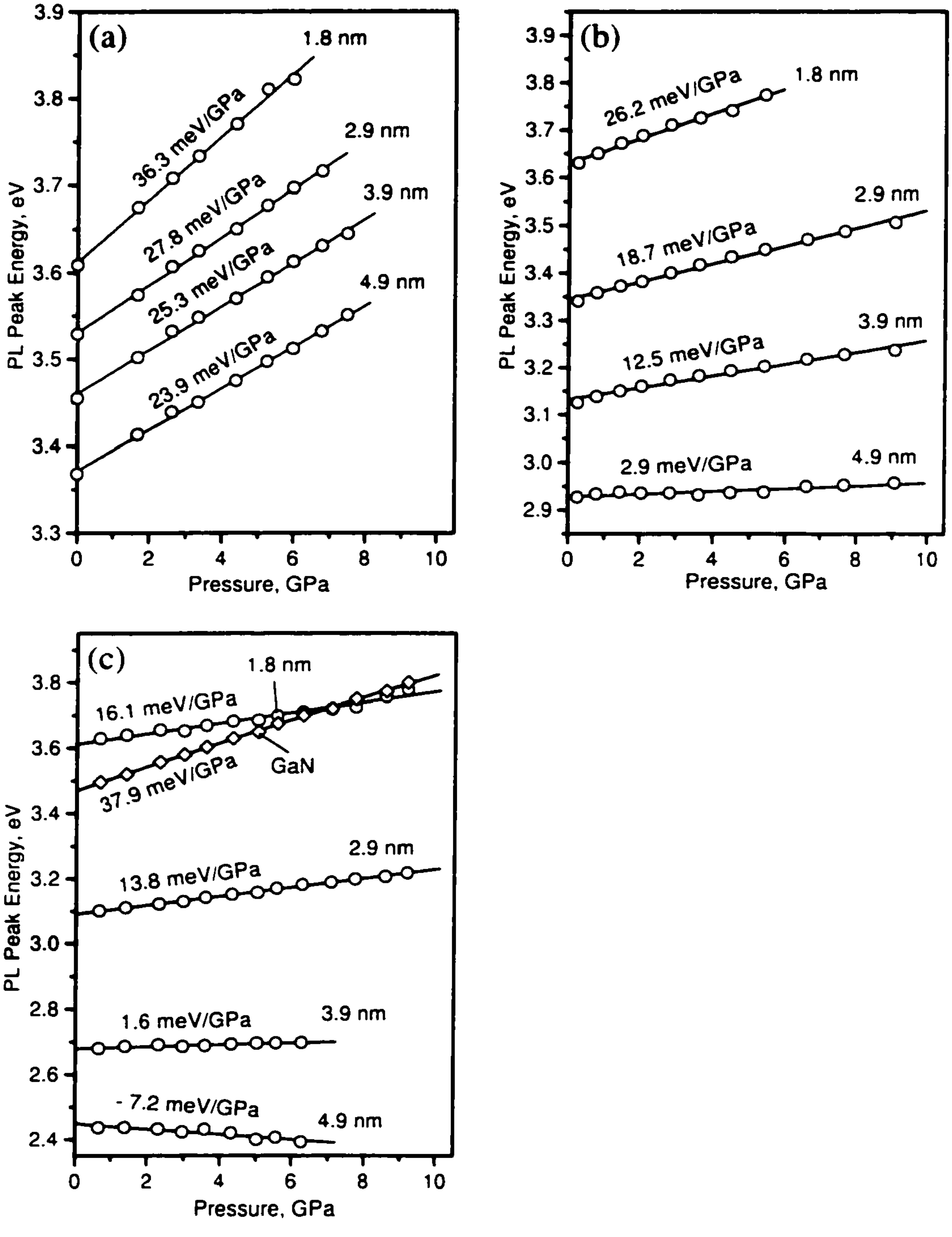

Fig. 4.7. Pressure dependence of the PL peaks in GaN/Al$_x$Ga$_{1-x}$N quantum well structures with $x = 0.2$ (a), $x = 0.5$ (b), and $x = 0.8$ (c). PL was obtained with optical excitation intensity of 2 W/cm^2 at 35 K. The pressure coefficients are shown above the lines.

addition, the pressure coefficients reduce with increase in the AlN mole fraction in the barriers. In the 3.9 nm well the pressure coefficient reduces from 25.3 meV/GPa in sample with $x = 0.20$, to 12.5 meV/GPa in the sample with $x = 0.50$, to 1.6 meV/GPa in the sample with $x = 0.80$ (Fig. 4.7).

The quantum well PL decay time measured in the GaN/AlGaN structures also shows a pressure behavior similar to that observed in the InGaN/GaN samples. The pressure dependence of the decay times in 2.9 and 3.9 nm wide quantum wells of the $x = 0.50$ sample is shown in Fig. 4.8. The wider well has the decay times significantly longer than the narrower one. Both decays increase with applied pressure: from 10 to 27 ns in the 2.9 nm well, and from 59 to 141 ns in the 3.9 nm. Unlike the case of the

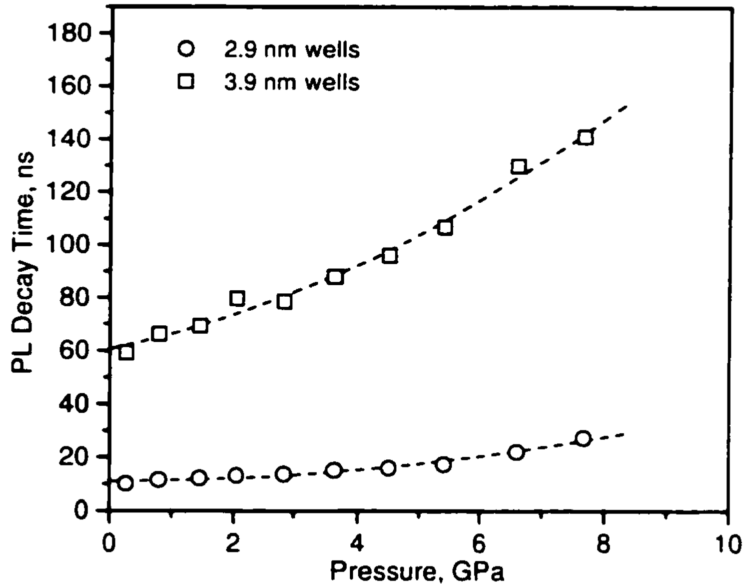

Fig. 4.8. Pressure dependence of the quantum well PL decay times in GaN/$Al_{0.5}Ga_{0.5}N$ structure obtained with optical excitation intensity of 2 W/cm^2. Measurements were done at 35 K in the spectral interval within 20 meV from the PL peak. The dashed line is a guide to the eye.

InGaN/GaN structures, the integrated PL intensity in GaN/AlGaN samples significantly reduces with applied pressure. The decay times measured in this experiment therefore may have contributions of both the radiative and nonradiative components.

5. Interpretation and analysis of experimental results

In Chapter 2 we have described some of the previous pressure studies in InGaN/GaN quantum wells and the interpretations of the unusual pressure behavior in these structures. Compared to these studies our work has incorporated new features that allowed us for the first time to identify unequivocally the major mechanisms responsible for this behavior. These new features include measuring the PL decay time as a function of pressure and performing experiments on the samples with varying well width L_w. In a recombination process dominated by the radiative component, the PL decay time has a direct dependence on the built-in electric field in the quantum wells (Eq. (2.21)). Therefore by tracking the change in the decay time with pressure we can evaluate the behavior of the electric field. In the experimental data presented in the previous chapter the quantum well PL decay time shows a dramatic increase with pressure. This finding suggests that the built-in electric field significantly increases with pressure.

The well width dependence of the PL peak energy also contains information about the magnitude of the built-in electric field. Since the field-induced red shift of the PL emission is proportional to L_w the change of the slope of the well width dependence of the PL peak energy can be used to assess quantitatively the changes in F_w. The strong well width dependence of the pressure coefficients of PL peak energies described in Chapter 4 thus also suggests a significant increase of the built-in electric field with pressure.

As it will be shown in this chapter the increase of the built-in electric field with applied pressure in the InGaN/GaN quantum wells contradicts the conventional theory of the electric polarization in nitrides, which predicts a slight reduction of the field with pressure. This point created one of the main barriers in understanding the pressure behavior in nitrides as being dominated by the polarization induced fields [120, 125]. To overcome this barrier we had to introduce in our analysis strong nonlinearities in the electromechanical properties of nitrides, which is a fairly unexplored subject for these materials.

In this chapter we systematically analyze the experimental findings reported in Chapter 4. The main focus of this analysis is on showing that the polarization induced electric field plays the major role in shaping the observed pressure behavior in the nitride heterostructures. We also show that the nonlinear piezoelectric effect is mainly responsible for the increase of the built-in electric fields with pressure, while the other secondary effects provide only a minor contribution to the observed effects in the pressure dependence of photoluminescence.

5.1. Pressure dependent PL in InGaN/GaN quantum wells and InGaN epilayer

As a first step in our analysis of the pressure dependence of the PL in InGaN/GaN quantum wells and InGaN epilayer we provide a qualitative interpretation of the observed effects. The pressure dependence of the quantum well PL peak energies at low excitation intensity (Fig. 4.2(a)) is dominated by the two competing effects: the bandgap increase in the well and barrier materials due to the reduction of the inter-atomic spacing, and the reduction of bandgap in the wells due to the quantum-confined Stark and Franz-Keldysh effects resulting from the increasing with pressure built-in electric field. The shift in the emission peak energy produced by the latter effect is approximately described by qF_wL_w, where q is the electron charge. The field-induced red shift of the emission is therefore larger in the wider wells than in the narrow ones. This is why the pressure coefficients in all measured samples increase with a reduction of the well width (Figs. 4.2, 4.7).

When we increase the optical excitation intensity in the samples we thus increase the concentration of photogenerated electrons and holes in the wells. The charge of these carriers partially screens out the built-in electric field, which results in the reduction of the field induced red shift of the emission peak and hence in an increase of the pressure coefficients (Fig. 4.2(b)).

In contrast to the quantum wells the 80 nm InGaN epilayer has the built-in electric field pinned at the value of $E_g/d \approx 0.39$ MV/cm by the self-screening effect [11]. This effect and the additional field screening by the charge of the photogenerated carriers assure that the built-in electric field does not play significant role in the epilayer. This is why the pressure coefficient of PL in the epilayer of 37.4 meV/GPa is much larger than those in the quantum wells (Fig. 4.5).

The quantum well PL decay time increase with pressure is also explained by the increase of the built-in electric field. We will show later that in the absence of the field the radiative lifetime in the quantum wells is not expected to change significantly with pressure. This is confirmed experimentally by the observed slight reduction of the decay time in the InGaN epilayer (Fig. 4.5) where the electric field is not important. The increase of the decay time observed in the quantum wells is therefore exclusively due to the spatial separation of the electrons and holes in the quantum wells leading to a reduced overlap of their wavefunctions.

To support this qualitative explanation of the pressure behaviour of the PL peak energy and decay time we calculate the PL peak energy shift with pressure in the absence of the effect of built-in field, and then obtain the magnitudes of the field and polarization from the experimental data of the Chapter 4. The first step in this analysis is determination of the strain in the quantum wells and in the barriers.

5.1.1. Calculation of strain varied by pressure

To find the strain in the InGaN quantum wells we add to the lattice mismatch strain a strain generated by the applied pressure. In these calculations we assume that the lattice mismatch between the GaN buffer and the sapphire substrate is accommodated by the low temperature grown nucleation layer, and therefore the buffer is essentially strain free before we apply pressure [126, 127]. Also, since the GaN buffer layer is much thicker than the quantum well layers we assume that most of the lattice mismatch between the GaN and InGaN is accommodated by the latter. With these assumptions the in-plane elastic strain in the wells is:

$$\varepsilon_1^{mism} = \varepsilon_2^{mism} = (a_{GaN} - a_{InGaN})/a_{InGaN} , \tag{5.1}$$

where a_{GaN} = 3.189 Å and a_{InGaN} = 3.241 Å are the lattice constants of free-standing GaN and InGaN films.

The sapphire substrate is the thickest element of the whole structure. Therefore the in-plane deformation of the samples with applied pressure is controlled by this element, resulting in equal pressure induced strains in the substrate, GaN, and InGaN layers [126]. To calculate these strains we assume a quasi-hexagonal symmetry of the substrate. This assumption can be justified since the elastic stiffness coefficient of sapphire C_{14} = - 23 GPa is almost an order of magnitude smaller than the other elements of the stiffness tensor of this material [49]. Applying Hooke's law (Eq. (2.2)) the pressure generated in-plane strain can be found as:

$$\varepsilon_1^p = \varepsilon_2^p = \frac{C_{13}-C_{33}}{(C_{11}+C_{12})C_{33}-2C_{13}^2}\,p, \qquad (5.2)$$

where C_{ij} are the elastic stiffness coefficients of sapphire [49], and p is the applied pressure in GPa. The total in-plane strain in the wells $\varepsilon_{1,2}^w$ and in the barriers $\varepsilon_{1,2}^b$ is given by:

$$\varepsilon_1^w = \varepsilon_2^w = \varepsilon_1^{mism} + \varepsilon_1^p;\ \ \varepsilon_1^b = \varepsilon_2^b = \varepsilon_1^p. \qquad (5.3)$$

The strain in the growth direction in the barriers ε_3^b and in the wells ε_3^w can be found from Hooke's law considering continuity of stress $\sigma = -p$:

$$\varepsilon_3^b = \frac{-p-2C_{13}^{GaN}\varepsilon_1^p}{C_{33}^{GaN}}; \qquad (5.4)$$

$$\varepsilon_3^w = -2\frac{C_{13}^{InGaN}}{C_{33}^{InGaN}}\varepsilon_1^{mism} + \frac{-p-2C_{13}^{InGaN}\varepsilon_1^p}{C_{33}^{InGaN}} = \varepsilon_3^{mism} + \varepsilon_3^p. \qquad (5.5)$$

The terms proportional to C_{13}/C_{33} in Eqs. (5.4) and (5.5) account for the Poisson effect induced by the in-plane strain. The InGaN elastic stiffness coefficients were obtained from the values for GaN and InN given in Table 2.1 using linear interpolation.

Figure 5.1 shows the results of strain calculation with pressure for the InGaN quantum wells. The applied pressure significantly modifies the strain state with

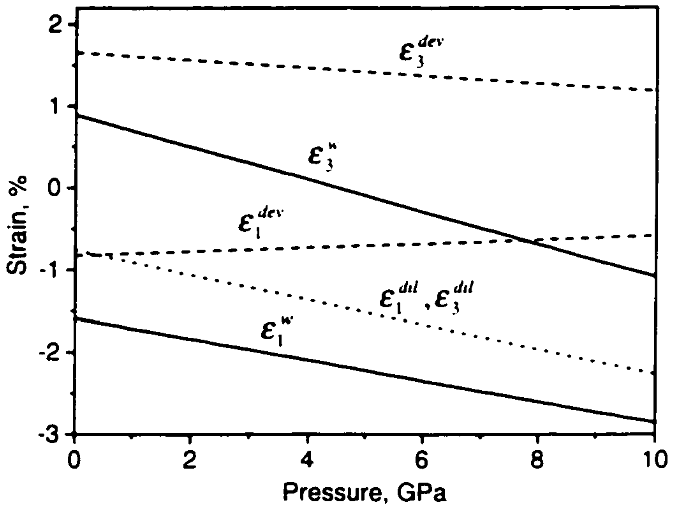

Fig. 5.1. Pressure dependence of the strain components in $In_{0.15}Ga_{0.85}N/GaN$ quantum wells.

respect to the initial strain generated by the lattice mismatch. The in-plane strain increases from –1.59 % at atmospheric pressure to –2.86 % at 10 GPa. The strain in the growth direction, which is 0.89 % at atmospheric pressure, changes its sign at ~ 4.5 GPa and arrives at – 1.09 % at 10 GPa. Also shown in the Fig. 5.1 are the calculated with Eqs. (2.30) and (2.31) deviatoric and dilatational components of strain that will be used in the calculation of pressure dependence of the piezoelectric constants.

5.1.2. Bandgap energy variation with pressure

From the calculated changes of strain with pressure we can obtain the pressure variation of the $In_{0.15}Ga_{0.85}N$ bandgap energy as [34]:

$$\Delta E_g^{InGaN}(p) = 2\varepsilon_1^p(a_c^{\parallel} - D_2 - D_4) + \varepsilon_3^p(a_c^{\perp} - D_1 - D_3) = 0.0387p\,. \text{ [eV]} \quad (5.6)$$

where the deformation potentials for InGaN $a_c^{\parallel} - D_2 = -9.18\,\mathrm{eV}$, $D_3 = 5.63\,\mathrm{eV}$, $a_c^{\perp} - D_1 = -5.80\,\mathrm{eV}$, and $D_4 = -2.85\,\mathrm{eV}$ were determined by linear interpolation between the theoretical values of the deformation potentials of GaN and InN shown in Table 2.1. Including the effects of the pressure dependence of the electron effective mass [117] and band offsets in the InGaN wells the bandgap shift with pressure is found to be *dE/dp* = 38.2 meV/GPa. This value expected in the polarization-free quantum wells of all thicknesses is confirmed by the close value of *dE/dp* = 37.4 meV/GPa measured in the $In_{0.11}Ga_{0.89}N$ epilayer (Fig. 4.5). We therefore can conclude that the small and well width dependent pressure coefficients of InGaN quantum well PL can not be explained by the effect of pressure on the band structure. This supports our explanation of the observed pressure behavior of PL as being dominated by the increasing with pressure electric field.

5.1.3. Determination of the built-in field and polarization

Next step in our analysis is the determination of the magnitude of the built-in electric field and electrical polarization at different pressures. The strongest transition responsible for the PL emission in quantum wells is the transition between the first confined state of electron e_1 and that of the heavy hole hh_1. In the presence of a transverse electric field F_w the energy of this transition can be approximated as [82]:

$$E_{e_1\text{-}hh_1} = E_g + E_{e_1} + E_{hh_1} - qF_w L_w, \qquad (5.7)$$

where E_g is the bandgap of the quantum well material (InGaN), and E_{e_1} and E_{hh_1} are the electron and hole confinement energies. It follows from this expression that if the wells are sufficiently wide and the magnitude of the electric field is sufficiently large, F_w almost exclusively defines the slope of the well width dependence of the PL peak energy in the quantum wells [82, 128]. This is the case in our InGaN/GaN samples as shown in Fig. 5.2, where the linear fit to the atmospheric pressure PL peaks (solid line) is compared with that of the calculation of the e_1-hh_1 transition performed using technique

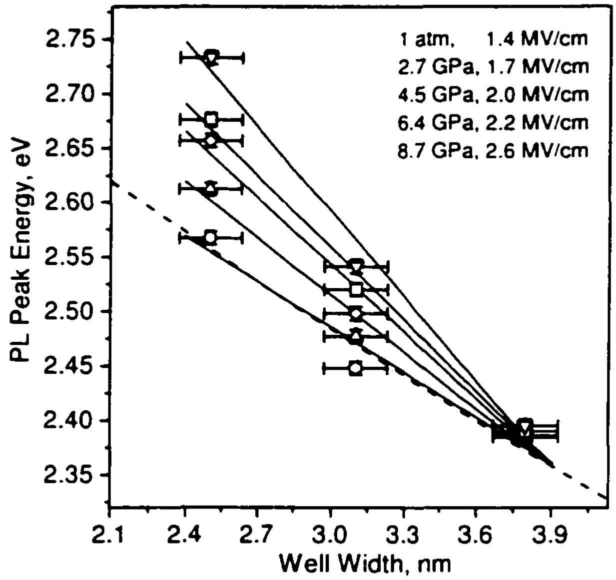

Fig. 5.2. PL peak energy in InGaN/GaN quantum wells as a function of well width at different applied pressure. The solid lines are linear fits to the PL peak energies. The resulting values of the built-in electric fields are shown in the upper right corner. The dashed line is the best fit to the atmospheric pressure data obtained by calculating e_1-hh_1 transition energy with the built-in field and energy offset as adjustable parameters.

developed by Miller *et al.* [129] (dashed line). The details of the calculation are given in the Appendix 2. Both fits provide the same value of the built-in electric field of 1.4 MV/cm, thus indicating that F_w at each pressure can be found simply from the slopes of the PL peak energy/well width dependence [82]. The values of the electric field obtained with this approach are shown in Fig. 5.3. F_w increases from 1.4 to 2.6 MV/cm when the pressure is increased from 1 atm to 9 GPa.

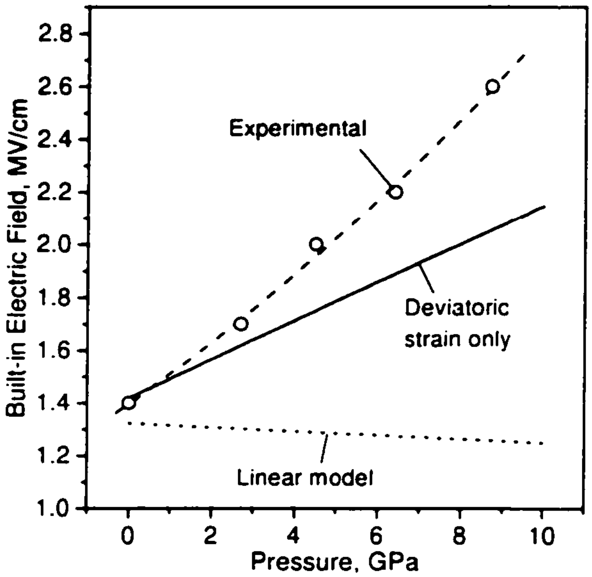

Fig. 5.3. Experimental and theoretical pressure dependence of the built-in electric field in $In_{0.15}Ga_{0.85}N/GaN$ quantum wells.

Next we compare the values of F_w obtained from the experiment with those predicted by the conventional model of polarization. For a structure with four equal wells located sufficiently far from the sample surface the assumptions for Eq. (2.14) hold, and F_w can be calculated from Eq. (2.15):

$$F_w = (P_b - P_w)/(\epsilon_w + \epsilon_b L_w/L_b), \tag{5.8}$$

where $\epsilon_{w,b}$ are the permittivities of the InGaN well and GaN barrier. $L_{w,b}$ are the well and barrier width, and $P_{b,w}$ are the total polarizations in the barriers and in the wells. The piezoelectric polarization components in the wells and in the barriers are found using Eq. (2.10):

$$P_w^{pz} = e_{33}^w \varepsilon_3^w + 2e_{31}^w \varepsilon_1^w, \tag{5.9}$$

$$P_b^{pz} = e_{33}^b \varepsilon_3^b + 2e_{31}^b \varepsilon_1^b. \tag{5.10}$$

The piezoelectric coefficients and the values of spontaneous polarization for InN and GaN are taken from Ref. 58 (Table 2.3); the values for InGaN are found using linear interpolation. The permittivities of GaN and InGaN (Table 2.1) are assumed to be independent of pressure.

The dotted line in Fig. 5.3 shows the results of calculations performed with the conventional linear model. Instead of increase, this model predicts a slight reduction of the built-in field with pressure. This obvious contradiction between the linear model and experiment suggests the strong contribution of the secondary effects, such as nonlinear piezoelectricity, to the polarization response of our samples. To show the feasibility of this explanation we estimate the change of F_w considering the deviatoric strain dependence of the piezoelectric coefficients of GaN calculated by Shimada *et al.* [25] and shown in Fig. 2.12. Since the volume conserving strain dependence of the piezoelectric coefficients in InGaN is not available, we use for this material the strain dependence of GaN. The built-in field is then calculated in the same way as for the linear model, using Eqs. (5.8) – (5.10). The solid line in Fig. 5.3 shows the result of this calculation. In this case the built-in field significantly increases with applied pressure, the slope of this increase being somewhat smaller than that determined from the experiment. This confirms that nonlinear piezoelectricity can be responsible, at least in part, for the observed anomaly in the pressure behavior of the InGaN/GaN quantum wells. The underestimation of the calculated dependence can be attributed to the contribution of the dilatational strain to the change in the piezoelectric coefficients not considered here, to the different strain dependence of the piezoelectric coefficients in InGaN than in GaN, and to the other secondary effects, such as nonlinear elasticity and photoelastic effect.

5.1.4. Pressure dependence of PL decay time

After establishing the reason for the small and well width dependent pressure coefficients of quantum well PL peaks we can focus on the analysis of the pressure dependence of the PL decays. We begin with a simple case of the band-to-band radiative recombination process in the absence of electric field and localization effects. The recombination rate for this process is given by [130]:

$$B = \frac{q^2}{m_0^2 c^3 \hbar^2}\left[\frac{2\pi\hbar^2}{k_B T}\right]^{3/2} \frac{\sqrt{\epsilon}\, M^2}{(\bar{m}_x \bar{m}_y \bar{m}_z)^{1/2}} E_g \left[1+\frac{3k_B T}{2E_g}\right], \tag{5.11}$$

where M is the matrix element, $\bar{m}_x = m_e + m_{h,x}$, $\bar{m}_y = m_e + m_{h,y}$, and $\bar{m}_z = m_e + m_{h,z}$. In Eq. (5.11) E_g, m_e, and ϵ are the parameters that have the strongest dependence on pressure [124]. The pressure dependence of m_e can be related to the band gap variation with pressure using [131]:

$$\frac{m_0}{m_e} = 1 + \frac{6M^2\left(E_g(p) + \frac{2}{3}\Delta_0\right)}{m_0 E_g(p)\left(E_g(p) + \Delta_0\right)}, \tag{5.12}$$

where Δ_0 is the spin-orbit splitting. Both the M and Δ_0 are fairly insensitive to the applied pressure [124]. The pressure dependence of the static dielectric constant ϵ in InGaN is taken from Ref. [86]. Using the experimentally obtained band gap pressure dependence for InGaN we calculate the variation of the normalized recombination rate $B(p)/B(0)$ with pressure from Eq. (5.11). Since the radiative carrier lifetime is inversely proportional to B we can also obtain the variation of the normalized carrier lifetime with pressure, which is shown in Fig. 5.4. by the dashed line. According to these calculations the radiative lifetime should slowly reduce with pressure. This finding is supported by the decay time trend observed in the InGaN epilayer (Fig. 4.5). The similar trend was also observed by Mariette *et al.* in the pressure behavior of decay time of bound excitons in GaAs [132]. For the free carriers or excitons confined in quantum wells or quantum dot-like formations we expect the same trend, since the pressure dependencies of the carrier dynamics are also dominated by the same terms [124]. We conclude that the significant increase of the PL decay time with pressure observed in our experiments is the result of increasing F_w.

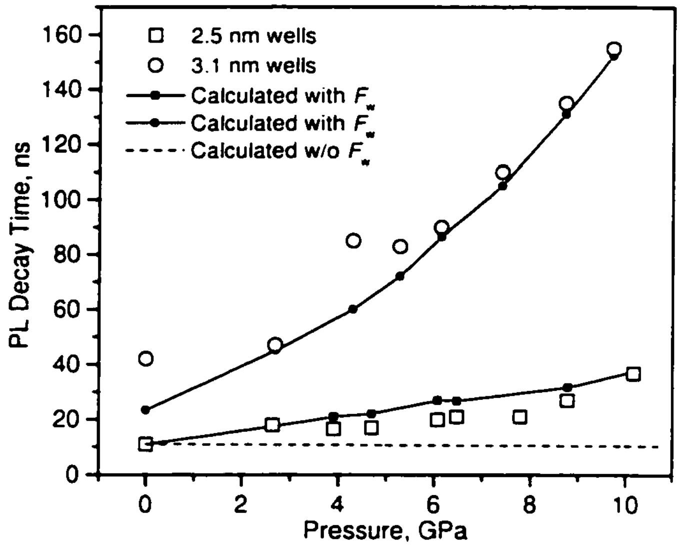

Fig. 5.4. Pressure dependence of the PL decay time constant in 2.5 and 3.1 nm quantum wells.

The change in the radiative carrier lifetime in the quantum wells with applied pressure can be calculated using the values of F_w determined from the experiment (Fig. 5.3). Using the approach described by Miller *et al.* [129] we calculate the wavefunctions of the e_1 electron and hh_1 hole at different pressures and F_w (Appendix 2). Figure 5.5 shows the calculated electron and hole wavefunctions (squared) at atmospheric pressure and at 9 GPa. From the calculated wavefunctions we find the change in the radiative carrier lifetime as:

$$\tau(p) = \frac{A}{\left(\int_{-\infty}^{\infty} dz \psi_e(z) \psi_h(z) \right)^2}, \qquad (5.13)$$

where A is a normalization parameter, and $\psi_e(z)$ and $\psi_h(z)$ are the electron and heavy hole wavefunctions. The normalized carrier lifetime in the 2.5 and 3.1 nm wells is shown

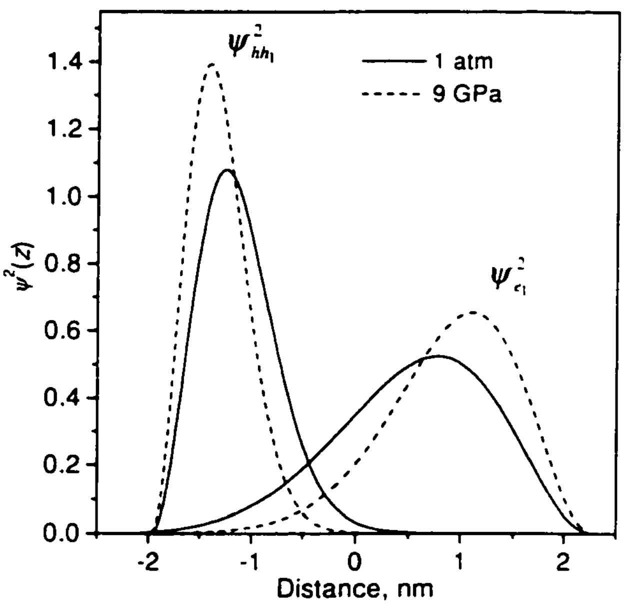

Fig. 5.5. Ground state electron and hole wavefunctions squared calculated for atmospheric pressure and for 9 GPa in a 3.1 nm InGaN/GaN quantum well.

in Fig. 5.4 by the solid line. The normalization parameter A is chosen to match the calculated lifetime in the 2.5 nm wells with the experimental decay time of 11 ns. The same value of A is used for both wells. The calculated lifetime reproduces well the measured decays for the wells of each width. This excellent agreement confirms the values of the built-in electric field determined from the experimental PL data in section 5.1.3.

5.2. Pressure dependent PL in GaN/AlGaN quantum wells

Obtaining an accurate description of the built-in electric field and electric polarization in InGaN/GaN quantum wells is somewhat complicated by the uncertainty of the InGaN bandgap energy and its pressure dependence [30, 42, 86]. This complication arises from the not so well established physical properties of InN and from the possible effects of the deformation potentials bowing and carrier localization on the pressure behavior of PL [125]. In contrast, in the GaN/AlGaN quantum well system properties of both GaN and AlN are determined with good precision and the effects of localization and deformation potentials bowing are not expected to play important role. Therefore in the analysis of the experimental results in this system we can use a more direct approach.

To obtain the values of the built-in electric field in the GaN/AlGaN quantum wells we fit the PL data with the model that describes the $e_1 - hh_1$ transition energy in the wells with the expression of the following form:

$$E_{e_1\text{-}hh_1} = E_{GaN} + E_{e_1} + E_{hh_1} - E_{ex}, \qquad (5.14)$$

where E_{GaN} is the GaN bandgap energy at each applied pressure, E_{e_1} and E_{hh_1} are the confinement energies, and E_{ex} is the exciton binding energy. The last three terms in Eq. (5.14) introduce the built-in electric field dependence of the e_1 – hh_1 transition energy. We thus intend to determine the values of electric field by using it as the only adjustable parameter in the fitting procedure.

As in the case of the InGaN/GaN wells we first calculate the strain state in the wells and in the barriers of the GaN/AlGaN structures. The procedure of these calculations is very similar to the one described above in the Section 5.1.1. The results of the strain calculations for the structure with AlN mole fraction in the barriers of 0.5 are shown in Fig. 5.6. Using these results and the theoretical values of the deformation potentials for GaN and AlN we estimate the pressure shift of the bandgap energies in GaN and AlGaN. The bandgap pressure coefficients found here are shown for different materials in the Table 5.1.

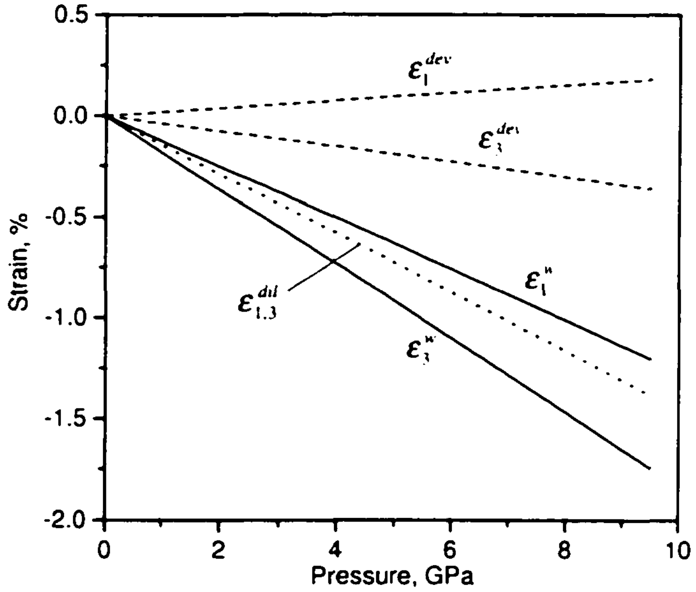

Fig. 5.6. Calculated pressure dependence of the strain components in GaN quantum wells of GaN/AlGaN structures.

Table 5.1. Calculated pressure coefficients of the bandgap energy in GaN and AlGaN with different AlN mole fraction.

Material	dE_g/dp, (meV/Gpa)
GaN	38.5
$Al_{0.20}Ga_{0.80}N$	39.5
$Al_{0.50}Ga_{0.50}N$	41.1
$Al_{0.80}Ga_{0.20}N$	42.6

Once the bandgap energies are defined we can find the electron and heavy hole confinement energies at different applied pressures and as a function of built-in electric field. These calculations are made following the technique developed by Miller *et al.* [129]. This completes determination of the first three terms in Eq. (5.14).

5.2.1. Calculation of the exciton binding energy

Next we calculate the exciton binding energy in the quantum wells as a function of well width and built-in electric field. Unlike the case of InGaN quantum wells investigated in this work, the GaN/AlGaN structures have wells with significant variation of width (from 1.8 nm to 4.9 nm). When the well width changes that much we cannot assume the exciton binding energies to be the same for all wells. Therefore an accurate calculation of this parameter is required to model the PL peak energies.

The binding energies were calculated using an approach described by Leavitt and Little [133]. Figure 5.7 shows the exciton binding energies calculated as a function of the well width (Appendix 3). The theoretical values of the built-in electric field in the wells at atmospheric pressure were used in these calculations. The well width dependencies shown in Fig. 5.7 were fitted with Gaussian functions and introduced in the model in analytical form.

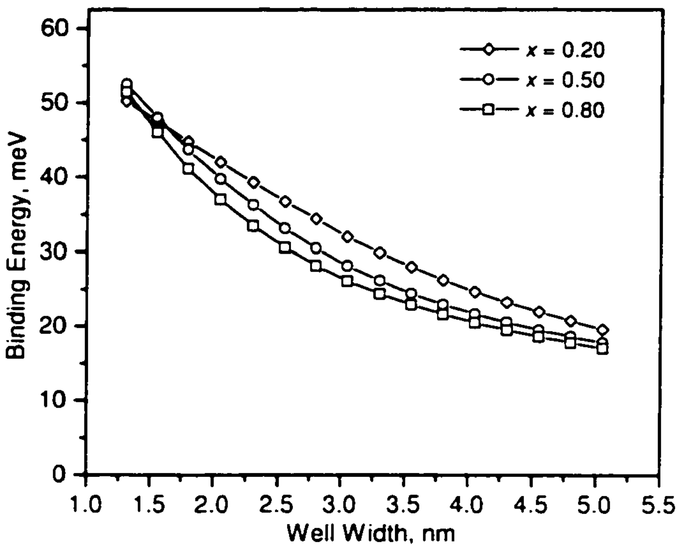

Fig. 5.7. Exciton binding energy as a function of the well width calculated using the theoretical values of the built-in electric field at atmospheric pressure.

5.2.2. Built-in electric field and well-barrier polarization difference

Among the several differences between the InGaN/GaN and GaN/AlGaN samples investigated in this work is the significant difference in their geometry. The latter group of samples has quantum wells located very close to the sample surface. The wells are therefore in the range of the surface potential-induced band bending [134, 135]. This band bending not only affects the built-in field in the wells, but also introduces a difference in the electric field between the wells at different distances from the surface. A schematic band diagram of the GaN/AlGaN quantum well structure that incorporates the effect of the surface proximity is shown in Fig. 5.8. Considering this effect the built-in

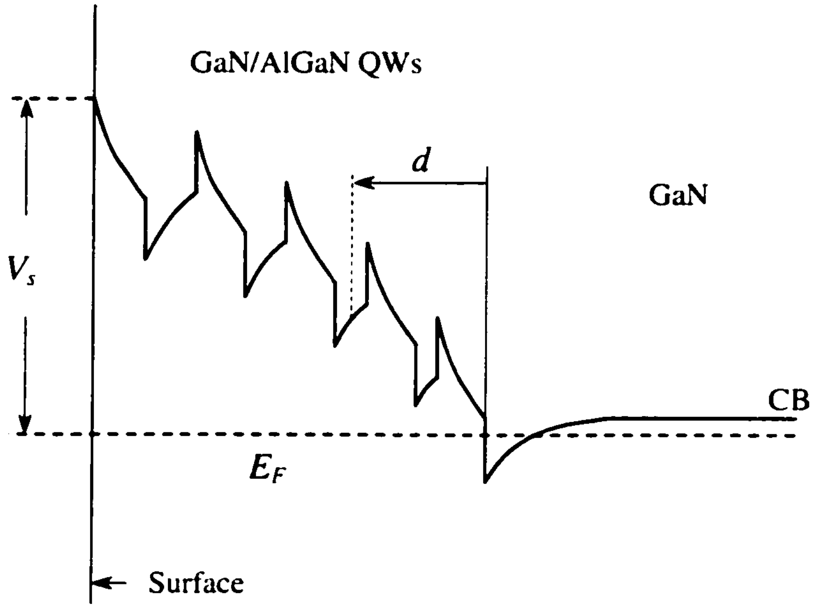

Fig. 5.8. Schematic diagram of the conduction band edge in the GaN/AlGaN quantum well region. After Simon *et al.* [134].

electric field in the wells is defined by the following expression [134]:

$$F_w = \frac{-(P_w - P_b) + \rho}{\epsilon\,(1 + L_w / L_b)} + \frac{V_s}{L_b + L_w} - \frac{qN_D}{\epsilon}\left[d - \frac{L_b + L_w}{2}\right], \qquad (5.15)$$

where ϵ is the permittivity of the GaN wells and $Al_xGa_{1-x}N$ barriers (assumed to be independent of pressure in this work), $L_{w,b}$ are the cumulative thicknesses of the well and the barrier layers, ρ is the 2D photogenerated charge density in the wells, V_s is the surface barrier potential assumed to be $V_s = 0.7 + 2.28x$ (eV) [134], $N_D \approx 10^{17}$ cm^{-3} is the background doping concentration, and d is the distance from the barrier-buffer interface to the well where the field is calculated. The first term in the Eq. (5.15) introduces the contribution of the well-barrier polarization difference $P_w - P_b$ (corrected for the screening by the photogenerated charge carriers) to the built-in field. The second term introduces the band edge tilting produced by the surface potential. And the third term in the Eq. (5.15) brings into consideration the band bending due to the residual doping in the structure.

According to the Eq. (5.15) the built-in field varies with well position in the structure and with the amount of the photogenerated charge. It is therefore more convenient to use in our fitting procedure the polarization difference $P_w - P_b$ as the adjustable parameter instead of the field intensity. This is a more universal characteristic that depends only on the materials of the barriers and the quantum wells and on the applied pressure.

The concentration of photogenerated charge ρ is determined from the following considerations. First the 2D carrier concentration generated by the single excitation pulse is determined as:

$$n = \frac{I_{av}(1 - e^{-\alpha_w L_w}) + I_{av}(1 - e^{-\alpha_b L_b})}{f(\hbar\omega)SA}, \qquad (5.16)$$

where I_{av} is the average power of the optical excitation beam (~ 4 mW), α_w and α_b are the absorption coefficients of the GaN quantum well and AlGaN barrier at the excitation wavelength ($\alpha_b \approx 10^7$ m^{-1} at 265 nm for $x = 0.2$ and $x = 0.5$; $\alpha_b = 0$ for x = 0.8 [136]). $f =$ 82 MHz is the repetition rate of the optical pulses, $\hbar\omega$ is the photon energy, $S \approx 8\times10^{-11}$m^2

is the illuminated spot area, and $A = 1309$ is the total attenuation factor that includes the optical beam attenuation by the neutral density filter, mirror losses, reflection losses at the cryostat window, diamond, and sample surface, and attenuation by the diamond. The absorption coefficient in the quantum well is approximated as [137]:

$$\alpha_w = \alpha_{GaN} \frac{\pi\hbar}{L_w\sqrt{2\mu_r(\hbar\omega - E_{GaN})}} \left(\int_{-\infty}^{\infty} \psi_e(z)\psi_h(z)dz \right)^2 , \tag{5.17}$$

where α_{GaN} is the absorption coefficient of bulk GaN ($\alpha_{GaN} \approx 10^7$ m^{-1} at 265 nm [136]), μ_r is the reduced electron-hole effective mass, and E_{GaN} is the GaN bandgap energy. The electron and hole envelope functions were calculated using the approach described in Ref. 129 using the theoretical values of the built-in electric field.

Next, for the well where the carrier lifetime is longer than the period of the excitation pulses, we calculate the quasi-equilibrium 2D carrier concentration as:

$$N = n\sum_{m=0}^{\infty} e^{-mT/\tau} , \tag{5.18}$$

where m is an integer (pulse number), $T = 12.2$ ns is the pulse period, and τ is the carrier lifetime (measured decay time constant). The carrier lifetime in the wide quantum wells where the decay time was too long to be accurately measured with our experimental system was approximated from the values measured in the narrower wells.

Figure 5.9 shows the typical least square fits to the PL peaks obtained with the model described above for the PL measured at 5 GPa. The good agreement between the fit and the experimental data suggests that the model accurately describes the ground state energy in the quantum wells. To highlight the importance of the built-in electric field in shaping the well width dependence of the PL peak energy we calculated the e_1-hh_1 transitions in our samples for the field-free case. These calculations are shown by the dashed line. The comparison of these dependences with the experimental data clearly demonstrates the profound effect of the electric field on the observed PL peak energies.

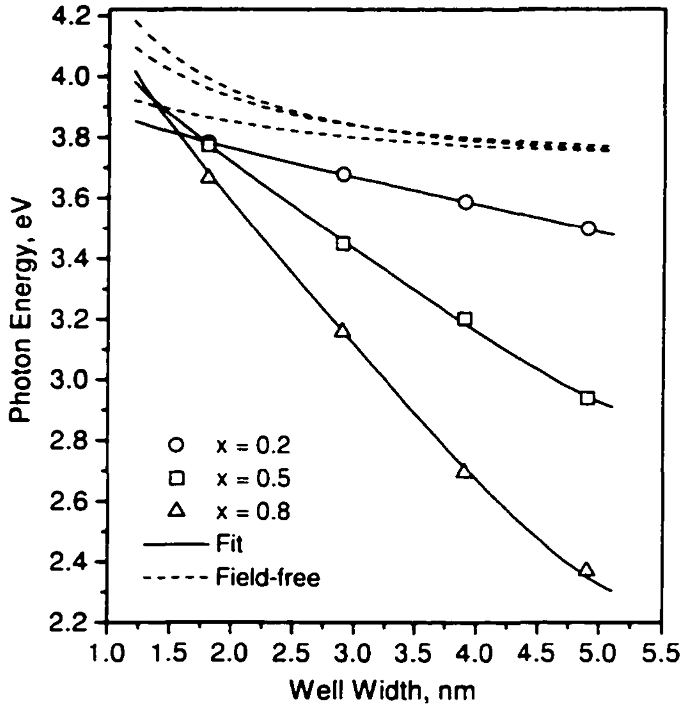

Fig. 5.9. Well width dependence of the PL peak energy in GaN/AlGaN quantum wells at 5 GPa. Open symbols are the experimental points; solid lines are the fits to the PL peaks obtained with the model described in the text. The dashed lines are the quantum well transition energies calculated in the absence of the built-in electric field.

As a result of the fitting procedure we obtain the well-barrier polarization difference. This parameter is shown as a function of the applied pressure for all three GaN/AlGaN samples in Fig. 5.10. The right-hand scale in these plots shows the corresponding built-in electric field in the 2.9 nm wells. As in the case of the InGaN/GaN quantum wells we find that the built-in field significantly increases with pressure, by

0.32, 0.76, and 1.01 MV/cm in the samples with x = 0.20, 0.50, and 0.80 respectively, in the pressure range of 8 GPa.

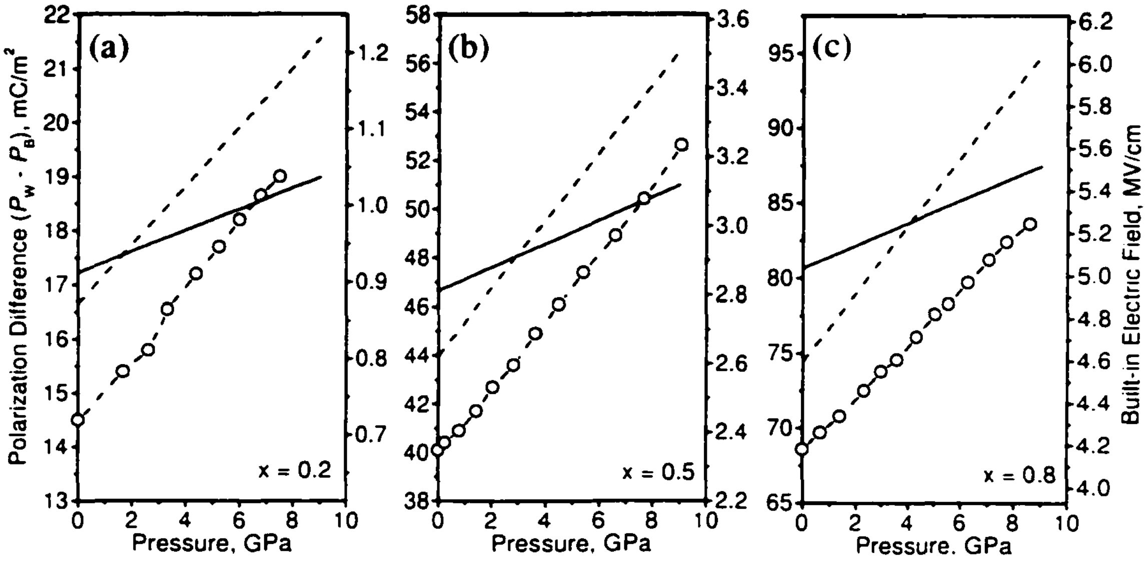

Fig. 5.10. Pressure dependence of P_w–P_b and corresponding built-in electric field in 2.9 nm GaN/AlGaN quantum wells with a) x = 0.2, b) x = 0.5, and c) x = 0.8. The experimental points shown by the circles were obtained from the fits to the PL data as shown in Fig. 5.9. The solid lines show the P_w–P_b and F_w calculated with the linear model. The dashed lines are the results of calculations with the strain dependence of piezoelectric coefficients suggested by Shimada *et al.* [25].

The calculated values of the polarization difference and the built-in field can be compared with those predicted by the conventional model of polarization. Spontaneous polarization difference is found using the values of the spontaneous polarization of GaN and AlN that are given in Table 2.3, and the linear interpolation between these values is used for the AlGaN. The piezoelectric polarizations in the wells and in the barriers at different pressures are found using Eqs. (5.9) and (5.10). The built-in electric field in the

2.9 nm wells is then found using Eq. (5.15). The results of this calculation are shown in Fig. 5.10 by the solid line. For every sample the conventional model predicts the slope of the pressure dependence of the polarization difference (and built-in filed) significantly smaller than that obtained from the experiment. We conclude that this model does not provide an adequate description of the polarization response to pressure in the GaN/AlGaN heterostructures.

Next we repeat the calculations introducing the nonlinear piezoelectric effect. We use the deviatoric strain dependence of the piezoelectric coefficients of GaN and AlN from the work of Shimada *et al.* [25], and the linear interpolation for the AlGaN. The results of this calculation are shown by the dashed line in Fig. 5.10. The slopes of the pressure dependences of the built-in field are much closer in this case to the experimental ones. This suggests that the nonlinear piezoelectricity is largely responsible for the observed pressure dependence of polarization and quantum well PL in GaN/AlGaN.

Although the effect of the nonlinear piezoelectricity in GaN/AlGaN system is not as dramatic as in the InGaN/GaN, the findings made in this section are very important. These findings were made under the minimum number of assumptions with direct calculation of the built-in fields and polarization differences from the PL data. Therefore the evidence of the nonlinear piezoelectric response in GaN/AlGaN suggests that strong nonlinearity is a universal property in group III nitrides. It also confirms the interpretation of the anomalous pressure behavior of PL in InGaN/GaN wells as being due to the nonlinear piezoelectricity.

5.2.3. The role of the other secondary effects

In the analysis provided in the previous section we did not take into account the role that the secondary effects other than nonlinear piezoelectricity may play in shaping the pressure dependence of PL. This is mostly related to the lack of the experimental and theoretical descriptions of these effects. In this section we use some of the available evidence to obtain a rough estimate of the possible contribution of the nonlinear elasticity and photoelastic effect to the pressure dependence of polarization difference. In Fig. 5.11 we recalculated the experimental and "linear" model values of P_w–P_b introducing the nonlinear elasticity and photoelastic effect, for the GaN/AlGaN quantum wells with x = 0.5. The nonlinear elasticity was taken into account by assuming pressure dependent elasticity coefficients C_{ij} of sapphire [138] and AlN [78]. The lack of reports on the

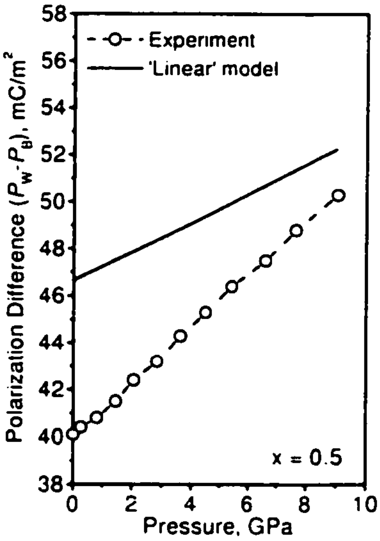

Fig. 5.11. Experimental and 'linear' model pressure dependence of P_w–P_b in the GaN/AlGaN quantum wells with x = 0.5 obtained considering pressure dependence of the elasticity coefficients C_{ij} of sapphire, AlN, and GaN, and that of the dielectric constants of AlN and GaN.

pressure dependence of C_{ij} led us to assume for GaN the same dependence as in AlN. The effect of lattice mismatch strain was neglected (we found that it does not significantly affect the slope of the pressure dependence). The pressure dependence of the electronic dielectric constants of GaN and AlN was taken from the Ref. [86]. As follows from these simple estimates the introduction of nonlinear elasticity and photoelastic effect, although producing tangible corrections to the polarization difference, does not have strong enough effect to explain the observed pressure response of polarization.

6. Impact of this work on recent studies in group III-nitrides

Following publication of the work that is being presented in this dissertation [139-143] a number of studies appeared in the literature that confirm the importance of the nonlinear polarization effects in group III-nitrides. In this chapter we review some of these works and compare, where possible, these new findings with the results obtained in our work.

Łepkowski *et al.* [144] investigated the pressure dependence of the PL in GaN/AlGaN quantum well structures with AlN mole fraction of 0.17 and with the well width ranging from 1.6 nm to 8.3 nm. The pressure coefficients of PL peak energies were found to reduce from 35.6 meV/GPa in the 1.6 nm well to 23.8 meV/GPa in the 8.3 nm well (Fig. 6.1). This effect was attributed to the increase of the built-in field with pressure. A linear model of polarization was used to describe the experimental observations (solid symbols in Fig. 6.2). One of the assumptions in the model was that the spontaneous polarization in AlN is – 0.036 C/m^2, almost by the factor of three smaller than theoretically calculated value of – 0.090 C/m^2 [58]. Authors concluded that the linear model of polarization provides reasonable description of the experimental observations. The same set of data, however, was reanalyzed in a later work by the same group of authors, now considering the nonlinear piezoelectric effect [145]. The results of this analysis are shown in Fig. 6.2. Much better agreement with the experiment was achieved in this case, which demonstrated the importance of the nonlinear piezoelectricity in the pressure behavior of PL in the investigated structures.

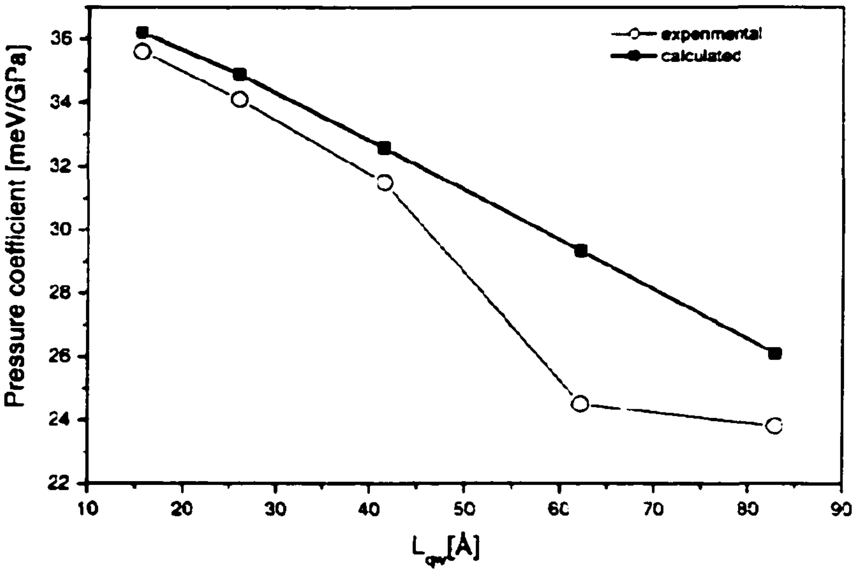

Fig. 6.1. Experimental and calculated pressure coefficients in $GaN/Al_{0.17}Ga_{0.83}N$ quantum wells. Calculations are based on the linear model of polarization. After Łepkowski *et al.* [144].

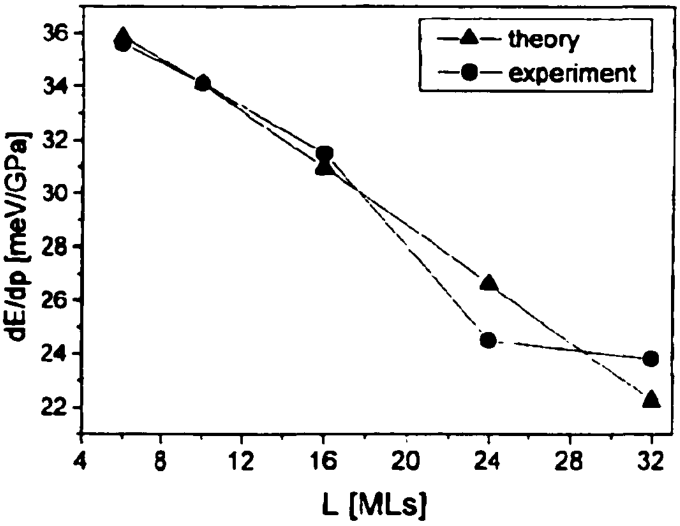

Fig. 6.2. Experimental and calculated pressure coefficients in $GaN/Al_{0.17}Ga_{0.83}N$ quantum wells. Calculations include nonlinear piezoelectricity. After Perlin *et al.* [145].

Suski *et al.* [146] compared the pressure dependence of PL in the wurtzite InGaN/GaN quantum wells with that in the structures with zinc blende lattice configuration, where the piezoelectric and spontaneous polarizations are absent due to the higher lattice symmetry. The authors of this work found that in the zinc blende InGaN/GaN the pressure coefficients of PL are of the order of 26 – 30 meV/GPa and are independent of the well width (Fig. 6.3). These findings support the conclusion of our work that the pressure behavior of PL in the wurtzite InGaN/GaN is dominated by the polarization induced built-in electric field. The smaller pressure coefficients in InGaN than in GaN and in wurtzite InGaN observed in this work can be attributed to the significantly smaller *dE/dp* in zinc blende InN (~19 meV/GPa [119]) than in the wurtzite InN (~ 33 meV/GPa [86]), and to the In segregation effect [146].

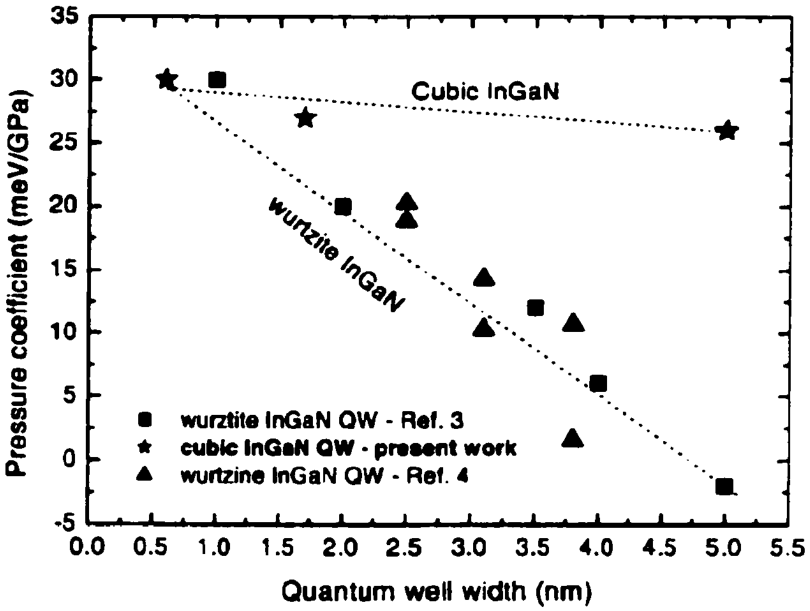

Fig. 6.3. Experimental pressure coefficients of PL peak energies in wurtzite and zinc blende InGaN/GaN quantum wells. Refs. 3 and 4 are the Refs. 125 and 141 respectively, in this dissertation. After Suski *et al.* [146].

Bernardini and Fiorentini investigated the effects of strain and composition on the macroscopic polarization in III-V nitride alloys in a theoretical work [147]. This work was later significantly elaborated by Ambacher *et al.* [148]. It was found in these publications that both the spontaneous and piezoelectric polarizations of the alloys are highly nonlinear with respect to the alloy composition (Fig. 6.4). The nonlinear behavior of the spontaneous polarization was explained by the different response of the bulk binary constituents of the alloys to the 'hydrostatic pressure' (volume deformation of the bulk binaries from their equilibrium lattice constant) and to the internal strain (varying cation-anion bond length) produced by the alloying. The nonlinear behavior of the piezoelectric polarization was attributed to the nonlinear macroscopic strain response of the bulk binary piezoelectric coefficients (i.e. nonlinear piezoelectricity).

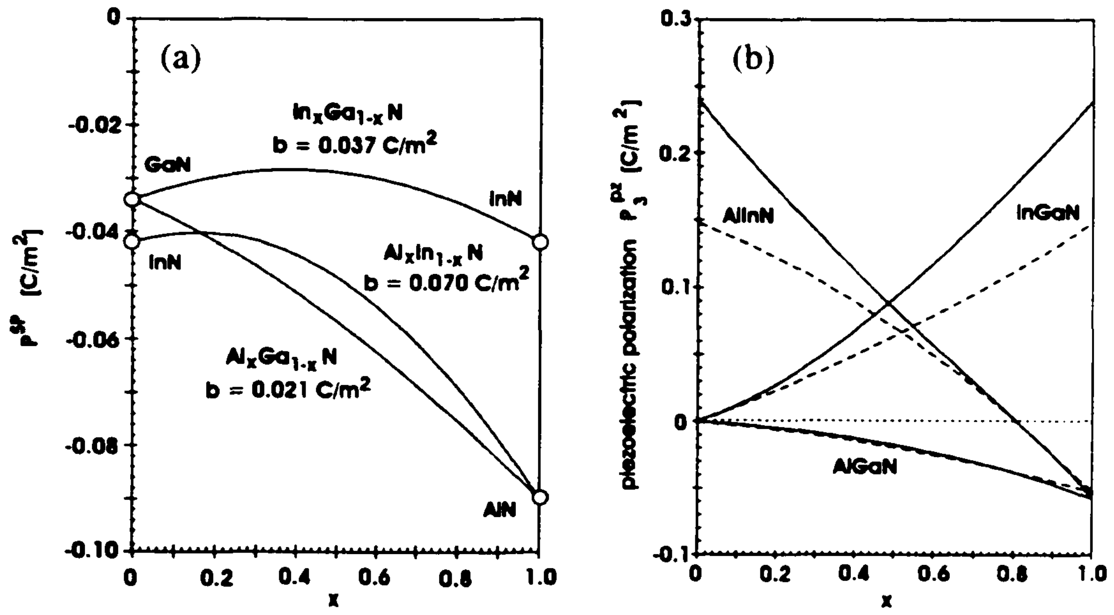

Fig. 6.4. Nonlinear spontaneous (a) and piezoelectric (b) polarization in the group III-nitride alloys as a function of the alloy composition x. Piezoelectric polarization calculated with the linear model is shown with the dashed line. After Ambacher *et al.* [148].

Following the results reported by Bernardini and Fiorentini [147] we calculated the polarization difference $P_w - P_b$ and built-in electric field in our GaN/AlGaN structures. We considered here only the changes in piezoelectric polarization with applied pressure that arise due to the hydrostatic compression of the 'ideal' (i.e. with fixed values of u and c/a) crystal (Fig 6.5), and due to the increase of the internal parameter u. The variation of u with pressure was obtained from the calculated values reported by Wagner and Bechstedt [149]. The spontaneous polarization bowing was included at $p = 1$ atm. The results of these calculations are shown in the Fig. 6.6 by the dashed lines together with the experimental points and the results of the linear model. The slope of the calculated pressure dependence of $P_w - P_b$ is significantly larger than that predicted by

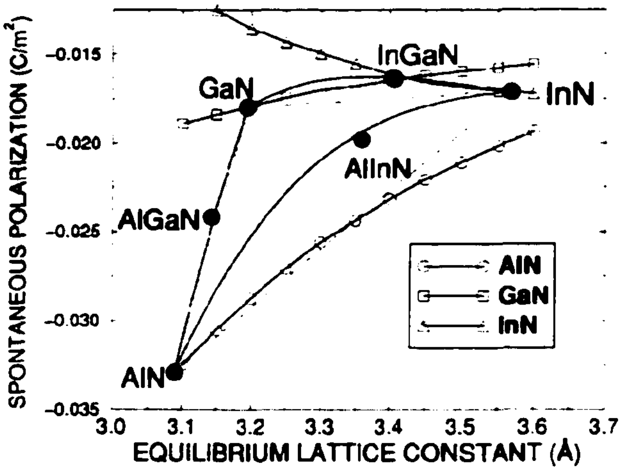

Fig. 6.5. Calculated spontaneous polarization versus lattice constant of ideal wurtzite structure (i. e. structure with fixed at the maximal sphere packing values of $u = 0.375$ and $c/a = \sqrt{8/3}$). Solid circles – values for binary compounds and random alloys; open symbols – values of polarization of binaries as a function of lattice constant a. After Bernardini and Fiorentini [147].

the linear model of polarization and fairly close to the experimentally obtained data. This again confirms our conclusion of the major role of the nonlinear piezoelectricity in the unique pressure behavior of PL in GaN/AlGaN quantum wells.

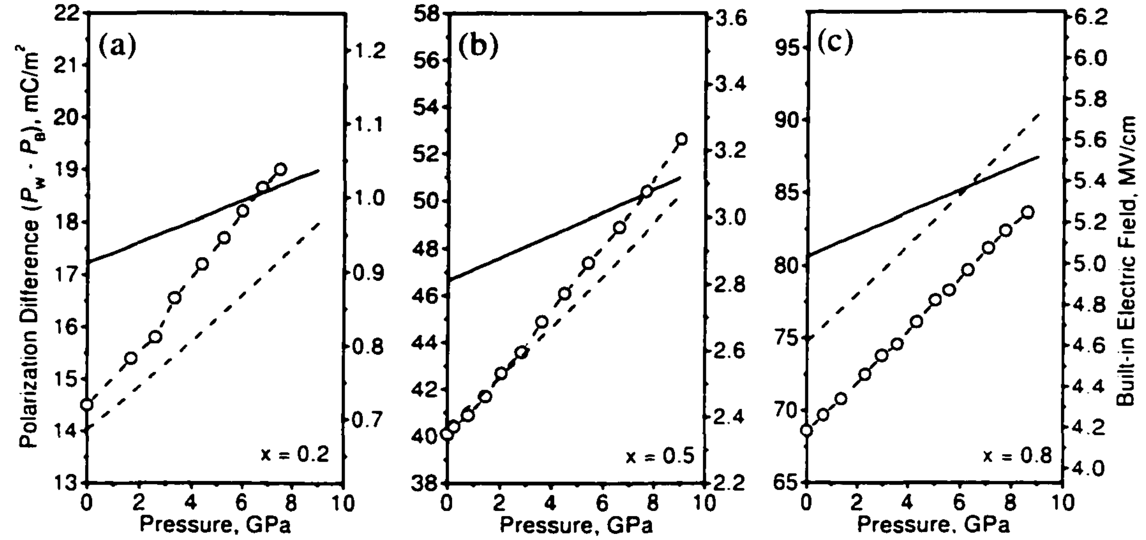

Fig. 6.6. Experimental (circles) and calculated pressure dependence of P_w–P_b and corresponding built-in electric field in 2.9 nm GaN/AlGaN quantum wells. The solid lines show the P_w–P_b and F_w calculated with the linear model; the dashed lines are the results of calculations based on the work of Bernardini and Fiorentini [147].

The model developed by Bernardini and Fiorentini was tested on a set of the experimental data obtained in GaN/AlGaN heterostructures in the work of Fiorentini *et al.* [150]. Figure 6.7 shows the results obtained in this work. The built-in electric field calculated assuming nonlinear spontaneous and piezoelectric polarization was found to better describe the experimental data obtained under variety of conditions in different groups of scientists. This was interpreted as a demonstration of the experimental evidence of the nonlinear behavior of polarization in these heterostructures.

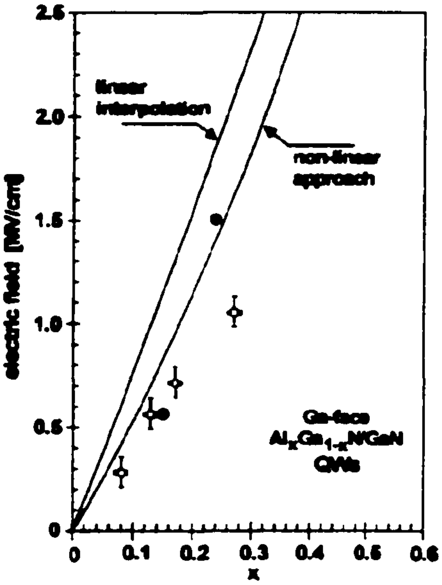

Fig. 6.7. Calculated and experimental values of the built-in electric field in the GaN/AlGaN quantum wells as a function of alloy composition in the barriers. Experimental points are taken from the Ref. 47 (open circles) and Refs.112 and 151 (solid circles).

7. Conclusion

This dissertation provides the first experimental investigation of the nonlinear piezoelectric effect in the group III-nitride heterostructures. This effect is revealed by modifying the strain state in the InGaN/GaN and GaN/AlGaN quantum well structures by applied hydrostatic pressure. To identify nonlinear piezoelectricity as the major mechanism responsible for the observed behavior of photoluminescence with pressure we combine static pressure dependent PL measurements with the time-resolved PL, and utilize the well width dependence of PL peak energy obtained at different pressures in our analysis. The analysis of the experimental results suggests that the polarization-induced electric field in the InGaN/GaN quantum wells increases almost by a factor of two, from ~ 1.4 MV/cm to ~ 2.6 MV/cm, in the 9 GPa pressure range. The field in the GaN/AlGaN quantum wells also shows a significant, 25 – 50 %, increase with pressure, depending on the AlN mole fraction in the barriers. The increase of the piezoelectric field with pressure clearly contradicts the linear model of macroscopic polarization, that predicts a reduction of the electric field in the InGaN/GaN structures and an increase of the field in the GaN/AlGaN quantum wells that is significantly smaller than that observed in the experiment. On the other hand, the increase is reasonably well described when the nonlinear piezoelectric effect is accounted for. We also show that the other secondary effects, such as nonlinear elasticity and photoelastic effects, have significantly smaller contribution to the observed pressure response of PL in the nitride heterostructures.

The immediate implication of the findings of this dissertation is in the modeling of the nitride-based devices, which typically have significant lattice mismatch strain. Our work shows that for the design of such devices the conventional model of polarization does not provide accurate values of the built-in electric field and other polarization-related parameters. Instead, a model including nonlinear polarization effects, such as that recently developed in Refs. 176 and 177, should be applied for these materials.

Aside from this technological implication the work presented here makes an important contribution to solving the puzzle of the anomalous pressure behavior of the PL in InGaN/GaN quantum wells, that was the focus of investigation of several groups and that resulted in large number of publications over the last 5 – 6 years. Although some of the effects considered in the previous investigations contribute to the unique pressure response in this system, our work is the first one to clearly show that the major effect shaping this response is the nonlinear piezoelectricity. Nevertheless, we should acknowledge here the large amount of work that was accomplished in the early studies, which unraveled the unusual behavior of the InGaN/GaN quantum wells and ultimately provoked our investigation.

Even though this dissertation is the result of a significant effort, it does not provide a complete description of the nonlinear piezoelectric effect. More detailed understanding of this phenomenon will require further investigation, both theoretical and experimental, of the unique electromechanical properties of group III-nitrides. Accurate experimental determination of the nonlinear piezoelectric coefficients, as well as the other nonlinear properties of these materials, would require bulk structures with better structural quality than what is currently available. In such structures the nonlinear coefficients can be measured using electromechanical resonance oscillations or acoustic wave propagation techniques [68]. Meanwhile, some of the nonlinear parameters, such as electrostrictive and electroelastic coefficients, can be evaluated with the samples that are readily available by measuring the sample displacement in the externally applied electric field and by measuring strain in the uniaxially stressed samples with the applied field. One of the goals of the work presented in this dissertation and in the ensuing publications was to show the importance of the secondary effects in the group III-nitrides and to initiate extensive investigation of these effects. Due to the large scale of the nonlinearities in nitrides the secondary effects are important not only for the accurate modeling of devices, but also for the potential development of new applications utilizing these effects.

Appendix 1

Definition of electric polarization

Electric polarization of a material as a physical effect can be defined as an unbalanced spatial arrangement of the electrical charges of opposite sign. If the material is modeled as a set of neutral units, polarization is said to create electrical dipoles with electrons and nuclei being displaced with respect to each other. Polarization as a quantity is commonly defined as a dipole moment per unit volume [152]:

$$P = \frac{1}{\Omega} \int \boldsymbol{r}\, \rho(\boldsymbol{r})\, \mathrm{d}^3 r, \qquad \text{(A1.1)}$$

where Ω is the unit volume and $\rho(\boldsymbol{r})$ is the spatial charge distribution. This classical definition uniquely describes polarization in a finite system. However, it is incorrect when applied to an extended matter since the dipole moment depends on the choice of the unit volume [153]. Within the quantum mechanical framework the electrons do not belong to a particular atom or unit cell of a crystal. The charge density of the electrons in a periodic crystal is a continuous and often delocalized function of position, and there is no unique way to define the dipole moment of the cell. Also, polarization in the internal region of any realistic sample strongly depends on the density and distribution of the surface charges, which depend on the sample configuration and the surface conditions [153]. Due to these uncertainties the question whether the macroscopic polarization of extended material as opposed to a finite sample can be meaningfully defined was subject for long lasting debates [154 - 158].

The solution of this problem came in 1992-93 when the foundations of the modern quantum mechanical theory of polarization were laid down by Resta [6, 7] and by Vanderbilt and King-Smith [8, 9]. Martin [159] and Resta [7] showed that the change in the surface charges of extended material experiencing adiabatic transformation resulting in a change of Hamiltonian (*e.g.* when atoms are displaced) can be related to integrals over currents flowing through the interior of the material. Although the total surface charge depends on the surface preparation and some other conditions, the change in this parameter can be uniquely defined from the changes in the bulk. The next key point developed by Vanderbilt and King-Smith [8] was the relation between the change of polarization and the internal current that was expressed in terms of the electron wavefunctions in the interior of the material, with no need to explicitly consider surface effects. The electronic contribution to the polarization difference between two states of a system characterized by an adiabatic transformation parameter λ was related to the electron wavefunctions as [10]:

$$\Delta P_e = P_e(\lambda_2) - P_e(\lambda_1) = -\frac{2e}{(2\pi)^3}\int_{\lambda_1}^{\lambda_2} d\lambda \int_{BZ} \frac{\partial^2}{\partial\lambda\partial k'}\phi^{(\lambda)}(k,k')\Big|_{k'=k} dk\,, \tag{A1.2}$$

where the integration domain in momentum space is the reciprocal unit cell, and $\phi^{(\lambda)}$ is the geometric quantum phase (Berry's phase [160]) of the occupied crystal Bloch states $u_n^{(\lambda)}(k)$ [10]:

$$\phi^{(\lambda)}(k,k') = \mathrm{Im}\{\ln[\det\langle u_m^{(\lambda)}(k)|u_n^{(\lambda)}(k')\rangle]\}\,. \tag{A1.3}$$

The absolute value of electronic polarization can be defined as the polarization difference between a certain state of the system λ and the state λ_0 with zero polarization [57]. Accordingly, the electronic contribution to the total polarization is defined as:

$$P_e(\lambda) = -\frac{2e}{(2\pi)^3}\int_{BZ} \frac{\partial}{\partial k'}\phi^{(\lambda)}(k,k')\Big|_{k'=k} dk\,. \qquad \text{(A1.4)}$$

The total (spontaneous) polarization is then given by the sum of the classical ionic contribution and electronic contribution described by Eq. 2.12 [161]:

$$P = \frac{e}{\Omega}\sum_j Z_j r_j + \sum_{n_{occ}} P_e \qquad \text{(A1.5)}$$

where Z_j and r_j are the atomic number and cell position of the j-th nucleus in the unit cell and n_{occ} is the number of occupied electronic states.

Appendix 2

Calculation of the electron and hole confinement energies in the presence of transverse electric field

The confinement energies are calculated using the approach described by Miller *et al.* [129]. This approach is based on the substitution of the finite barrier well where the confinement energy is sought for with the infinite barrier well of a width that provides the same zero field ground state energy as the finite barrier well.

The first step in this calculation is defining the zero field confinement energies E_1^0 in the conduction and valence bands as a solution of the equation [131]:

$$\frac{m_b}{m_w}\frac{\sqrt{2m_w E_1^0}}{\hbar}\tan\left(\frac{L_w\sqrt{2m_w E_1^0}}{2\hbar}\right)=\frac{\sqrt{2m_b(V_0-E_1^0)}}{\hbar}, \qquad \text{(A2.1)}$$

where m_w and m_b are the effective masses in the well and in the barrier, and V_0 is the barrier height. Once the E_1^0 are found, we calculate the effective well width (separately for the electrons and holes) as:

$$L_{eff}=\frac{\hbar\pi}{\sqrt{2m_w E_1^0}}. \qquad \text{(A2.2)}$$

Then the effective electric field F_{eff} is found as:

$$F_{eff}=\frac{E_1^0}{qL_{eff}}. \qquad \text{(A2.3)}$$

Finally, the eigen energy is found as a solution of the following equation:

$$0 = Ai(Z_+)Bi(Z_-) - Ai(Z_-)Bi(Z_+), \tag{A2.4}$$

where Ai(Z) and Bi(Z) are the Airy function and the Airy function of the second kind respectively, and $Z_\pm$ are given by:

$$Z_\pm = \left[-\frac{\pi F_{eff}}{F}\right]^{2/3}\left(\frac{E_1}{E_1^0} \pm \frac{F_w}{F_{eff}}\right), \tag{A2.5}$$

where F_w is the built-in electric field in the well and E_1 is the resulting energy of the confined state.

After determining the confinement energies the wavefunctions of the quantum well electron and hole can be found as:

$$\psi(Z) = A\left[Bi(Z) - Ai(Z)\frac{Bi(Z_-)}{Ai(Z_+)}\right], \tag{A2.6}$$

where A is a normalization parameter (constant) found from the condition $\int_{-\infty}^{\infty}\psi^2(z)dz = 1$, and Z is the function of the distance z in the direction perpendicular to the well:

$$Z = -\left[\frac{2m_w}{(q\hbar F)^2}\right]^{1/3}(E_1 + qFz). \tag{A2.7}$$

Appendix 3

Calculation of quantum well exciton binding energy

The exciton binding energy is calculated using approach described by Leavitt and Little [133]. For the e_1 and hh_1 subbands the exciton binding energy E_{ex} is found as:

$$E_{ex} = \int_{-\infty}^{\infty}\int_{-\infty}^{\infty} |\psi_e(z_e)|^2 |\psi_h(z_h)|^2 E_0 w[(z_e - z_h)/a_0] dz_e dz_h, \tag{A3.1}$$

where $E_0 = \mu_r q^4 / 2\epsilon^2 \hbar^2$, $a_0 = \epsilon \hbar^2 / \mu_r q^2$, μ_r is the density of states reduced mass, and the normalized binding energy $w[(z_e - z_h)/a_0]$ of a system in which the electron and hole are confined to the $z = z_e$ and $z = z_h$ planes respectively is given by the following approximation of the exact solution:

$$w(v) = \frac{4 + 12.97v + 0.718v^2}{1 + 9.65v + 9.24v^2 + 0.3706v^3}. \tag{A3.2}$$

The reduced mass μ_r is found as:

$$\mu_r^{-1} = \int_{-\infty}^{\infty} \frac{|\psi_e(z_e)|^2}{m_e(z_e)} dz_e + \int_{-\infty}^{\infty} \frac{|\psi_h(z_h)|^2}{m_h(z_h)} dz_h, \tag{A3.3}$$

where $m_e(z_e)$ and $m_h(z_h)$ are the position-dependent electron and heavy hole effective masses. The electron and hole wavefunctions $\psi_e(z_e)$ and $\psi_h(z_h)$ are calculated in the fashion described in Appendix 2.

Bibliography

[1] E. Tiede, M. Thimann, and K. Sensse, *Chemische Berichte* **61**, 1568 (1928).

[2] W. C. Johnson, J. B. Parsons, and M. C. Crew, *J. Phys. Chem.* **36**, 2561 (1932).

[3] R. Juza and H. Hahn, *Zeitschrift für anorganische und allgemeine Chemie* **239**, 282 (1938).

[4] I. Akasaki, H. Amano, M. Kito, and K. Hiramatsu, *J. Lumin.* **48/49**, 666 (1991).

[5] S. Nakamura, M. Senoh, and T. Mukai, *Jpn. J. Appl. Phys.* **30**, L1708 (1991).

[6] R. Resta, *Ferroelectrics* **136**, 51 (1992).

[7] R. Resta, *Europhys. Lett.* **22**,133 (1993).

[8] R.D. King-Smith and D. Vanderbilt, *Phys. Rev.* B **48**, 1651 (1993).

[9] D. Vanderbilt and R.D. King-Smith, *Phys. Rev.* B **48**, 4442 (1993).

[10] F. Bernardini, V. Fiorentini, and D. Vanderbilt, *Phys. Rev. Lett.* **79**, 3958 (1997).

[11] V. Fiorentini, F. Bernardini, F. Della Sala, A. Di Carlo, and P. Lugli, *Phys. Rev.* B **60**, 8849 (1999).

[12] C. Gmachl, H.M. Ng, S.N.G. Chu, and A.Y. Cho, Appl. Phys. Lett. **77**, 3722 (2000).

[13] O. Ambacher, J. Smart, J.R. Shealy, N.G. Weimann, K. Chu, M. Murphy, W.J. Schaff, L.F. Eastman, R. Dimitrov, L. Wittmer, M. Stutzmann, W. Rieger, and J. Hilsenbeck, *J. Appl. Phys.* **85**, 3222 (1999).

[14] W. G. Cady, *Piezoelectricity* (New York: Dover, 1964).

[15] J. F. Nye, *Physical properties of crystals* (Claredon, Oxford, 1969).

[16] D. L. Smith, *Solid State Comm.* **57**, 919 (1986).

[17] D. L. Smith and C. Mailhiot, *J. Appl. Phys.* **63**, 2717 (1988).

[18] C. Mailhiot and D. L. Smith, *Phys. Rev.* B **38**, 5520 (1988).

[19] E. A. Caridi, T. Y. Chang, K. W. Goossen, and L. F. Eastman, *Appl. Phys. Lett.* **56**, 659 (1990).

[20] M. P. Halsall, J. E. Nicholls, J. J. Davies, B. Cockayne, and P. J. Wright, *J. Appl. Phys.* **71**, 907 (1992).

[21] R. L. Tober and T. B. Bahder, *Appl. Phys. Lett.* **63**, 2369 (1993).

[22] R. André, C. Deshayes, J. Cibert, Le Si Dang, S. Tatarenko, and K. Saminadayar, *Phys. Rev.* B **42**, 11392 (1990).

[23] J. Cibert, R. André, C. Deshayes, L. S. Dang, H. Okumura, S. Tatarenko, G. Feuillet, P. H. Jouneau, R. Mallard, and K. Saminadayar, *J. Cryst. Growth* **117**, 424 (1992).

[24] A. Dal Corso, R. Resta, and S. Baroni, *Phys. Rev.* B **47**, 16252 (1993).

[25] K. Shimada, T. Sota, K. Suzuki, and H. Okumura, *Jpn. J. Appl. Phys.* **37**, L1421 (1998).

[26] C. Stampfl and C.G. Van de Walle, *Phys. Rev.* B **59**, 5521 (1999).

[27] M. Leszczynski, T. Suski, J. Domagala, and P. Prystawko, in: *Properties, processing and applications of gallium nitride and related semiconductors*, edited by J.H. Edgar, S. Strite, I. Akasaki, H. Amano, and C. Wetzel, (INSPEC, London, 1999), p. 6.

[28] H. Schulz and K. H. Thiemann, *Solid State Commun.* **23**, 815 (1977).

[29] L. Bellaiche, K. Kunc, and J. M. Besson, *Phys. Rev.* B **54**, 8945 (1996).

[30] I. Vurgaftman, J. R. Meyer, and L. R. Ram-Mohan, *J. Appl. Phys.* **89**, 5815 (2001).

[31] M. Suzuki, T. Uenoyama, and A. Yanase, *Phys. Rev.* B **52**, 8132 (1995).

[32] Y. C. Yeo, T. C. Chong, and M. F. Li, *J. Appl. Phys.* **83**, 1429 (1998).

[33] T. Onuma, S. F. Chichibu, T. Sota, K. Asai, S. Sumiya, T. Shibata, and M. Tanaka, *Appl. Phys. Lett.* **81**, 652 (2002).

[34] W.W. Chow and S.W. Koch, *Semiconductor-Laser Fundamentals* (Springer, Berlin, 1999), p.189.

[35] A. Polian, M. Grimsditch, and I. Grzegory, J. Appl. Phys. **79**, 3343 (1996).

[36] K. Tsubouchi, K. Sugai, and N. Mikoshiba, in *1981 Ultrasonics Symposium*, edited by B. R. McAvoy (IEEE, New York, 1981), vol. 1, p. 375.

[37] A.F. Wright, J. Appl. Phys. **82**, 2833 (1997).

[38] D. Huang, P. Visconti, M. A. Reshchikov, F. Yun, T. King, A. A. Baski, C. W. Litton, J. Jasinski, Z. Liliental-Weber, and H. Morkoç, *phys. stat. sol.* (a) **188**, 571 (2001).

[39] D. Huang, P. Visconti, K. M. Jones, M. A. Reshchikov, F. Yun, A. A. Baski, T. King, and H. Morkoç, *Appl. Phys. Lett.* **78**, 4145 (2001).

[40] O. Ambacher, *J. Phys. D: Appl. Phys.* **31**, 2653 (1998).

[41] E. S. Hellman, *MRS Internet J. Nitride Semicond. Res.* **3**, 11 (1998).

[42] J. Wu, W. Walukiewicz, K. M. Yu, J. W. Ager III, E. E. Haller, H. Lu, W. J. Schaff, Y. Saito, and Y. Nanishi, *Appl. Phys. Lett.* **80**, 3967 (2002).

[43] S. B. Nam, D. C. Reynolds, C. W. Litton, R. J. Almassy, T. C. Collins, and C. M. Wolfe, *Phys. Rev.* B **13**, 761 (1976).

[44] M. Smith, G. D. Chen, J. Y. Lin, H. X. Jiang, M. Asif Khan, C. J. Sun, Q. Chen, and J. W. Yang, *J. Appl. Phys.* **79**, 7001 (1996).

[45] S. Chichibu, H. Okumura, S. Nakamura, G. Feuillet, T. Azuhata, T. Sota, and S. Yoshida, *Jpn. J. Appl. Phys.* **36**, 1976 (1997).

[46] P. Bigenwald, P. Lefebvre, T. Bretagnon, and B. Gil, *phys. stat. sol.* (b) **216**, 371 (1999).

[47] N. Grandjean, B. Damilano, S. Dalmasso, M. Leroux, M. Laügt, and J. Massies, *J. Appl. Phys.* **86**, 3714 (1999).

[48] L. D. Landau and E. M. Lifshitz, *Theory of elasticity* (Pergamon, London, 1959).

[49] Y. Takeda and M. Tabuchi, in: *Properties, processing and applications of gallium nitride and related semiconductors*, edited by J.H. Edgar, S. Strite, I. Akasaki, H. Amano, and C. Wetzel, (INSPEC, London, 1999), p. 381.

[50] K. Dovidenko, S. Oktyabrsky, J. Narayan, and M. Razeghi, *J. Appl. Phys.* **79**, 2439 (1996).

[51] L. Liu and J. H. Edgar, *Mater. Sci. Eng.* R **37**, 61 (2002).

[52] O.-H. Nam, M. D. Bremser, T. S. Zheleva and R. F. Davis, *Appl. Phys. Lett.* **71**, 2638 (1997).

[53] Z. Liliental-Weber and D. Cherns, *J. Appl. Phys.* **89**, 7833 (2001).

[54] C. Wetzel, T. Takeuchi, S. Yamaguchi, H. Katoh, H. Amano, and I. Akasaki, *Appl. Phys. Lett.* **73**, 1994 (1998).

[55] Y. Koide, H. Itoh, M. R. H. Khan, K. Hiramatu, N. Sawaki, and I. Akasaki, *J. Appl. Phys.* **61**, 4540 (1987).

[56] S.H. Wei and A. Zunger, *Appl. Phys. Lett.* **69**, 2719 (1996).

[57] F. Bernardini, V. Fiorentini, and D. Vanderbilt, *Phys. Rev.* B **56**, R10024 (1997).

[58] F. Bernardini, V. Fiorentini, and D. Vanderbilt, *Phys. Rev.* B **63**, 193201 (2001).

[59] I. L. Guy, S. Muensit, and E. M. Goldys, *Appl. Phys. Lett.* **75**, 4133 (1999).

[60] F. Bernardini and V. Fiorentini, *phys. stat. sol.* (b) **216**, 391 (1999).

[61] G. Bastard, E.E. Mendez, L.L. Chang, and L. Esaki, *Phys. Rev.* B **28**, 3241 (1983).

[62] F. D. Sala, A. Di Carlo, P. Lugli, F. Bernardini, V. Fiorentini, R. Scholz, and J. M. Janku, *Appl. Phys. Lett.* **74**, 2002 (1999).

[63] A.D. Bykhovski, B.L. Gelmont, and M.S. Shur, *J. Appl. Phys.* **81**, 6332 (1997).

[64] T. Takeuchi, H. Amano, and I. Akasaki, *Jpn. J. Appl. Phys.* **39**, 413 (2000).

[65] M. R. McCartney, F. A. Ponce, J. Cai, and D. P. Bour, *Appl. Phys. Lett.* **76**, 3055 (2000).

[66] I. L. Guy, S. Muensit, and E. M. Goldys, *Appl. Phys. Lett.* **75**, 3641 (1999).

[67] W. P. Mason, *Piezoelectric crystals and their application to ultrasonics* (D. Van Nostrand, New York, 1950) p. 463.

[68] S. I. Chizhikov, N. G. Sorokin, and V. S. Petrakov, *Ferroelectrics* **41**, 9 (1982).

[69] N. W. A. van Uden, J. R. Downes, and D. J. Dunstan, *Phys. Rev.* B **63**, 233304 (2001).

[70] R. N. Thurston and K. Brugger, *Phys. Rev.* **133**, A1604 (1964).

[71] K. Brugger, *Phys. Rev.* **133**, A1611 (1964).

[72] R. Stern and R. T. Smith, *J. Acoust. Soc. Am.* **44**, 640 (1968).

[73] H. J. McSkimin and P. Andreatch, Jr., *J. Appl. Phys.* **38**, 2610 (1967).

[74] E. H. Bogardus, *J. Appl. Phys.* **36**, 2504 (1965).

[75] F. D. Murnaghan, *Proc. Natl. Acad. Sci. USA* **30**, 244 (1944).

[76] M. Ueno, M. Yoshida, A. Onodera, O. Shimomura, and K. Takemura, *Phys. Rev.* B **49**, 14 (1994).

[77] T. Tsuchiya, K. Kawamura, O. Ohtaka, H. Fukui and T. Kikegawa, *Solid State Commun.* **121**, 555 (2002).

[78] R. Kato and J. Hama, *J. Phys.: Condens. Matter* **6**, 7617 (1994).

[79] K. Hruška, *Chech. J. Phys.* B **14**, 309 (1964).

[80] G. A. Reider, E. Kittinger, and J. Tichý, *J. Appl. Phys.* **53**, 8716 (1982).

[81] C. K. Hruška, *IEEE Transactions on Sonics and Ultrasonics* **SU-25**, 198 (1978).

[82] R. André, J. Cibert, Le Si Dang, J. Zeman, and M. Zigone, *Phys. Rev.* B **53**, 6951 (1996).

[83] H. Beige and G. Schmidt, *Ferroelectrics* **41**, 39 (1982).

[84] R. André, C. Bodin, J. Cibert, Le Si Dang, and G. Feuillet, *J. De Physique IV* **3**, 429 (1993).

[85] R. E. Newman, V. Sundar, R. Yimnirun, J. Su, and Q. M. Zhang, *J. Phys. Chem.* B **101**, 10141 (1997).

[86] N. E. Christensen and I. Gorczyca, *Phys. Rev.* B **50**, 4397 (1994).

[87] B. Abbar, B. Bouhafs, H. Aourag, G. Nouet, and P. Ruterana, *phys. stat. sol.* (b) **228**, 457 (2001).

[88] P. Perlin, I. Gorczyca, N. E. Christensen, I. Grzegory, H. Teisseyre, and T. Suski, *Phys. Rev.* B **45**, 13307 (1992).

[89] J. Miragliotta, D. K. Wickenden, T. J. Kistenmacher, and W. A. Bryden, *J. Opt. Soc. Am.* B **10**, 1447 (1993).

[90] Y. Fujii, S. Yoshida, S. Misawa, S. Maekawa, and S. Sakudo, *Appl. Phys. Lett.* **31**, 815 (1977).

[91] J. Chen, Z. H. Levine, and J. W. Wilkins, *Appl. Phys. Lett.* **66**, 1129 (1995).

[92] S. D. Lester, F. A. Ponce, M. G. Craford, and D. A. Steigerwald, *Appl. Phys. Lett.* **66**, 1249 (1995).

[93] S. J. Rosner, E. C. Carr, M. J. Ludowise, G. Girolami, and H. I. Erikson, *Appl. Phys. Lett.* **70**, 420 (1997).

[94] T. Sugahara, H. Sato, M. Hao, Y. Naoi, S. Kurai, S. Tottori, K. Yamashita, K. Nishino, L. T. Romano and S. Sakai, *Jap. J. Appl. Phys.* **37**, L398 (1998).

[95] S. Chichibu, T. Azuhata, T. Sota, and S. Nakamura, *Appl. Phys. Lett.* **69**, 4188 (1996).

[96] E. S. Jeon, V. Kozlov, Y.-K. Song, A. Vertikov, M. Kuball, A. V. Nurmikko, H. Liu, C. Chen, R. S. Kern, C. P. Kuo, and M. G. Craford, *Appl. Phys. Lett.* **69**, 4194 (1996).

[97] Y. Narukawa, Y. Kawakami, S. Fujita, S. Fujita, and S.Nakamura, *Phys. Rev.* B **55**, R1938 (1997).

[98] M. Sugawara, *Phys. Rev.* B 51, 10743 (1995).

[99] I-hsiu Ho and G. B. Stringfellow, *Appl. Phys. Lett.* **69**, 2701 (1996).

[100] D. M. Wood and A. Zunger, *Phys. Rev. Lett.* **61**, 1501 (1988).

[101] S. B. Zhang and A. Zunger, *Appl. Phys. Lett.* **71**, 677 (1997).

[102] L. Bellaiche, T. Mattila, L.-W. Wang, S.-H. Wei, and A. Zunger, *Appl. Phys. Lett.* **74**, 1842 (1999).

[103] Y. Narukawa, Y. Kawakami, M. Funato, S. Fujita, S. Fujita, and S.Nakamura. *Appl. Phys. Lett.* **70**, 981 (1997).

[104] P. R. C. Kent and A. Zunger, *Appl. Phys. Lett.* **79**, 1977 (2001).

[105] P. Lefebvre, J. Allègre, B. Gil, A. Kavokine, H. Mathieu, W. Kim, A. Salvador. A. Botchkarev, and H. Morkoç, *Phys. Rev.* B **57**, R9447 (1998).

[106] K. C. Zeng, M. Smith, J. Y. Lin, and H. X. Jiang, *Appl. Phys. Lett.* **73**, 1724 (1998).

[107] P. Lefebvre, J. Allègre, and H. Mathieu, *Mat. Sci. Eng.* B **59**, 307 (1999).

[108] H. M. Ng, R. Harel, S. N. G. Chu, A.Y. Cho, *J. Electr. Mat.* **30**, 134 (2001).

[109] A. Bykhovski, B. Gelmont, M. Shur, and A. Khan, *J. Appl. Phys.* **77**, 1616 (1995).

[110] T. Takeuchi, S. Sota, M. Katsuragawa, M. Komori, H. Takeuchi, H. Amano, and I. Akasaki, *Jap. J. Appl. Phys.* **36**, L382 (1997).

[111] This experimental finding can be explained by the self-screening effect [11].

[112] R. Langer, J. Simon, V. Ortiz, N. T. Pelekanos, A. Barski, R. André, and M. Godlewski, *Appl. Phys. Lett.* **74**, 3827 (1999).

[113] C. Wetzel, T. Takeuchi, H. Amano, and I. Akasaki, *J. Appl. Phys.* **85**, 3786 (1999).

[114] C. Wetzel, H. Amano, and I. Akasaki, *Jap. J. Appl. Phys.* **39**, 2425 (2000).

[115] J. S. Im, H. Kollmer, J. Off, A. Sohmer, F. Scholz, and A. Hangleiter, *Phys. Rev.* B **57**, R9435 (1998).

[116] D. Cherns, J. Barnard, and F. A. Ponce, *Solid State Commun.* **111**, 281 (1999).

[117] P. Perlin, V. Iota, B. A. Weinstein, P. Wisniewski, T. Suski, P. G. Eliseev, and M. Osinski, *Appl. Phys. Lett.* **70**, 2993 (1997).

[118] W. Shan, J. W. Ager III, W. Walukiewicz, E. E. Haller, M. D. McCluskey, N. M. Johnson, and D. P. Bour, *Phys. Rev.* B **58**, R10191 (1998).

[119] B.A. Weinstein, P. Perlin, N.E. Christensen, I. Gorczyca, V. Iota, T. Suski, P. Wisniewski, M. Osinski, and P.G. Eliseev, *Solid. St. Comm.* **106**, 567 (1998).

[120] P. Perlin, C. Kisielowski, V. Iota, B. A. Weinstein, L. Mattos, N. A. Shapiro, J. Kruger, E. R. Weber, and J. Yang, *Appl. Phys. Lett.* **73**, 2778 (1998).

[121] T. Suski, P. Perlin, C. Skierbiszewski, P. Wisniewski, L. Dmowski, M. Leszczynski, and W. Walukiewicz, *phys. stat. sol. (b)* **216**, 521 (1999)

[122] R.–D. Hong, D. W. Jenkins, S. Y. Ren, and J. D. Dow, *Phys. Rev.* B **38**, 12549 (1988).

[123] M. Yousuf, *Diamond anvil cells in High-pressure studies of semiconductors*, in *Semiconductors and semimetals*, vol. 55 edited by T. Suski and W. Paul (San Diego: Academic Press, 1998).

[124] A. R. Goñy and K. Syassen, *Optical properties of semiconductors under pressure*, in *Semiconductors and semimetals*, vol. 54 edited by T. Suski and W. Paul (San Diego: Academic Press, 1998).

[125] P. Perlin, I. Gorczyca, T. Suski, P. Wisniewski, S. Łepkowski, N. E. Christensen, A. Svane, M. Hansen, S. P. DenBaars, B. Damilano, N. Grandjean, and J. Massies, *Phys. Rev.* B **64**, 115319 (2001).

[126] P. Perlin, L. Mattos, N.A. Shapiro, J. Kruger, W.S. Wong, T. Sands, N.W. Cheung, and E.R. Weber, *J. Appl. Phys.* **85**, 2385 (1999).

[127] L.T. Romano, C.G. Van de Walle, J.W. Ager III, W. Götz, and R.S. Kern, *J. Appl. Phys.* **87**, 7745 (2000).

[128] M. Leroux, N. Grandjean, J. Massies, B. Gil, P. Lefebvre, and P. Bigenwald, *Phys. Rev.* B **60**, 1496 (1999).

[129] D.A.B. Miller, D.S. Chemla, T.C. Damen, A.C. Gossard, W. Wiegmann, T.H. Wood, and C.A. Burrus, *Phys. Rev.* B **32**, 1043 (1985).

[130] A. Dmitriev and A. Oruzheinikov, *J. Appl. Phys.* **86**, 3241 (1999).

[131] S.L. Chuang, *Physics of optoelectronic devices* (New York: Wiley, 1995).

[132] H. Mariette, D.J. Wolford, and J.A. Bradley, *Phys. Rev.* B **33**, 8373 (1986).

[133] R.P. Leavitt and J.W. Little, *Phys. Rev.* B **42**, 11774 (1990).

[134] J. Simon, R. Langer, A. Barski, M. Zervos, and N.T. Pelekanos, *phys. stat. sol. (a)* **188,** 867 (2001).

[135] J. L. Sánches-Rojas, J. A. Garrido, and E. Munoz, *Phys. Rev.* B **61**, 2773 (2000).

[136] D. Brunner, H. Angerer, E. Bustarret, F. Freudenberg, R. Höpler, R. Dimitrov, O. Ambacher, and M. Stutzmann, *J. Appl. Phys.* **82**, 5090 (1997).

[137] J. Singh, *Physics of semiconductors and their heterostructures* (New York: Mc-Graw-Hill, 1993).

[138] J. H. Gieske and G. R. Barsch, *phys. stat. sol.* **29,** 121 (1968).

[139] G. Vaschenko, D. Patel, C.S. Menoni, S. Keller, U.K. Mishra, and S.P. DenBaars, *Appl. Phys. Lett.* **78**, 640 (2001).

[140] D. Patel, G. Vaschenko, C.S. Menoni, S. Keller, U.K. Mishra, S.P. DenBaars, N. F. Gardner, J. Sun, W. Götz, and C. N. Tomé, in *Frontiers of high pressure research II: Application of high pressure to low-dimensional novel electronic materials*, edited by H. D. Hochheimer, B. Kuchta, P. K. Dorhout, and J. L. Yarger (Dordrecht, Ned.: Kluwer, 2001).

[141] G. Vaschenko, D. Patel, C.S. Menoni, N. F. Gardner, J. Sun, W. Götz, C. N. Tomé, and B. Clausen, *phys. stat. sol.* (b) **228**, 73 (2001).

[142] G. Vaschenko, D. Patel, C.S. Menoni, N. F. Gardner, J. Sun, W. Götz, C. N. Tomé, and B. Clausen, *Phys. Rev.* B **64**, 241308 (2001).

[143] G. Vaschenko, D. Patel, C. S. Menoni, H. M. Ng, and A. Y. Cho, *Appl. Phys. Lett.* **80**, 4211 (2002).

[144] S. P. Łepkowski, H. Teisseyre, T. Suski, P. Perlin, N. Grandjean and J. Massies, *Appl. Phys. Lett.*, **79**, 1483 (2001); P. Perlin, S. P. Łepkowski, H. Teisseyre, T. Suski, N. Grandjean, and J. Massies, *Acta Physica Polonica* A **100**, 261 (2001).

[145] P. Perlin, T. Suski, S. P. Łepkowski, H. Teisseyre, N. Grandjean, and J. Massies, *phys. stat. sol.* (a) **188**, 839 (2001).

[146] T. Suski, H. Teisseyre, S. P. Łepkowski, P. Perlin, T. Kitamura, Y. Ishida, H. Okumura, and S. F. Chichibu, *Appl. Phys. Lett.* **81**, 232 (2002).

[147] F. Bernardini and V. Fiorentini, *Phys. Rev.* B **64**, 085207 (2001).

[148] O. Ambacher, J. Majewski, C. Miskys, A. Link, M. Hermann, M. Eickhoff, M. Stutzmann, F. Bernardini, V. Fiorentini, V. Tilak, B. Schaff, and L. F. Eastman, *J. Phys.: Condens. Mat.* **14**, 3399 (2002).

[149] J.-M. Wagner and F. Bechstedt, *Phys. Rev.* B **62**, 4526 (2000).

[150] V. Fiorentini, F. Bernardini, and O. Ambacher, *Appl. Phys. Lett.* **80**, 1204 (2002).

[151] H. S. Kim, J. Y. Lin, H. X. Jiang, W. W. Chow, A. Botchkarev, and H. Morkoç, *Appl. Phys. Lett.* **73**, 3426 (1998).

[152] C. Kittel, *Introduction to solid state physics* (John Wiley & Sons, New York, 1971), p. 449.

[153] R. M. Martin and G. Ortiz, *Solid State Commun.* **102**, 121 (1997).

[154] J. W. F. Woo, *Phys. Rev.* B **4**, 1218 (1971).

[155] R. M. Martin, *Phys. Rev.* B **5**, 1607 (1972).

[156] C. Kallin and B. I. Halperin, *Phys. Rev.* B **29**, 2175 (1984).

[157] A. K. Tagantsev, *Phys. Rev. Lett.* **69**, 389 (1992).

[158] A. Baldereschi, M. Posternak, and R. Resta, *Phys. Rev. Lett.* **69**, 390 (1992).

[159] R. M. Martin, *Phys. Rev.* B **9**, 1998 (1974).

[160] M. V. Berry, *Proc. Roy. Soc. Lond.* A **392**, 45 (1984).

[161] D. Vanderbilt, *J. Phys. Chem. Sol.* **61**, 147 (2000).